

Search for Charginos and Neutralinos
in Models with Gauge-Mediated SUSY breaking
in e^+e^- Collisions at $\sqrt{s}=183$ GeV

重心系エネルギー 183 GeV での電子・陽電子衝突実験における
ゲージ粒子媒介により超対称性を破るモデルに基づいた
チャージーノ、ニュートラリーノの探索

三原 智



①

Search for Charginos and Neutralinos
in Models with Gauge-Mediated SUSY breaking
in e^+e^- Collisions at $\sqrt{s} = 183$ GeV

Satoshi Mihara

International Center for Elementary Particle Physics

University of Tokyo

Abstract

A search for the pair production of charginos, $\tilde{\chi}_1^+ \tilde{\chi}_1^-$, and the associated pair production of neutralinos, $\tilde{\chi}_2^0 \tilde{\chi}_1^0$, has been performed in the context of supersymmetric models with a neutralino as the next-to-lightest supersymmetric particle and a gravitino as the lightest supersymmetric particle at the center-of-mass energy of 183 GeV. The data corresponding to 56.75pb^{-1} collected with the OPAL detector at LEP have been used. No evidence for their existence was found. Cross section limits on their production and the exclusion regions in the M_2 vs. μ plane for non-zero $\tilde{\chi}_1^0$ lifetimes are presented. The exclusion region in the parameter space of the minimal gauge-mediated supersymmetry breaking model is also given.

Acknowledgement

I would like to thank Professor S. Orito, who gave me a chance to join the OPAL Collaboration. I am also grateful to Professor S. Komamiya. His continuous support, advice and encouragement have helped me to keep my interest and motivation. I would like to appreciate my colleagues of ICEPP, International Center of Elementary Particle Physics, the University of Tokyo; their encouragement and inspiring discussions throughout this work were invaluable.

I am indebted to all the members of the OPAL Collaboration, for their construction of the beautiful detector and successful operation during LEP2.

They are also very helpful to a newcomer, and I was helped by many of them in understanding the experiment. Among all, I would like to express my special gratitude to several persons who has directly helped my work: Dr. R.A. McPherson, who executed the low-multiplicity analysis and achieved good performance, without which this work wouldn't have completed. Dr. S. Asai, who helped me strongly in generating Monte Carlo samples for the chargino and neutralino signals and offered me a lot of suggestions during this analysis. Dr. S Yamashita, who has designed and constructed the energy flow algorithm. He offered me excellent ideas through many discussions on the analysis method and interpretation. I would show my gratitude to Dr. C. Rembser, who prepared the framework to simulate the expected signals incorporating their lifetime.

Finally, I would like to thank the SL Division of CERN for the efficient operation of the LEP accelerator, and other CERN staffs for their support.

Satoshi Mihara

Contents

Acknowledgement	1
1 Introduction	4
2 Gauge-Mediated SUSY breaking model and Experimental Signatures	6
2.1 The Minimal Model of Gauge-Mediated SUSY Breaking	6
2.2 The Gravitino	11
2.3 Experimental Signature	13
2.3.1 Neutralino NLSP	13
2.3.2 Slepton NLSP	15
3 Experimental Apparatus	17
3.1 Accelerator	17
3.1.1 Structure	17
3.1.2 Accelerating System	18
3.2 The OPAL detector	19
3.2.1 Magnet	21
3.2.2 Central Tracking System	21
3.2.3 Electromagnetic Calorimeter	24
3.2.4 Hadron Calorimeter	27
3.2.5 Muon Detector	27
3.2.6 Silicon Tungsten Calorimeter	27
3.2.7 Forward Calorimeter	28
3.2.8 Gamma Catcher	29
3.2.9 Trigger	29
4 Monte Carlo Event Simulation	33
4.1 Outline of Monte Carlo Event Simulation	33
4.2 Simulation of Signals	34
4.2.1 $\tilde{\chi}_1^+ \tilde{\chi}_1^-$ Signals	34
4.2.2 $\tilde{\chi}_2^0 \tilde{\chi}_1^0$ Signals	34
4.3 Simulation of Background Events	34

4.3.1 Multihadronic Processes	35
4.3.2 Four-fermion Processes	35
4.3.3 Lepton-pair Processes	35
4.3.4 Two-photon processes	35
5 Analysis	37
5.1 Algorithm to Calculate Energy Flow	38
5.2 Jet Reconstruction Algorithm	42
5.3 Acoplanarity Angle	49
5.4 Identification of Isolated Photons	49
5.5 Luminosity	52
5.6 Quality Requirements	54
5.7 Detection of Charginos	55
5.7.1 Analysis A ($N_{\text{ch}} - N_{\text{conv}} > 4$)	56
5.7.2 Analysis B ($N_{\text{ch}} - N_{\text{conv}} \leq 4$)	60
5.7.3 Combined Efficiencies and Background for $\tilde{\chi}_1^+ \tilde{\chi}_1^-$	62
5.7.4 Detection Efficiencies for Arbitrary Leptonic Branching Fraction of $\tilde{\chi}_1^\pm$ Decay	62
5.7.5 Detection Efficiencies for Arbitrary $\tilde{\chi}_1^0$ Lifetimes	64
5.8 Detection of Neutralino	65
5.9 Systematic Errors and Corrections	65
6 Results	72
6.1 Limits on the Production Cross Sections	72
6.2 Limits in the M_2 vs. μ Plane	73
6.3 Limits in the Minimal GMSB Model Parameter Space	73
7 Conclusion	86
A SUSY particles	92
B Field contents of gauginos	93
B.1 Neutralinos	93
B.2 Charginos	94
C Particle ID	95
C.1 Electron ID	95
C.2 Muon ID	96
D The OPAL Collaboration	97

Chapter 1

Introduction

The Standard Model (SM) in high energy physics provides a successful description of the phenomena which have been experimentally observed. It predicts the existence of the Higgs boson in order to allow the gauge bosons to acquire masses without destroying the gauge invariance. Since the vacuum expectation value of the Higgs field has been experimentally determined to be $\langle H \rangle = 174$ GeV, the Higgs mass should lie near the electroweak scale. However the Higgs mass receives very large quantum corrections from the virtual effects of various particles which couple to the Higgs field. These corrections are of the order to which the theory is valid (its cut-off), and where new physics appears. If the theory is valid up to the scale of the gauge unification (GUT) or Planck scale, extreme fine tuning is necessary at each order of perturbation theory to avoid the blow up of the Higgs mass. This is called the "naturalness" or "hierarchy" problem.

Supersymmetry (SUSY) [1] can provide a solution to this problem. If SUSY is an exact symmetry, the SUSY particles would have the same masses as their SM partners. However since no SUSY particles have been observed experimentally, SUSY must be a broken symmetry. Then it is important to understand the mechanism by which SUSY breaking occurs and is transmitted to the particles of the SM and their superpartners.

One possibility to understand this mechanism is a gravity-mediated approach. In this approach SUSY is broken at a scale of $\sim 10^8$ TeV in a sector (called "hidden sector") which communicates with the particles of the minimal supersymmetric standard model (MSSM) [2] only through gravitational interactions. This has historically been the most popular approach, and its phenomenological consequence has been studied extensively.

Another possibility is that dynamical SUSY breaking occurs at a scale as low as 10 TeV and SUSY breaking is transmitted by "messengers" through the ordinary gauge interactions [3, 4, 5], which is called gauge-mediated SUSY breaking (GMSB). GMSB models are highly predictive with respect to the phenomenology at the electroweak scale. In GMSB models, the masses of squarks, sleptons,

neutralinos, and charginos are determined with only a handful of free parameters. In addition, flavour-changing neutral currents are automatically suppressed because the gauge interaction does not distinguish the flavours. Another striking feature is that the gravitino is naturally the lightest supersymmetric particle (LSP). Assuming R -parity is conserved, the principal decay of the next-to-the-lightest supersymmetric particle (NLSP) is to its partner plus a gravitino. The longitudinal component of the gravitino, "the goldstino", couples to matter with strength proportional to F^{-1} , where \sqrt{F} is the scale of SUSY breaking. For a plausible range of F , the NLSP decay occurs near the interaction point or outside the detector. The decay of the NLSP inside the detector leads to very distinctive signatures of GMSB models from the gravity-mediated SUSY breaking model.

For the case of the neutralino NLSP and the gravitino LSP, the neutralino decays by $\tilde{\chi}_1^0 \rightarrow \gamma \tilde{G}$ after cascade decays of other SUSY particles to neutralinos. As it is mentioned above, the decay length could be in a range from microscopic order to the size of the detector depending on F . Because of this reason it is very important to consider the decay length in searches for the signature of GMSB models. Recently the DELPHI [6] and D0 [7] collaborations reported on the cross section limit of the chargino production with a zero lifetime decay of $\tilde{\chi}_1^0 \rightarrow \gamma \tilde{G}$.

In 1997 the LEP e^+e^- collider at CERN was run at the new center-of-mass energy (\sqrt{s}) of 183 GeV. Search for charginos and neutralinos is performed based on GMSB models considering the lifetime of $\tilde{\chi}_1^0 \rightarrow \gamma \tilde{G}$. A data set corresponding to 56.75 pb^{-1} collected with the OPAL detector in 1997 is used in this search.

In Chapter 2, an overview of the phenomenological aspects and experimental signals expected in the gauge-mediated SUSY breaking model are presented. Then the experimental apparatus and Monte Carlo event simulation are described in Chapter 3 and 4 respectively. The analysis method is presented in Chapter 5. In Chapter 6 experimental results and discussion are presented. We give the conclusion in Chapter 7.

Chapter 2

Gauge-Mediated SUSY breaking model and Experimental Signatures

In the framework of gauge-mediated SUSY breaking models, the SUSY-breaking sector is coupled to the messenger sector, which in turn couples to the visible sector through the ordinary $SU(3)_C \times SU(2)_L \times U(1)_Y$ standard-model gauge interactions. There are three remarkable signatures in this model:

- The lightest supersymmetric particle (LSP) is the gravitino.
- The sparticle masses are functions of the gauge quantum numbers and can be calculated from a small number of parameters.
- Flavour changing neutral currents (FCNC) can be automatically suppressed because the ordinary gauge interaction do not distinguish generations.

In Section 2.1 the minimal model is briefly described, in Section 2.2 phenomenology of the gravitino is given and expected experimental signatures are presented in Section 2.3.

2.1 The Minimal Model of Gauge-Mediated SUSY Breaking

The minimal model of gauge-mediated SUSY breaking [4, 5] consists of a set of messenger fields which transform as a single flavour $\mathbf{5} + \bar{\mathbf{5}}$ of $SU(5)$; i.e. there are $SU(3)_C$ triplets, q and \bar{q} , and $SU(2)_L$ doublets, ℓ and $\bar{\ell}$. These particles are called messenger (s)quarks and (s)leptons which couple to a single gauge singlet field, S , through the superpotential

$$W = \lambda_3 S q \bar{q} + \lambda_2 S \ell \bar{\ell} \quad (2.1)$$

where the field S should be thought of as a field which represents the dynamics that breaks SUSY. The scalar component and the auxiliary component of S , denoted S (also) and F_S respectively are both assumed to have vacuum expectation values (VEVs). Consequently the fermionic components of q, \bar{q} and their scalar partners get masses as

$$m_f = M \quad (2.2)$$

$$m_b = M \sqrt{1 \pm \frac{\Lambda}{M}} \quad (2.3)$$

where $M = \lambda_3 \langle S \rangle$ and $\Lambda = \langle F_S \rangle / \langle S \rangle$.

In the same manner the fermionic components of $\ell, \bar{\ell}$ get a mass M , while the scalars get masses $M \sqrt{1 \pm \Lambda/M}$, (assuming $\lambda_2 = \lambda_3$). Thus a non-zero expectation value for the scalar component of S defines the order of the masses of the messenger particles, M , and a non-zero expectation value for the auxiliary component, F_S , defines the SUSY-breaking scale within the messenger sector.

The SUSY violation which appears in the messenger spectrum is communicated to the visible sector (MSSM particles) through radiative corrections with gauge-interaction strength, as follows.

- The visible-sector gauginos obtain masses from the one-loop graph shown in Figure 2.1. The scalar (dashed) and fermion (solid) lines in the loop are messenger fields, with q, \bar{q} loops giving mass to the gluino (\tilde{g}) and the bino (\tilde{B}), and $\ell, \bar{\ell}$ loops giving mass to the wino (\tilde{W}) and bino fields. If $\langle F_S \rangle$ were 0, then the messenger scalars would be degenerate with their fermionic superpartners and there would be no contribution to the gaugino masses. For $\langle F_S \rangle \ll \lambda_i \langle S \rangle^2$, the gaugino masses at the messenger scale are given by [4]

$$m_{\lambda_i}(M) = N \frac{\alpha_i(M)}{4\pi} \Lambda \quad (2.4)$$

where for a more general messenger sector ¹ N is the equivalent number of $SU(5)$ $\mathbf{5} + \bar{\mathbf{5}}$ representations.

- The visible-sector scalars do not get any radiative corrections to their masses at one-loop order. Their masses come from the two-loop graphs as shown in Figure 2.2. In the same limit $\langle F_S \rangle \ll \lambda_i \langle S \rangle^2$, the scalar masses squared at the messenger scale are [4]

$$\tilde{m}^2 = 2\Lambda^2 N \left[C_3 \left(\frac{\alpha_3}{4\pi} \right)^2 + C_2 \left(\frac{\alpha_2}{4\pi} \right)^2 + \frac{3}{5} \left(\frac{Y}{2} \right)^2 \left(\frac{\alpha_1}{4\pi} \right)^2 \right] \quad (2.5)$$

where $C_3 = \frac{4}{3}$ for colour triplets and zero for singlets, $C_2 = \frac{3}{4}$ for weak doublets and zero for singlets, and Y is the ordinary hypercharge normalised

¹The case of $N=1$ is often called "minimal model".

as $Q = T_3 + \frac{1}{2}Y$. Those coefficients are summarised in Table 2.1 for squarks and sleptons.

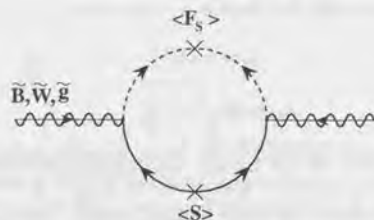


Figure 2.1: Contributions to the gaugino masses from one-loop graphs involving virtual messenger particles.

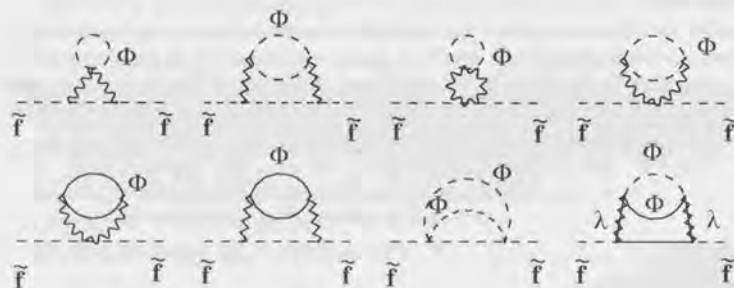


Figure 2.2: Contributions to the sfermion squared masses from two-loop graphs, where visible-sector gaugino and sfermion are denoted by λ and \tilde{f} respectively. The scalar and fermionic components of the messenger field Φ are denoted by dashed and solid lines and ordinary gauge bosons are denoted by wavy lines.

It can be clearly seen that the parameter Λ sets the global scale for the masses, and that the gaugino and scalar masses go roughly as their gauge couplings squared. The bino and right-handed sleptons gain masses only through $U(1)_Y$ interactions, therefore either can be the NLSP. The winos and left-handed sleptons, which transform under $SU(2)_L$, are somewhat heavier. The strongly interacting squarks and gluino are significantly heavier than the other sparticles. These expressions for the masses have also the following remarkable feature. In the minimal model the squark, left handed slepton, right handed slepton, and bino masses have the mass ratios

C_3	$\frac{4}{3}$	for $\tilde{q}_{R,L}$
	0	for $\tilde{\ell}, \tilde{\nu}$
C_2	$\frac{3}{4}$	for $\tilde{q}_L, \tilde{\ell}_L, \tilde{\nu}_L$
	0	for $\tilde{q}_R, \tilde{\ell}_R$

Table 2.1: Coefficients used in Equation (2.5) for squarks and sleptons.

$$m_{\tilde{q}} : m_{\tilde{\ell}_L} : m_{\tilde{\ell}_R} : m_{\tilde{B}} = 11.6 : 2.5 : 1.1 : 1.$$

Therefore the bino is natural candidate for the next-to-lightest supersymmetric particle (NLSP).

For more general case ($N \geq 1$), the gaugino masses grow proportionally to $N\Lambda$, while the scalar masses grow as $\sqrt{N}\Lambda$. For example in the case of $N=2$, the above masses are in the ratio

$$m_{\tilde{q}} : m_{\tilde{\ell}_L} : m_{\tilde{\ell}_R} : m_{\tilde{B}} = 10.6 : 2.3 : 1 : 1.3.$$

In this case the right handed slepton is the candidate for the NLSP.

Below the messenger scale the particle content is just that of the MSSM plus the light gravitino discussed in the next section. In order to translate these "boundary conditions" given at the messenger scale into physically meaningful quantities which describe physics at the electroweak scale, it is necessary to evolve the gauge couplings, superpotential parameters and mass of sparticles to low energy. This is done by utilising the renormalization group (RG) equations [16, 17]. In Figure 2.3 an example of RG evolution from in Reference [5] is shown. Here, the boundary conditions are applied with $M = \Lambda = 76$ TeV, $N = 1$ (which corresponds to $m(\tilde{B}) = 105$ GeV), $\tan \beta = 3$ and $\mu > 0$ supposing $m_{top} = 175$ GeV. It can be seen that the evolution of the up-type Higgs boson (H_u) mass squared is negative, which is caused by the contribution from stop-top loops due to the large top quark Yukawa coupling. The negative value of $m_{H_u}^2$ leads to electroweak symmetry breaking at low energy.

Imposing correct electroweak symmetry breaking gives relations among the Higgs sector mass parameters:

$$|\mu|^2 + \frac{m_{Z^0}^2}{2} = \frac{(m_{H_d}^2 + \Sigma_d) - (m_{H_u}^2 + \Sigma_u) \tan^2 \beta}{\tan^2 \beta - 1} \quad (2.6)$$

$$\sin 2\beta = \frac{-2m_{12}^2}{(m_{H_u}^2 + \Sigma_u) + (m_{H_d}^2 + \Sigma_d) + 2|\mu|^2} \quad (2.7)$$

where μ is the Higgs mixing mass, defined by the Higgs bilinear term in the superpotential

$$W = \mu H_1 H_2, \quad (2.8)$$

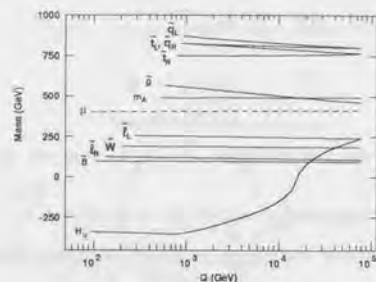


Figure 2.3: An example of the RG evolution given in Reference [5]. Input parameters for this calculation are $M = \Lambda = 76$ TeV, $N = 1$ (which corresponds to $m(\tilde{B}) = 105$ GeV), $\tan \beta = 3$ and $\mu > 0$ supposing $m_{top} = 175$ GeV.

$m_{1,2}^2$ is a SUSY-breaking counterpart of μ^2 defined by the following term in the scalar potential

$$V = m_{1,2}^2 H_1 H_2 + h.c., \quad (2.9)$$

$\tan \beta$ is the ratio of the two VEVs written as

$$\tan \beta \equiv \frac{v_u}{v_d}, \quad (2.10)$$

and $\Sigma_{u,d}$ represent finite one-loop corrections from gauge interactions and top and bottom Yukawas [15]. From these relations the absolute value of μ can be determined, although the field contents of gauginos also depends on sign of μ affecting their phenomenology. Field contents of gauginos are given in Appendix B.

Thus, with electroweak symmetry breaking imposed, the parameters of the minimal model ($N=1$) can be taken to be

$$(\tan \beta, \Lambda, \text{sign}(\mu), M)$$

For more general case, N can be another input parameter.

In Table 2.1 two examples of the mass spectrum of gauginos and sfermions are presented for $\Lambda=40$ TeV, $\mu > 0$ and $M=100$ TeV with two different N and $\tan \beta$: $N = 1, \tan \beta = 2$ and $N = 3, \tan \beta = 35$.

Finally in this section it should be mentioned about the attractive feature of the GMSB model, automatic suppression of FCNCs.

In the gravity-mediated approach, there is no obvious reason why the SUSY-breaking masses for squarks and sleptons should be flavour-invariant. The mismatch between the mass matrices for quarks and squarks (and for leptons and

² $m_{1,2}^2$ is often seen in the literature as $b, m_{1/2}^2$ or $B\mu$.

Particle	Mass (GeV)	
	$N=1, \tan \beta=2$	$N=3, \tan \beta=35$
\tilde{u}_L, \tilde{d}_L	463.7, 467.4	888.1, 891.7
\tilde{u}_R, \tilde{d}_R	446.2, 445.6	859.0, 857.3
\tilde{g}	351.6	951.6
\tilde{t}_L, \tilde{t}_R	134.5, 146.9	251.5
$\tilde{\chi}_1^\pm, \tilde{\chi}_2^0$	78.1, 82.8	270.4, 271.7
$\tilde{\ell}_R$	77.4	132.0
$\tilde{\tau}_1$	76.9	90.6
$\tilde{\chi}_1^0$	43.0	156.0

Table 2.2: The mass spectrum for two cases $N=1$ and $\tan \beta=2$, and $N=3$ and $\tan \beta=35$ under the conditions of $\Lambda=40$ TeV, $\mu > 0$ and $M=100$ TeV. $\tilde{\tau}_1$ represents the stau mass eigenstate which can be lighter than the other right handed sleptons due to the large mixing for large $\tan \beta$.

sleptons) leads to FCNC processes such as the $\mu \rightarrow e\gamma$ process or $\bar{K}^0 - K^0$ oscillations³ shown in Figure 2.4

On the other hand, in the gauge-mediated approach the masses of squarks and sleptons depend only on their gauge quantum numbers. This leads automatically to the degeneracy of squark and slepton masses among their generations which is needed to suppress the FCNC processes.

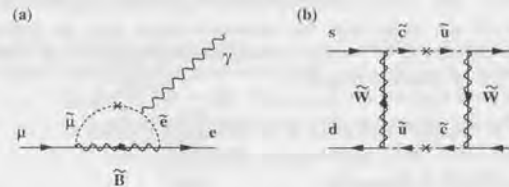


Figure 2.4: Diagrams which cause flavour violation, (a) for $\mu \rightarrow e\gamma$ and (b) for $\bar{K}^0 - K^0$ oscillation. There are similar diagrams which contributes to $\bar{K}^0 - K^0$ oscillation in which the bino and gluino are exchanged.

2.2 The Gravitino

In the presence of spontaneous SUSY breaking, the spin-3/2 gravitino (\tilde{G}) gains a mass by absorbing the spin-1/2 goldstino via the superhiggs mechanism, which

³Current limits on these processes are $Br(\mu \rightarrow e\gamma) < 4.9 \times 10^{-11}$ and $m_{\bar{K}^0} - m_{K^0} / m_{K^0} < 9 \times 10^{-19}$ [42].

is entirely analogous to the ordinary Higgs mechanism in gauge theories by which the W^\pm and Z^0 gauge bosons gain mass. The resulting \tilde{G} mass is given under the condition of vanishing cosmological constant by

$$m_{\tilde{G}} = \frac{F}{\sqrt{3}M_P} \simeq 2.4 \left(\frac{\sqrt{F}}{100 \text{ TeV}} \right)^2 \text{ eV} \quad (2.11)$$

where $M_P \simeq 2.4 \times 10^{18}$ GeV is the reduced Plank mass and \sqrt{F} is the SUSY breaking scale [8].

This means that one has very different expectations for the mass of the \tilde{G} in gravity-mediated and in gauge-mediated models, because they usually make a very different prediction for F . Since in the GMSB models the scale \sqrt{F} associated with SUSY breaking can be as low as 10 TeV, the gravitino is naturally the LSP. Therefore if R -parity [9] is conserved, the NLSP which is thought to be a candidate of the LSP in the gravity-mediated model will decay to its partner and the gravitino.

The corresponding interaction Lagrangian for NLSP decays is given by

$$\tilde{L} = -\frac{1}{F} j^{\alpha\mu} \partial_\mu G_\alpha + h.c. \quad (2.12)$$

where $j^{\alpha\mu}$ is the supercurrent [10].

As can be seen, the coupling is suppressed by $1/F$ compared to electroweak and strong interactions. This makes decay to the \tilde{G} significant only for the NLSP. However it should be also noted that the coupling is larger than the gravitational coupling which is suppressed by $1/M_P$, possibly leading to the NLSP decay with detectable decay length inside a detector.

As discussed in the previous section, in the GMSB model the NLSP is either a neutralino ($N=1$)⁴ or a right-handed slepton ($N>1$). When the lightest neutralino, $\tilde{\chi}_1^0$, is NLSP, it decays by

$$\tilde{\chi}_1^0 \rightarrow \gamma \tilde{G}$$

while a right-handed slepton, $\tilde{\ell}_R$, NLSP decays by

$$\tilde{\ell}_R \rightarrow \ell \tilde{G}.$$

The decay width of $\tilde{\chi}_1^0 \rightarrow \gamma \tilde{G}$ is written, if it is mostly bino, \tilde{B} , as [12, 13]

$$\Gamma(\tilde{\chi}_1^0 \rightarrow \gamma \tilde{G}) = \frac{\cos^2 \theta_W m_{\tilde{\chi}_1^0}^5}{16\pi F^2}. \quad (2.13)$$

⁴For large $\tan \beta$, due to the mixing between left and right handed states, the stau ($\tilde{\tau}$) can be the NLSP. This is discussed in Section 6.3.

This translates to a decay length

$$c\tau \simeq 130 \left(\frac{100 \text{ GeV}}{m_{\tilde{B}}} \right)^5 \left(\frac{\sqrt{F}}{100 \text{ TeV}} \right)^4 \mu\text{m}. \quad (2.14)$$

Accordingly there is a range of \sqrt{F} and $m_{\tilde{B}}$ for which the decay occurs within a detector, with the gravitino carrying off missing energy. The allowed lifetime range is determined by the maximum and minimum allowed \sqrt{F} in Equation (2.14). Requiring $\sqrt{F} < 10^{10}$ GeV avoids a mixed gravity- and gauge-mediated scenario, and thus the re-introduction of potential unsuppressed FCNCs associated with gravity-mediated SUSY breaking. Cosmological considerations may be further restrictive, preferring $\sqrt{F} < 2 \times 10^6$ GeV [13]. The lower limit is also uncertain, but $\sqrt{F} > 10^4$ GeV is preferred [13]. With a recent model $\sqrt{F} \simeq 10^5 - 10^6$ is obtained by imposing superpartner mass $m_{SUSY} \simeq 10^2 - 10^3$ GeV [14].

In principle, one can also have $\tilde{\chi}_1^0 \rightarrow Z\tilde{G}$ or $h^0\tilde{G}$, but the corresponding decay width suffer a strong kinematical suppression and can be shown to be always negligible [11]. In the rest frame of the decaying $\tilde{\chi}_1^0$, the photon is produced isotropically (independent of the spin of $\tilde{\chi}_1^0$) with energy equal to $m_{\tilde{\chi}_1^0}/2$.

For a slepton NLSP, the decay length of $\tilde{\ell} \rightarrow \ell + \tilde{G}$ has a similar order depending on \sqrt{F} and $m_{\tilde{\ell}}$.

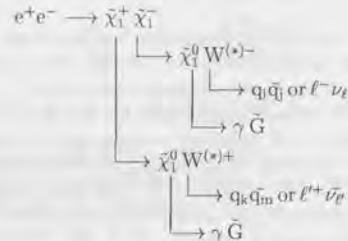
2.3 Experimental Signature

The decay of the NLSP to its partner plus the \tilde{G} within a detector leads to very distinctive signatures. If such signatures were established experimentally, one of the most important challenges would be to measure the distribution of final path lengths for the NLSP, thereby giving a direct measurement of the SUSY-breaking scale.

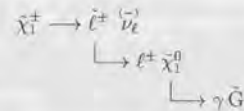
2.3.1 Neutralino NLSP

In the minimal GMSB model, $\tilde{\chi}_1^0$ is the candidate of the NLSP and decays by $\tilde{\chi}_1^0 \rightarrow \gamma \tilde{G}$ if R -parity is conserved. Assuming it decays in a detector, the signatures for SUSY are $\gamma\gamma + X + (\text{missing energy})$, where X arises from cascade decays to $\tilde{\chi}_1^0$. Since in the GMSB model squarks are much too heavy to be relevant to discovery, it is the electroweak states that could be produced. In these signatures both the missing energy and photon energies are typically greater than $m_{\tilde{\chi}_1^0}/2$ and the photons are generally isolated. The background events from initial- and final- state radiation typically does not have isolated photons with such high energy except the "radiative-return" events in which the initial state photons are radiated to reduce the effective center-of-mass energy to $m_{\mu\mu}$.

In the case of $\tilde{\chi}_1^+ \tilde{\chi}_1^-$ pair production, which is expected to have large production cross section in e^+e^- colliders, the following cascade decay to $\gamma\tilde{G}$ from $\tilde{\chi}_1^\pm$ is expected:

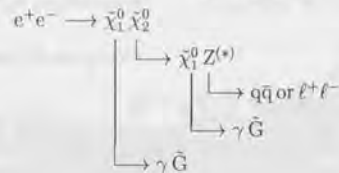


There appears three types of topologies in final states depending on the decay mode of $W^{(*)\pm}$ as schematically shown in Figure 2.5. If the mass of slepton, $m_{\tilde{\ell}}$, is lighter than $m_{\tilde{\chi}_1^\pm}$, it is also possible that $\tilde{\chi}_1^\pm$ perform cascade decay like the following⁵.



This means that we cannot always assume that the branching fraction of $\tilde{\chi}_1^\pm \rightarrow W^{(*)\pm} \tilde{\chi}_1^0$ is equal to 100%. $\text{Br}(\tilde{\chi}_1^\pm \rightarrow \ell^\pm \bar{\nu}_\ell \tilde{\chi}_1^0)$ should be a free parameter.

In the case of $\tilde{\chi}_2^0 \tilde{\chi}_1^0$ production, $\tilde{\chi}_2^0$ and $\tilde{\chi}_1^0$ decay by



The final state containing two energetic photons and jets or lepton pairs which arise from decay of $Z^{(*)}$ would be observed with missing energy carried by the

⁵If $m_{\tilde{\ell}}$ is lighter than $m_{\tilde{\chi}_1^\pm}$, it is also possible that $\tilde{\chi}_1^\pm \rightarrow \tilde{\nu} \ell^\pm$ and $\tilde{\nu} \rightarrow \nu \tilde{\chi}_1^0$ followed by the decay of $\tilde{\chi}_1^0$ to $\gamma\tilde{G}$. This case also has the same final topology shown above.

\tilde{G} . They are shown schematically in Figure 2.6. When $Z^{(*)}$ decays to a pair of neutrinos, the final state is acoplanar di-photon which is not searched for in the analysis of this work. The same kind of the final topology is expected when $\tilde{\chi}_1^0$'s are produced in pair and each $\tilde{\chi}_1^0$ decays as $\tilde{\chi}_1^0 \rightarrow \gamma\tilde{G}$, which is searched in Reference [18]. Although $\tilde{\chi}_2^0 \tilde{\chi}_1^0$ productions with these decays have not been directly searched for, the analysis presented in Reference [18] would have sensitivity.

2.3.2 Slepton NLSP

It is possible within non-minimal models that a right-handed slepton is the NLSP, which decays by

$$\tilde{\ell}_R \longrightarrow \ell \tilde{G}.$$

In this case the signature for SUSY is $\ell^+\ell^- + X + (\text{missing energy})$. The decay $\tilde{\ell} \rightarrow \ell\tilde{G}$ over a macroscopic distance would give rise to the signature of a greater than minimum ionising track with a kink to a minimum ionising track. If the decay takes place well outside the detector, the signature for SUSY is heavy charged particles rather than the missing energy [19]. On the other hand, short decay length of $\tilde{\ell}$ would provide the signature of acoplanar di-lepton [20] in slepton pair production. It can be also expected that $\tilde{\chi}_1^0$'s are produced in pair through \tilde{e} exchange and they decay to $\tilde{\ell}\tilde{\ell}$ followed by the decay of $\tilde{\ell} \rightarrow \ell\tilde{G}$ resulting in the final state of 4 leptons + (missing energy). Furthermore in the case of the second-lightest slepton production, $e^+e^- \rightarrow \tilde{\ell}_s \tilde{\ell}_s$, the $\tilde{\ell}_s$ decays to $\tilde{\ell}_f \tilde{\ell}_f$ followed by the decay of $\tilde{\ell}_f$ to $\ell_f \tilde{G}$, leading to 6 leptons + (missing energy) in the final state, where $\tilde{\ell}_s(\tilde{\ell}_s)$ is the second-lightest slepton (its partner) and $\tilde{\ell}_f(\tilde{\ell}_f)$ is the lightest slepton (its partner). The decay length of the lightest slepton should be considered in such analyses.

The process $e^+e^- \rightarrow \tilde{G}\tilde{G}\gamma$ might be able to be detected in LEP2 if the \tilde{G} is very light as predicted by the GMSB models even when the other particles are heavy and can not be detectable [46]. Since the \tilde{G} interaction with the other particles depends on the SUSY breaking scale, \sqrt{F} , measurement of the single photon production in the excess of the standard-model processes such as $e^+e^- \rightarrow \nu\nu\gamma$ can directly set the limit on the breaking scale.

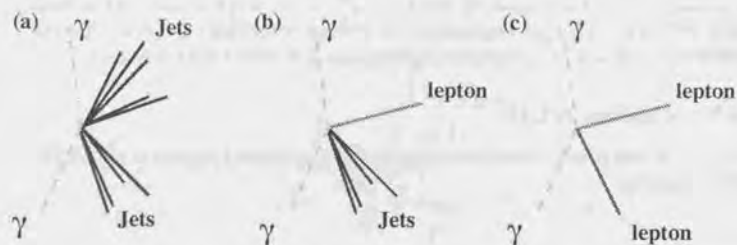


Figure 2.5: A schematic view of the final topologies for $\tilde{\chi}_1^+ \tilde{\chi}_1^-$ pair production with $\tilde{\chi}_1^0 W^{*\pm}$ decays of $\tilde{\chi}_1^\pm$ followed by $\gamma \tilde{G}$ decay of the $\tilde{\chi}_1^0$. For the decays of $\tilde{\chi}_1^\pm$ only through $W^{*\pm}$, rates for (a), (b) and (c) are in the ratio 45% : 44% : 11%, where (a) for both $W^{*\pm}$ decaying to hadrons, (b) for one to hadrons and the other to leptons and (c) for both to leptons.

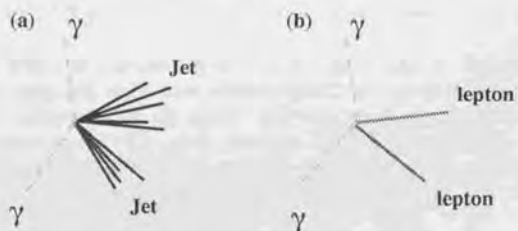


Figure 2.6: A schematic view of the final topologies for $\tilde{\chi}_2^0 \tilde{\chi}_1^0$ production with $\tilde{\chi}_1^0 Z^{(*)}$ decay of the $\tilde{\chi}_2^0$ followed by $\gamma \tilde{G}$ decay of $\tilde{\chi}_1^0$. (a) for hadronic decay of $Z^{(*)}$ and (b) for leptonic decay except invisible decay of $Z^{(*)}$.

Chapter 3

Experimental Apparatus

3.1 Accelerator

The CERN Large Electron Positron (LEP) collider is a e^+e^- storage ring with 26.67 km circumference. This collider was built to investigate the electroweak interaction with high precision. In the first phase (LEP1), the collider was operated around the center-of-mass energy of Z^0 resonance (~ 91 GeV) and it produced a large number of Z^0 bosons. From the analyses of Z^0 decay products, many important physics results, such as a precision measurement of the mass of Z^0 boson, have been obtained. In 1996, installing 144 superconducting cavities for the operation above the W^+W^- production threshold (≥ 161 GeV), LEP entered the second phase (LEP2). After the summer shutdown in 1996 for installation of additional 32 superconducting cavities, the center-of-mass energy of 172 GeV was reached. In 1997 the energy is raised to 183 GeV by installing 64 more superconducting cavities.

Extensive searches for new particles as well as the measurement of mass of the W boson have been performed at LEP2.

A brief summary of the structure of the LEP and the accelerating system for LEP2 are described below.

3.1.1 Structure

The LEP storage ring consists of eight straight sections connected by the same number of curved sections. The ring is situated underground, in a tunnel of 3.8 m diameter, at an average depth of 100 m from the ground. Electrons and positrons are constrained in the vacuum chamber along the nominal orbit by the electromagnetic field guide system. The system consists of dipole, quadrupole and sextupole magnets, dipole correctors in horizontal and vertical directions, rotated quadrupoles, and electrostatic deflectors. The curved sections are occupied by sets of standard cells consisting of these magnets. The beams are bent in the

dipole field of about 0.1 T, which is unusually low in a circular accelerator, in order to reduce the energy loss due to synchrotron radiation while bending. In a circular orbit, the energy radiated by an electron or positron per turn is given by

$$\Delta E = \frac{4\pi}{3} \frac{e^2 \beta^2 \gamma^4}{\rho} \propto \frac{E^4}{\rho} \quad (3.1)$$

where ρ is the bending radius, β is the particle velocity, $\gamma = (1 - \beta^2)^{-1/2}$, and E is the particle energy. Consequently, larger radius results in smaller loss of the energy in addition to lower magnetic field to bend the beams. However reaching higher energy, one needs more power to accelerate and maintain the beams in the orbit due to the radiation increasing in proportion to E^4 .

Four interaction regions located in the middle of the straight sections are surrounded by solenoidal magnets used by the detectors of the experiments. Beams are focused tightly at the interaction points by the strong quadrupole field generated by a set of superconducting magnets to obtain high luminosity. Typical transverse dimension of the beam at an interaction point is about $10 \mu\text{m} \times 250 \mu\text{m}$ in the vertical and horizontal plane respectively. The longitudinal dimension is typically $\sim 2 \text{cm}$.

3.1.2 Accelerating System

The LEP storage ring is the last in a chain of five accelerators. Electrons are generated at the end point of a 200 MeV linac and are accelerated by the electrostatic field. Positrons are generated by the positron converter which converts some of the accelerated electrons into the positrons. Electrons and positrons are then accelerated up to 600 MeV by a linac. Accelerated particles are injected into the Electron-Positron Accumulating ring (EPA). The role of this ring is to generate bunches for electrons and positrons with a high intensity and a constant energy. The high-intensity beams are transported to the CERN Proton Synchrotron (CERN-PS) which accelerates the beams up to 3.5 GeV. The PS injects the beams into the next circular accelerator, Super Proton Synchrotron (CERN-SPS), operated as a electron-positron injector for LEP. Particles are further accelerated up to 20 GeV in this ring and finally they are transported to the LEP ring. After the transportation, the LEP accelerating system accelerates the bunches up to the full energy required for collisions. As explained above, old accelerators in CERN are utilized in practical way and being operated in good performance.

Since the particles are constrained to a circular motion, they continually lose energy through the emission of synchrotron radiation. In order to compensate this energy loss and maintains the beams in their orbit, the Radio-Frequency (RF) accelerator cavities are installed in the straight section of the LEP ring. In LEP2, RF cavities made of superconducting material are employed to reduce the

power dissipation as heat in the cavities and to achieve the higher beam energy. Performance of LEP2 during the runs in 1997 is summarized in table 3.1.2.

Beam Energy	91.4 GeV
Acceleration Voltage	2301 MV
Number of Bunch/Beam	4
Maximum Current	5.2mA
Peak Luminosity (Integrated)	$\sim 5 \times 10^{31} \text{cm}^{-2}\text{s}^{-1}$ ($\sim 100 \text{nb}^{-1}/\text{hour}$ $\sim 2 \text{pb}^{-1}/24 \text{hours}$)

Table 3.1: Performance of LEP2 during the runs in 1997.

3.2 The OPAL detector

The OPAL detector [21], one of the four large detectors installed at the LEP storage ring, is a multipurpose apparatus surrounding the beam pipe with its center at the nominal interaction point and having nearly complete solid angle coverage.

The main part of the detector consists of many subdetectors classified into five elements according to their characteristics:

- A central detector to measure the positions, directions, momenta and energy loss of charged particles.
- An electromagnetic calorimeter to measure the energies of electrons and photons.
- A hadron calorimeter to measure the energies of hadrons which pass through the electromagnetic calorimeter.
- A muon detector to identify muons by measuring their positions and directions behind the hadron calorimeter.
- A forward detector to measure the luminosity by counting small angle Bhabha scattering events.

A schematic view of the general layout of the detector system is shown in Figures 3.1. Figure 3.2 shows the cross-sectional view of the detector in the x - y and z - x planes.

A right-handed coordinate system is adopted, where the z -axis points to the center of the LEP ring, and positive z is along the electron beam direction. The angles θ and ϕ are the polar and azimuthal angles, respectively.

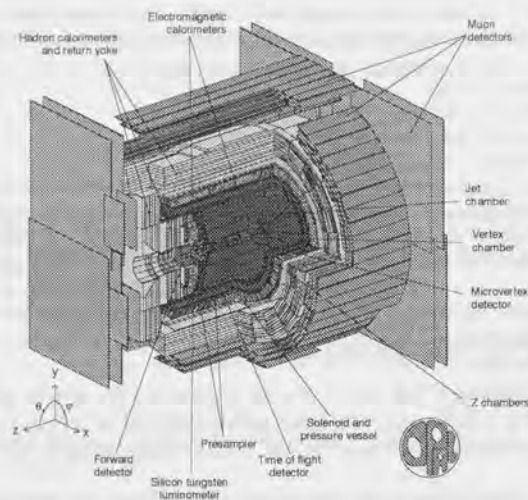


Figure 3.1: Schematic view of the OPAL detector.

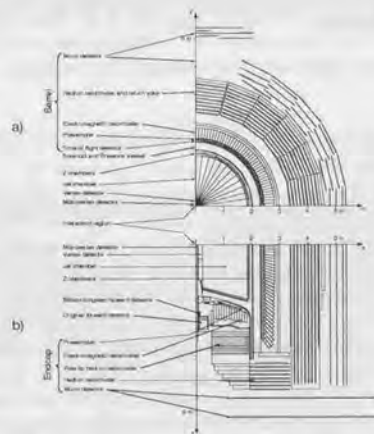


Figure 3.2: Cross-sectional views of the OPAL detector (a) perpendicular to the beam and (b) parallel to the beam.

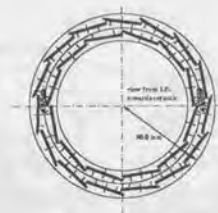


Figure 3.3: Front view of SI detector. Each ladder is tilted to close ϕ gaps by 5.5 degree in the inner layer and 7.5 degree in the outer layer.

3.2.1 Magnet

A solenoidal coil surrounding the central detector which provides a uniform magnetic field parallel to the beam is installed. The coil is made of aluminum supported by itself to reduce the amount of material, since electrons and photons need to pass through it without interaction before reaching the electromagnetic calorimeter. The thickness of the coil is 96 mm of Al and 54 mm of glass epoxy, which corresponds to 1.7 radiation lengths. The iron return yoke is made of soft iron plates, which serves also as the absorption material of the hadron calorimeter. (see Section 3.2.4.)

The magnetic field in the central detector volume is 0.435 T with the uniformity of $\pm 0.5\%$.

3.2.2 Central Tracking System

The central tracking system consists of a silicon microvertex detector (SI), a vertex drift chamber (CV), a jet chamber (CJ) and z -chambers (CZ). The whole tracking system is located inside the solenoid coil.

Silicon Microvertex Detector

The silicon microvertex detector (SI) consists of two barrels of ladders at radii of 6.1 and 7.5 cm respectively. The inner layer consists of 12 ladders and the outer one of 15, tilted to close ϕ gaps as shown in Figure 3.3. Each ladder is 30 cm long and consists of 5 silicon wafers which are assembled by gluing $r-\phi$ and $r-z$ wafers back to back. The strip has $25 \mu\text{m}$ pitch and the signal is read out at $50 \mu\text{m}$ pitch in $r-\phi$ and $100 \mu\text{m}$ pitch in $r-z$.

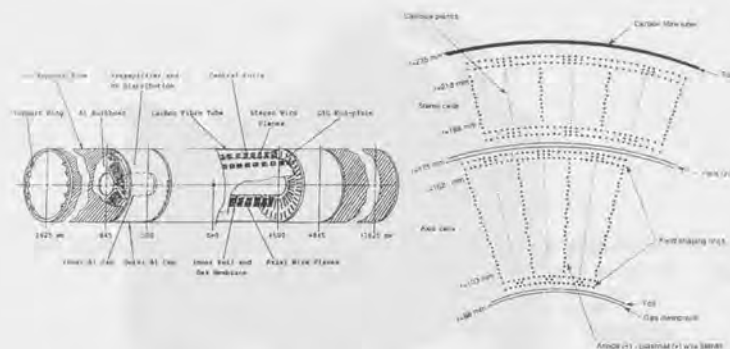


Figure 3.4: Schematic view of CV and its wire layout at one end plate.

Vertex Drift Chamber

The vertex drift chamber (CV) is a high precision cylindrical jet drift chamber. It is 100 cm long with a radius of 23.5 cm and consists of two layers of 36 ϕ sectors each. The inner layer contains the axial sectors, each of which contains a plane of 12 sense wires strung parallel to the beam direction. The outer layer contains the stereo sectors each containing a plane of 6 sense wires inclined at a stereo angle of about 4 degree. The r - ϕ position of a track is measured by the drift time sensed by the axial wires and the z position is measured by combining the information from axial and stereo wires. Figure 3.4 shows a schematic view of CV and its wire layout at one end plate. Spatial resolution of the r - ϕ position σ is obtained to be about $50 \mu\text{m}$.

Jet Chamber

The jet chamber (CJ) is a cylindrical drift chamber of length 400 cm in z with an outer radius of 185 cm and inner of 25 cm. The chamber consists of 24 identical sectors each containing a sense wire plane of 159 wires strung parallel to the beam direction. The signal wires are positioned at radii between 255 mm and 1835 mm with a 10 mm spacing, alternating with potential wires. The signal wires are staggered alternately by $\pm 100 \mu\text{m}$ to resolve left-right ambiguity. The coordinates of wire hits in the r - ϕ plane are determined from the drift time. The z -coordinate is measured using a charge division technique. The sum of the charges received at both end of a wire gives information on the energy loss dE/dx . Figure 3.5 shows a plot of dE/dx versus momentum. In the range $|\cos \theta| < 0.73$, 159 points can be measured along each track. More than 20 points on a track can be used for the measurement over 96% of the full solid angle. Measurements of the curvatures of

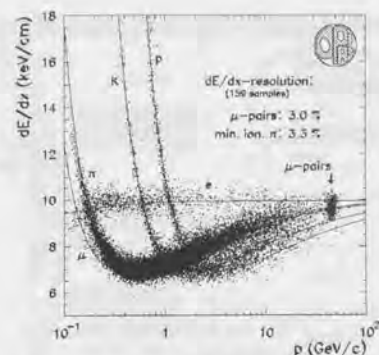


Figure 3.5: dE/dx versus momentum for multi-hadrons and muon-pairs together with the expected values. Each track is required to have more than 130 wire hits for dE/dx measurement. The dE/dx resolutions for minimum ionising pions ($p = 0.4 - 0.8 \text{ GeV}/c$) and muon-pairs with 159 wire hits are also indicated.

the tracks provide precise momentum determination. The momentum resolution is given by

$$\frac{\sigma_{p_t}}{p_t} = 1.4 \times 10^{-3} p_t (\text{GeV}) \oplus 0.02$$

including a term due to multiple scattering.

z -Chamber

The z -chambers (CZ) are a set of thin drift chambers which provide the precise measurement of the z -coordinates of tracks as they leave CJ. They consist of a layer of 24 drift chambers with 4 m length and 0.5 m width arranged to form a barrel. The chambers cover 94% of the azimuthal angle within the polar angle range $|\cos \theta| < 0.72$. Each chamber is divided in z into eight cells, covering $50 \text{ cm} \times 50 \text{ cm}$, containing a plane of six sense wires strung in the ϕ direction. The θ angle is measured by the drift time and ϕ angle is by the charge division technique. When they are installed in the OPAL detector, θ angle resolution of 3 mrad and ϕ position resolution of about 1.5 cm are obtained.

A cut-away drawing which shows the arrangement of SI, CV, CJ and CZ is given in Figure 3.6.

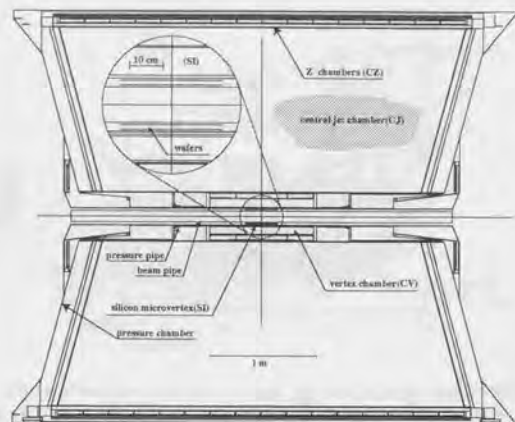


Figure 3.6: Cut-away drawing to show the arrangement of the components of the central tracker.

3.2.3 Electromagnetic Calorimeter

A lead-glass electromagnetic calorimeter (ECAL) providing acceptance for $|\cos\theta| < 0.984$ together with presamplers and time-of-flight scintillators (TOF) is located outside the magnet coil and at the front of both endcaps.

Barrel Electromagnetic Calorimeter

The barrel electromagnetic calorimeter (EB) covers the geometrical region of $|\cos\theta| < 0.82$. Each lead glass block is made of SF57 [24] which has a density of 5.54 g/cm^3 . The depth of the block is 37 cm, which corresponds to 24.6 radiation lengths. Figure 3.7 shows the assembly of a block. The calorimeter is segmented

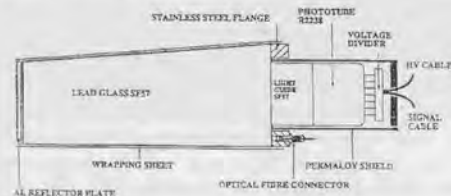


Figure 3.7: Schematic view of a block of barrel electromagnetic calorimeter

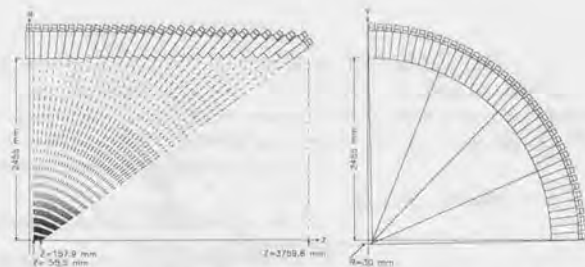


Figure 3.8: The set up of blocks in EB. The longitudinal axis of each block points at the interaction region with slight offset. In the z direction, each block points to different z position ($|z|=55.5-157.9 \text{ mm}$) along the beam axis depending on its position. In the ϕ direction, the blocks are tilted by 0.574° so that they miss the beam axis by 30 mm.

into 59×160 blocks in z and ϕ directions respectively. The blocks are arranged in a nearly-pointing geometry to the interaction region with slight offset in order to prevent incoming particles from escaping in the gaps between the blocks. The set up of the blocks in EB is shown in Figure 3.8. The energy resolution during the runs in 1997 is expressed as

$$\frac{\sigma_E}{E} = \frac{10.1\%}{\sqrt{E}} \oplus 0.7\% \quad (3.2)$$

For 50 GeV electrons injected normal to the counters, a position resolution was obtained to be 2.4 mm in a test beam.

Endcap Electromagnetic Calorimeter

The Endcap Electromagnetic Calorimeter (EE) covers the region of $0.81 < |\cos\theta| < 0.98$. The blocks are 38, 42 and 52 cm long, and arranged so that the total depth of the counter seen by particles from the interaction region is at least 20.5 and typically 22 radiation lengths. They are mounted with their axes parallel to the beam direction. The lead glass used is CEREN-25 [25] which has a density of 4.06 g/cm^3 . Figure 3.9 shows a schematic view of a counter assembly. Total of 1132 lead glass counters are arranged in a dome-shape array as shown in Figure 3.10. The energy resolution of the endcap calorimeter at low energies, studied in pion and electron beams, is $\sigma_E/E = 5\%/\sqrt{E}$ where E is in GeV. The response was measured to be linear with the accuracy of $\sim 1\%$ in the energy range of 3 to 50 GeV.

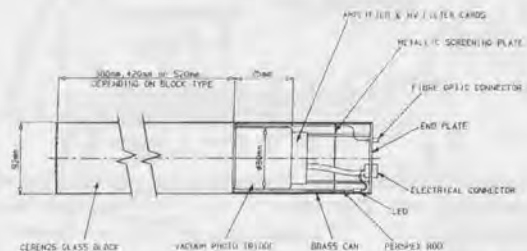


Figure 3.9: Schematic view of a block of endcap electromagnetic calorimeter

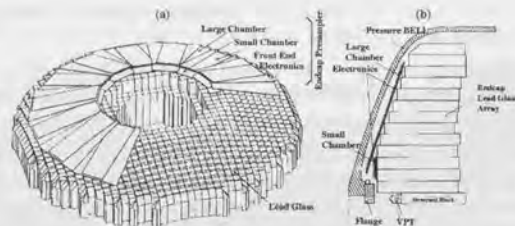


Figure 3.10: Schematic views of the endcap electromagnetic calorimeter (a) in 3-D view, and (b) in a cross-section parallel to the beam direction. The endcap presampler and pressure bell for the central tracker are also shown.

3.2.4 Hadron Calorimeter

The magnet return yoke is instrumented for hadron calorimetry (HCAL) giving a polar angle coverage of $|\cos\theta| < 0.99$. HCAL consists of three parts, barrel, endcap and pole tip hadron calorimeters. Two of them have essentially the same design, located each in the barrel and endcap regions respectively. The energy resolution is $120\%/\sqrt{E}$ for all of them.

Barrel and Endcap Hadron Calorimeter

In the barrel region $|\cos\theta| < 0.81$ the calorimeter consists of 9 layers of chambers with streamer tubes alternating with 8 iron slabs of 100 mm in thickness, which corresponds to 4.8 interaction length. The endcap hadron calorimeters cover the ends of the barrels, $0.81 < |\cos\theta| < 0.91$, with 8 layers of chambers and 7 iron slabs of 100 mm in thickness. The total thickness of the iron absorber corresponds to 4.2 interaction lengths.

Pole Tip Hadron Calorimeter

At the end of the endcap hadron calorimeter the pole tip hadron calorimeter is installed up to the polar angle of $0.91 < |\cos\theta| < 0.99$. It consists of 10 active layers with multiwire proportional chambers alternating with 9 iron slabs of 80 mm in thickness. The total thickness of the iron absorber corresponds to 4.3 interaction lengths.

3.2.5 Muon Detector

The muon detector (MU) is located at the outer side of HCAL covering more than 93% of the full solid angle. Before entering the muon detector, most hadrons from the interaction region traverse material of more than 7 interaction length. Muons are identified by extrapolating the track detected in the central detector to the muon detector within the tolerance caused by energy loss and multiple scattering in the absorber.

3.2.6 Silicon Tungsten Calorimeter

The silicon tungsten calorimeter (SW) is a sampling calorimeter designed to detect small-angle Bhabha-scattering events in order to measure the luminosity. SW is located on both sides at ± 238.94 cm from the interaction point on the z-axis, and covers the geometrical acceptance of 59 mrad to 24 mrad in polar angle. A schematic view of SW is shown in figure 3.11. Each calorimeter consists of 19 layers of silicon detectors and 18 layers of tungsten. At the front of each

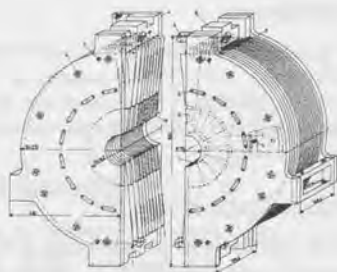


Figure 3.11: Schematic view of SW. They are located on both sides at ± 238.94 cm from the interaction point on the z -axis.

calorimeter is a bare layer of silicon to detect preshowering, the next 14 silicon layers are each behind 3.8 mm (1 radiation length) of tungsten and the final 4 layers are behind 7.6 mm (2 radiation length) of tungsten. Each silicon layer consists of 16 wedge shaped silicon detectors. The wedges cover 22.5 degree in ϕ with an inner radius of 6.2 cm and an outer one of 14.2 cm. The wedge is subdivided into 64 parts (32 in r and 2 in ϕ) giving a total of 38912 channels which are read out individually. Adjacent wedges in a layer are offset by $800 \mu\text{m}$ in z and positioned in such a way that there is no gap in the active area of the silicon. Consecutive layers in the detector are offset in ϕ by a half wedge so that any cracks between the tungsten half-rings do not line up. The relative experimental error of the absolute luminosity at LEP1 measured with the SW luminometer is 3.3×10^{-4} . This includes all intrinsic and time-dependent sources of experimental uncertainty such as detector geometry, gain variations, energy and positional biases in the detector response to electromagnetic showers, variations in the beam geometry, backgrounds and other environmental influences.

3.2.7 Forward Calorimeter

The forward calorimeter (FD) consists of 16 segments located at both sides and covers the acceptance of 37 to 154 mrad from the beam pipe. Each segment is composed of 35 sampling layers of lead-scintillator sandwiches divided into a presampler of 4 radiation lengths and the main calorimeter of 20 radiation lengths. It is located behind SW at both sides.

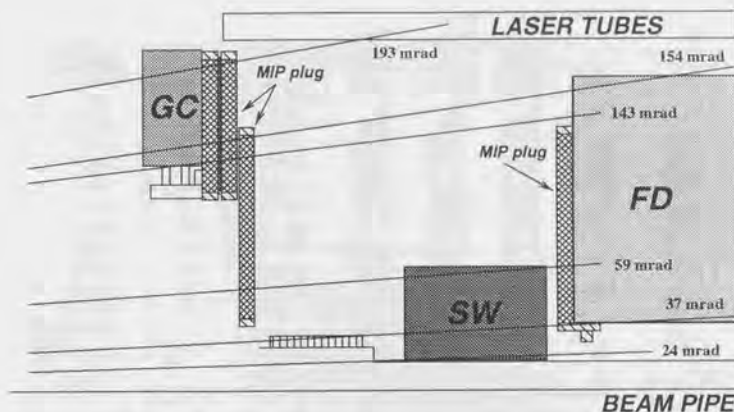


Figure 3.12: Schematic view of the layout of SW, FD and GC. MIP plugs which were installed in 1997 are also shown.

3.2.8 Gamma Catcher

The gamma catcher (GC) is a ring of lead scintillator sandwich sections of 7 radiation length, located in front of SW at both sides. They cover the acceptance of 143 to 193 mrad from the beam pipe, thus filling the gap between EE and FD. The detector has a linear response to the energy of electromagnetic shower up to 5 GeV. Any electrons or photons with the energy of more than 2 GeV can be detected, thus providing an efficient veto for radiative events.

Schematic view of the layout of SW, FD and GC is shown in Figure 3.12¹.

3.2.9 Trigger

Events are only recorded by the data acquisition system if they satisfy certain trigger conditions. The detail of the OPAL trigger system can be found in Reference [22].

The trigger signals from subdetectors divide into two complementary parts, "stand-alone" and " θ - ϕ matrix" signals. Information from a single detector component is used for the stand-alone trigger signals such as total energy measured by ECAL or track multiplicities provided by the track trigger (TT)² and pro-

¹In 1997, 4 layers of scintillator tiles (MIP plugs) were installed in both endcaps of the OPAL detector. The main purpose of these tiles is to detect the presence of minimum ionizing particles at small angle to the beam axis. They are not used in the analysis of this work.

²The track trigger [23] uses information from the 12 axial wires of each sector of CV and

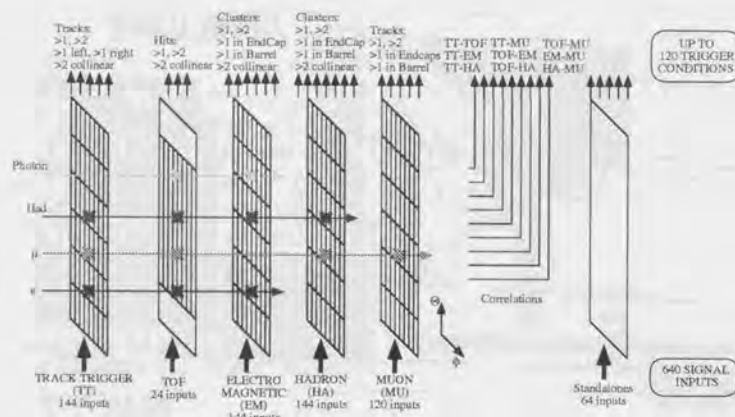


Figure 3.13: Overview of trigger generation by the θ - ϕ matrix.

vides relatively high thresholds. In order to allow lower thresholds and spatial coincidences between components, the detector has been subdivided into θ and ϕ elements (" θ - ϕ matrix"). The θ - ϕ matrix is composed of overlapping bins in polar and azimuthal angles. The full azimuthal range is covered by 24 bins, the polar range by 6 bins. The matrix has 5 "layers" corresponding to the track, time-of-flight, electromagnetic, hadron and muon triggers. The matrix provides spatial correlations of hits within and between subdetector layers. This is shown schematically in Figure 3.13.

Trigger signals which were utilized during the runs in 1997 are listed in Table 3.2.9 for stand-alone trigger signals and in Table 3.2.9 for θ - ϕ matrix outputs. The trigger rate during the data taking was 5~6 Hz with a typical readout dead-time of 20 msec.

from three groups of 12 adjacent wires at different radii of each CJ sector. Signals formed by CV and CJ trigger electronics are combined by the track trigger processor, which detects the presence of tracks in any bins of the θ - ϕ matrix and provides various track multiplicity signals. In addition, simple counts of the number of hit wires are provided, and trigger signals depending on the specific ionisation of particles are available from the CJ electronics.

Name	Detector	Signal description
TM1	TT	≥ 1 track
TM2	TT	≥ 2 tracks
TM3	TT	≥ 3 tracks
TBM1	TT	≥ 1 barrel track
TBM2	TT	≥ 2 barrel tracks
TBM3	TT	≥ 3 barrel tracks
J1H	TT	≥ 8 hists in jet chamber ring 1
J2H	TT	≥ 8 hists in jet chamber ring 2
J3H	TT	≥ 8 hists in jet chamber ring 3
VXH	TT	Number of CV hits/wires above threshold
VXH2	TT	Number of CV hits/wires above threshold
QUARK	CJ	track with low charge
MONOPOL	CJ	track with high charge
TOVCV	TOF	back-to-back in 9° TOF segments
TOV2V2	TOF	back-to-back in overlapped 9° segments
EBWEDGE	ECAL	Sum 'wedge' of EB above threshold (2 GeV)
EBTOTH	ECAL	Total EM energy in barrel-High threshold (≥ 5 GeV)
EELHI	ECAL	ECAL energy in left endcap-High threshold (≥ 2.4 GeV)
EERHI	ECAL	ECAL energy in right endcap-High threshold (≥ 2.4 GeV)
EBTPHI	ECAL	OR of θ - ϕ in barrel (≥ 1.8 GeV)
EBTOTLO	ECAL	Total ECAL energy in barrel-Low threshold (≥ 1.8 GeV)
EELLO	ECAL	ECAL energy in left endcap-Low threshold (≥ 1.6 GeV)
ERLO	ECAL	ECAL energy in right endcap-Low threshold (≥ 1.6 GeV)
MELR	MU	≥ 1 muon in left AND right endcaps
MBH	MU	≥ 1 muon in barrel
MEL	MU	≥ 1 muon in left endcap
MER	MU	≥ 1 muon in right endcap
SWHIOR	SW	energy of single end ≥ 34 GeV
SWSEG	SW	Back-to-back segment coincidence (9 GeV)
SWSUM	SW	Low threshold(4 GeV) AND of two sides
SWSEGL	SW	energy of left segment ≥ 9 GeV
SWSEGR	SW	energy of right segment ≥ 9 GeV
SWLOL	SW	energy of left segment ≥ 4 GeV
SWLOR	SW	energy of right segment ≥ 4 GeV
FDSUM	FD	energy sum of left AND right ≥ 15 GeV
FDSEG	FD	coincidence left and right segments ≥ 13 GeV
FDHIOR	FD	one-sided FD ≥ 35 GeV
LCALLO	FD	energy in left FD ≥ 15 GeV
RCALLO	FD	energy in right FD ≥ 15 GeV
FDGCLT	GC	Gamma catcher left tag
FDGCRT	GC	Gamma catcher right tag
BXRSA	BX	Stand-alone random trigger (0.1 Hz)
BXR	BX	Random beam crossing (4 Hz)

Table 3.2: Stand-alone trigger signals provided by the subdetectors which were utilized during data taking in 1997. TT and BX denote the track trigger and the random trigger respectively.

Name	Detector	Trigger condition
TPTTB	TT	$\geq 1 \theta$ - ϕ bin in barrel
TPTT1	TT	$\geq 1 \theta$ - ϕ bin
TPTT2	TT	≥ 2 independent θ - ϕ bins
TP TTL	TT	$\geq 1 \phi$ bin in θ_1
TP TTR	TT	$\geq 1 \phi$ bin in θ_5
TP T T CL	TT	≥ 1 pair of collinear tracks
TP T T TO	TT AND TOF	≥ 1 correlated θ - ϕ bin
TP T TEM	TT AND ECAL	≥ 1 correlated θ - ϕ bin
TP T THA	TT AND HCAL	≥ 1 correlated θ - ϕ bin
TP T TMU	TT AND MU	≥ 1 correlated θ - ϕ bin
TP TO1	TOF	$\geq 1 \theta$ - ϕ bin
TP TO2	TOF	≥ 2 independent θ - ϕ bins
TP TO CL	TOF	≥ 1 pair of coplanar hits
TP TO CAP	TOF	endcap coincidence
TP TO EM	TOF AND ECAL	≥ 1 correlated θ - ϕ bin
TP TO MUR	TOF AND MU	≥ 1 correlated θ - ϕ bin
TP TO MU	TOF AND MU	≥ 1 correlated θ - ϕ bin in barrel
TP EM1	ECAL	$\geq 1 \theta$ - ϕ bin
TP EM2	ECAL	≥ 2 independent θ - ϕ bins
TP E ML	ECAL	$\geq 1 \phi$ bin in θ_1 (0.75 GeV)
TP E MR	ECAL	$\geq 1 \phi$ bin in θ_6 (0.75 GeV)
TP E CL	ECAL	≥ 1 pair of collinear hits
TP E CAP	ECAL	endcap coincidence
TP E MMU	ECAL AND MU	≥ 1 correlated θ - ϕ bin
TP HAB	HCAL	$\geq 1 \theta$ - ϕ bin in barrel (1.0 GeV)
TP E MB	MU	$\geq 1 \theta$ - ϕ bin in barrel (0.3 GeV)
TP M UB	MU	$\geq 1 \theta$ - ϕ bin in barrel region
TP M U1	MU	$\geq 1 \phi$ bin in one θ bin
TP M U2	MU	≥ 2 independent ϕ bins in one θ bin
TP M UL	MU	$\geq 1 \phi$ bin in θ_1
TP M UR	MU	$\geq 1 \phi$ bin in θ_6
TP M UCL	MU	≥ 1 pair of coplanar hits
TP M UCAP	MU	endcap coincidence

Table 3.3: θ - ϕ matrix output signals which were utilized during data taking in 1997.

Chapter 4

Monte Carlo Event Simulation

General signal and background events have been processed through the full simulation of the OPAL detector [26]. The same event analysis chain has been applied to the simulated events as to the real data.

4.1 Outline of Monte Carlo Event Simulation

The general organisation of the OPAL simulation system is indicated by Figure 4.1. A "four-vector file" which contains four vectors of particles, their identification codes and history information generated by a certain event generator is processed in the detector simulation program GOPAL. This program is based on the CERN GEANT [27] simulation package, which provides a framework for the definition of the detector geometry, and controls the tracking of particles through this geometry. Inside GOPAL, the tracking of particles through the OPAL detector is performed and the detector response is simulated. In the lead glass calorimeter tracking of the particles in electro-magnetic showers is performed down to the threshold for emission of Čerenkov light (about 100 keV). In most of other regions standard tracking cutoffs (kinetic energy of 1 MeV for e^+/γ and 10 MeV for hadrons) are used, though lower cutoffs are employed in some of the sensitive volumes in the calorimeter and the muon chambers and in the thin silicon detectors. After the end of the tracking, the program enters the digitisation phase, which involves collecting the hit information and simulating the detector response by applying noise and a suitable normalisation. The digitisation code for each subdetector duplicates the banks provided by the data acquisition system and fills them with simulated raw data. The output from GOPAL is passed to the OPAL reconstruction program ROPE (Reconstruction of OPAL Events), which reconstructs the simulated events just as if they were real data.

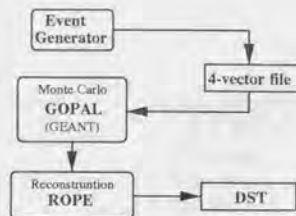


Figure 4.1: Outline of the organisation of the Monte Carlo program.

4.2 Simulation of Signals

4.2.1 $\tilde{\chi}_1^+ \tilde{\chi}_1^-$ Signals

The DFGT generator [28] is used to simulate signal events. It includes spin correlations and allows a proper treatment of the W boson width effect in the chargino decays. The generator includes initial state radiation and the JETSET 7.4 package [36] is used for the hadronisation of the quark-antiquark system in the hadronic decays of chargino. The decay of neutralino to $\gamma\tilde{G}$ is treated isotropically in the rest frame of the neutralino. The most important parameters which affect the chargino detection efficiencies are the mass of the lightest chargino, $m_{\tilde{\chi}_1^\pm}$, and the mass difference between the lightest chargino and the lightest neutralino, $\Delta M_+ \equiv m_{\tilde{\chi}_1^\pm} - m_{\tilde{\chi}_1^0}$. $\tilde{\chi}_1^+ \tilde{\chi}_1^-$ events have been generated for 72 points in the $(m_{\tilde{\chi}_1^\pm}, \Delta M_+)$ plane, for $m_{\tilde{\chi}_1^\pm}$ between 50 GeV and 90 GeV and for ΔM_+ between 3 GeV and $m_{\tilde{\chi}_1^\pm} - 100$ MeV. For each point 2000 events have been generated.

4.2.2 $\tilde{\chi}_2^0 \tilde{\chi}_1^0$ Signals

$\tilde{\chi}_2^0 \tilde{\chi}_1^0$ events have been generated for 75 points in the plane of $m_{\tilde{\chi}_2^0} + m_{\tilde{\chi}_1^0}$, $\Delta M_0 \equiv m_{\tilde{\chi}_2^0} - m_{\tilde{\chi}_1^0}$ using the DFGT generator and the JETSET 7.4 package for the hadronisation and the same treatment has been made for the decay of the lightest neutralino to $\gamma\tilde{G}$. At each point 1000 events have been generated.

4.3 Simulation of Background Events

The sources of background to the chargino and neutralino signals include multihadronic, four-fermion, lepton-pair and two-photon processes.

4.3.1 Multihadronic Processes

Multihadronic events are generated via the processes $e^+e^- \rightarrow Z^0/\gamma \rightarrow q\bar{q}$. At the center-of-mass energy above Z^0 pole, the process in which the initial state photons are radiated to reduce the effective center-of-mass energy to the Z^0 pole dominates the production of multihadronic events. This is called the ‘‘radiative-return’’ process and the cross-section at LEP2 energies reaches about 100 pb. Generation of these multihadronic events and hadronisation of the $q\bar{q}$ system is simulated using the PYTHIA and with the JETSET package [36].

4.3.2 Four-fermion Processes

Four-fermion events are dominated by W^+W^- pair production events. Other contributions are from $Z\gamma^*$ and $Z^{(*)}Z$ events. They are simulated using the gr4f generator [32] which takes into account all interfering four-fermion diagrams. The events with an energetic neutrino at the final state are important. They have large missing momenta which do not point at the beam direction. Therefore, events with large missing transverse momenta from the four-fermion processes can be misidentified as the signal, if an isolated photon is emitted from the initial or final states.

4.3.3 Lepton-pair Processes

Lepton pairs are simulated using the KORALZ generator [34] for $e^+e^- \rightarrow \mu^+\mu^-(\gamma)$ and $e^+e^- \rightarrow \tau^+\tau^-(\gamma)$ and the BHWIDE generator [35] for $e^+e^- \rightarrow e^+e^-(\gamma)$ events. Decay of τ leptons contains missing neutrinos, which causes the event to have large missing energy/momentum, especially in the case of radiative-return process, due to an initial state radiation they can have topologies very similar to that of the signal. Contribution from the other lepton-pair processes is negligible for this analysis.

4.3.4 Two-photon processes

Two-photon events are generated through the process $e^+e^- \rightarrow e^+e^- + X$ where the system X is produced in the scattering of two quasi-real photons as $\gamma\gamma \rightarrow X$. The Monte Carlo generators PHOJET [30] for $Q^2 < 4.5$ GeV² and HERWIG [31] for $Q^2 \geq 4.5$ GeV² are used for simulating hadronic two-photon events. The Vermaseren program [33] is used to simulate leptonic two-photon processes ($e^+e^- \rightarrow e^+e^-, e^+e^- \mu^+\mu^-,$ and $e^+e^- \tau^+\tau^-$). Additional samples of them which are not covered by the Vermaseren program are generated using gr4f.

The Monte Carlo samples used to estimate the number of background events in this analysis are summarised in Table 4.3.4.

Process	Generator	Cross section(pb)	Number of Events
$Z^0/\gamma \rightarrow q\bar{q}$	PYTHIA	107.4	500,000
Four-fermion	grc4f	19.0	94,968
$e^+e^-(\gamma)$	BHWIDE	627.9	423,859
$\mu^+\mu^-(\gamma)$	KORALZ	8.5	100,000
$\tau^+\tau^-(\gamma)$	KORALZ	8.4	100,000
$\gamma\gamma$ hadronic	PHOJET	14.1(nb)	999,000
	HERWIG	335.4	169,000
$\gamma\gamma$ leptonic	Vermaseren	1.8(nb)	1,830,000

Table 4.1: Background Monte Carlo samples used in this analysis.

Chapter 5

Analysis

The signal of gauge-mediated SUSY breaking for the case when $\tilde{\chi}_1^0$ is the NLSP and decays by $\tilde{\chi}_1^0 \rightarrow \gamma\tilde{G}$ is characterised as follows;

(Missing Momentum) Missing momentum carried by \tilde{G} 's should exist and it should not be in the beam direction where the acceptance of the detector is not covered well. This missing momentum causes large transverse momentum of the event.

(Acoplanarity Angle) Acoplanarity angle, which is explained in Section 5.3, is also expected to be large because of missing momentum carried by \tilde{G} 's.

(Missing Energy) Visible energy of the event should be smaller than the center-of-mass energy since unobserved \tilde{G} 's carry energy away.

(Isolated Photons) Photons from the decay of $\tilde{\chi}_1^0 \rightarrow \gamma\tilde{G}$ should have high energy and well isolated from the other charged tracks and neutral particles.

The analysis is performed on data collected during the 1997 runs of LEP at a center-of-mass energy of $\sqrt{s}=183$ GeV. Data used in this analysis are obtained in the runs in which all the subdetectors relevant to this analysis were fully operational, corresponding to an integrated luminosity of 56.75 pb^{-1} . Several cuts are applied on the collected data. These cuts are optimised to maximise the expected sensitivity of the signal. Efficiencies for the signals after applying these cuts are estimated using Monte Carlo events described in Chapter 4. Expected background at each stage of the analysis chain is also estimated in the same way. In this chapter, first of all, basic algorithms to calculate energy flow and to reconstruct jets employed in this analysis are presented in section 5.1 and 5.2. Then definition of acoplanarity angle is given in section 5.3 and the method to detect isolated photons is described in section 5.4. The analysis flows for chargino and neutralino detections are presented in section 5.6 and after.

5.1 Algorithm to Calculate Energy Flow

An algorithm to calculate energy flow is the most basic method to extract kinematic values of the events from measured values with each part of the detector. Measuring visible energy with better resolution leads to more precise measurement of missing energy which plays an important role in searches where unobserved new particles could carry off the energy.

In the hadronic final state, charged particles carry about 2/3 of the total energy. In the OPAL detector, in most cases, momenta of charged particles are measured with better momentum and angular resolutions by the tracking device (CT) than by the calorimeters (ECAL and HCAL).¹ Neutral particles carry the remaining 1/3 of the total energy and their energy needs to be measured by the calorimeters. However charged particles also deposit energy in ECAL and HCAL mainly due to hadronic interaction, though their momenta are measured by CT. This means that simply summing up all the measured momenta by CT and energies by ECAL and HCAL will result in doubly counting of energy for charged particles. This can be avoided by subtracting energy from the measured one by a part of the detector which has already been measured by the other part of the detector. Practically this is done by subtracting energy from ECAL and HCAL clusters by the amount of energy measured by the CT. The remained energy after subtraction should be treated as originated by neutral particles

When using calorimetry information, another problem can occur because the energy responses of ECAL and HCAL are very different for hadrons in the OPAL detector. Hadrons sometimes pass through ECAL without strong interaction and deposit full energy in HCAL. However we frequently have high energy deposition in ECAL not only by electrons or photons, but also by hadrons since the hadronic interaction length of ECAL is greater than one. When a hadron shower is produced inside ECAL by interaction of an incoming hadron with the material of ECAL, Čerenkov light of the amount which corresponds to energy of π^0 's in the shower is emitted. Other charged particles in the shower can lose part of their energy by the break up of nuclei and/or nuclear excitation followed by evaporation of nucleons, which is not observed in ECAL. This means that the energy measured by the ECAL is much smaller than the energy lost by the hadron in ECAL. Hence if we simply add the observed energy in ECAL and HCAL for hadrons, we don't have good resolution due to unobserved part of the hadron energy. The observed ECAL energy should be scaled up for hadrons. Although the fraction of the unobserved energy depends on the first interaction points of the hadrons which can not be evaluated cluster by cluster, it is possi-

¹The exception is for the high energy electrons. Energy measured by calorimeters has better resolution than that by the tracking devices.

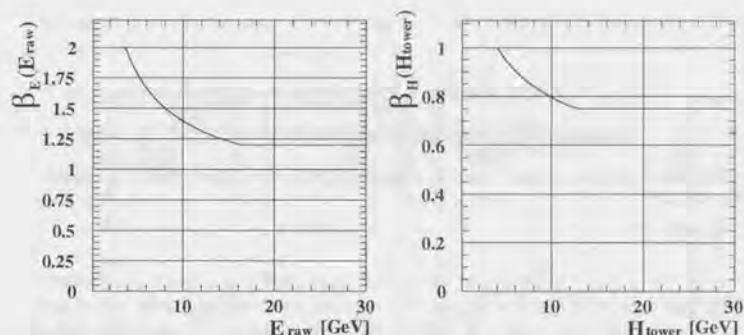


Figure 5.1: The correction factors for the ECAL cluster energy and the HCAL tower energy for the case of hadrons being incident particles to the calorimeters. The corrected energies are calculated as $\beta_E(E_{raw}) \cdot E_{raw}$ and $\beta_H(H_{tower}) \cdot H_{tower}$.

ble to estimate the mean fraction of the unobserved energy as a function of the observed cluster energy. Once we can correct the observed energy by adding the ECAL and HCAL energies with optimal weights, we can use calorimetry energy as better estimate of the hadron energy as well as tracking information. This procedure before subtraction of the energy measured with CT to avoid doubly counting is very important in order to achieve better resolution. The correction of the measured energy for hadrons is done using the functions shown in Figure 5.1 and visible energy is reconstructed by the following function.

$$E_{VIS} = \sum_i \beta_E(E_{raw}^i) \cdot E_{raw}^i + \sum_i \beta_H(H_{tower}^i) \cdot H_{tower}^i \quad (5.1)$$

Both $\beta_E(E^i)$ and $\beta_H(H^i)$ are tuned using the Monte Carlo samples for the case of pions to be incident particles to the calorimeters and checked with the data taken at Z^0 peak. Figure 5.2 shows cluster energy distributions of ECAL and HCAL for the data taken at Z^0 peak. In Figure 5.3, cluster energy distributions for the simulated chargino events with $m_{\tilde{\chi}_1^\pm} = 90$ GeV and $m_{\tilde{q}} = 45$ GeV are presented. In this figure, it can be seen that the distributions have similar shapes with those for the data at Z^0 and small energy clusters which have energy smaller than 10 GeV dominates the distributions. This means that the functions and parameters which have achieved good performance at Z^0 peak should be applicable in searches at higher energies.

This correction for hadrons is not expected to work correctly for isolated electrons and muons. In order to solve the problem, particle ID is employed in the algorithm. Details of particle ID is described in Appendix C.

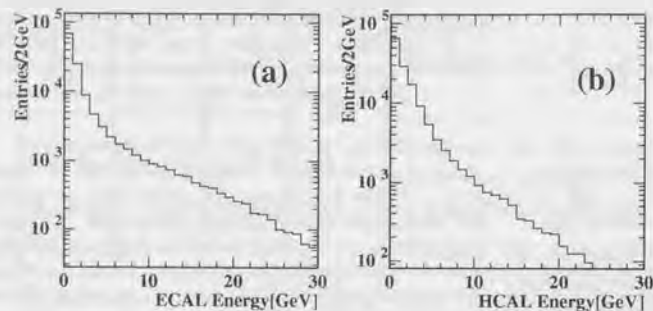


Figure 5.2: Cluster energy distributions of ECAL (shown in (a)) and HCAL (shown in (b)) for the data taken at Z^0 peak in 1997. Small clusters which have energy smaller than 10 GeV dominates the distributions.

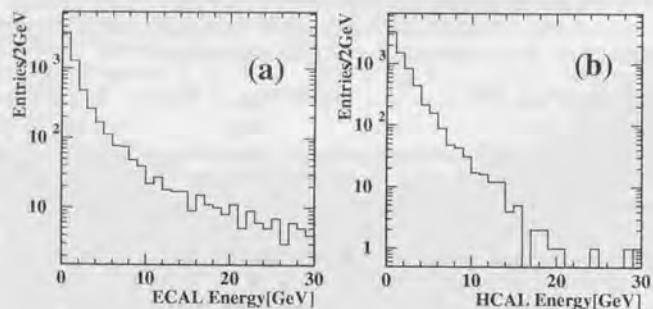


Figure 5.3: Cluster energy distributions of the simulated chargino events with $m_{\tilde{\chi}_1^+} = 90$ GeV and $m_{\tilde{\chi}_1^0} = 45$ GeV, (a) for ECAL and (b) for HCAL clusters. Clusters corresponding photons which come from $\tilde{\chi}_1^0$ decays are not included in (a). Same as the distribution shown in Figure 5.2, small clusters dominates the distributions.

Consequently in the algorithm to calculate the energy flow applied in this analysis, there are two important key items;

- subtraction of energy of calorimeters to prevent double counting
- correction of the measured energy by calorimeters for hadrons.

Based on these principles, the algorithm to calculate energy flow starts its process with finding ECAL and HCAL matching clusters to tracks, and matching tracks to ECAL and HCAL cluster, using extrapolated position of tracks into calorimeters.

Secondly the algorithm continues its process using particle ID. If the ECAL cluster is identified as that of an electron, the energy will not be scaled up in the following sequence. If a track is identified as that of a muon, the expected energy deposition for a minimum ionising particle is subtracted.

Next the algorithm starts searching for ECAL clusters associated with only one or two tracks in the matching region such as shown in Figure 5.4. If the ratio of ECAL cluster energy to the track momentum (or the sum of momenta of two tracks) is greater than 0.7, and the ratio of the associated HCAL cluster energy to the track momentum (or the sum) is less than 0.05, the ECAL energy is reduced by the associated track momentum without compensation. This situation will occur when γ is converted before reaching ECAL (as shown in Figure 5.4 (a)) or isolated pion interacts with lead-glass and larger energy than expected are observed by ECAL (as shown in Figure 5.4 (b)). For the latter case, the above requirement on the HCAL cluster energy is necessary to ensure for any other neutral particle not to have entered the cluster. In the case of γ -conversion, the cluster should be treated as an electro-magnetic shower cluster, and in the case of pion interaction the energy should not be calculated with calorimeter but with CT.

Then the algorithm starts energy correction for hadrons for each cluster except the ones which are identified as an isolated electron or muon, and γ -conversion or pion interaction and subtracts appropriate energy from ECAL and HCAL cluster according to the associated track momentum. Subtraction is done first from HCAL energy, and if HCAL energy can not fulfil the energy required by the track then from ECAL cluster energy. After subtraction, remaining energy on calorimeters should have come from neutral particles such as $\gamma(s)$ or neutral hadron(s). The remaining energy in ECAL is re-calculated as from γ for ECAL. After these processes, all the information is stored as that of tracks and energy deposition on the calorimeters by neutral particles. The schematic view of the algorithm is shown in Figure 5.5.

Performance of this algorithm is summarised in Table 5.1. Figure 5.6 shows the visible energy distribution both for Monte Carlo and for data at $\sqrt{s} = m_Z$ taken in 1997. In Figure 5.7 is shown comparison between data and Monte Carlo

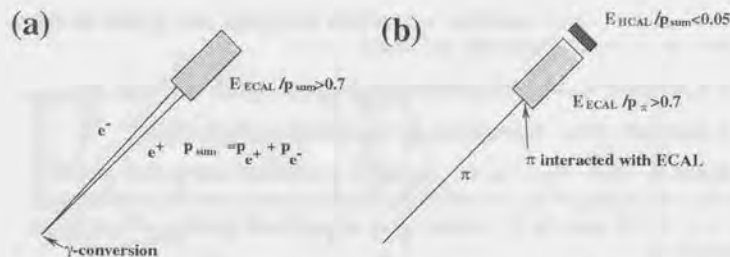


Figure 5.4: (a): an e^+e^- pair from γ -conversion which makes a single ECAL cluster. They are not identified as an isolated electron and a positron but the cluster should be treated as an electro-magnetic cluster. (b): When an isolated pion interacts with lead-glass and observed energy with ECAL is larger than 70% of the track momentum, scaling up the measured ECAL energy will change the event energy flow, which is dangerous especially for low-multiplicity analyses. Such pion energy should be measured by CT and the ECAL cluster should be discarded in the subtraction process. To ensure that no other neutral particle has entered the cluster, it is required that the HCAL measured energy should be smaller than 5% of the track momentum.

on the visible energy depending on the direction of the thrust axis. Figure 5.8 shows the transverse momentum distribution and Figure 5.9 shows difference of angular resolutions each in the plane perpendicular to the beam direction (ϕ) and parallel to the beam direction (θ) between Monte Carlo and data. Data and Monte Carlo agree very well in "without-HCAL mode", where the energy flow is calculated without using HCAL information to prevent apparent transverse momentum caused by noise and sampling fluctuations in HCAL, while their agreement is worse in "with-HCAL mode". The origin of this disagreement is not understood well. These differences are taken into consideration in the estimation of systematic error.

5.2 Jet Reconstruction Algorithm

Jets are formed from charged tracks and calorimeter clusters using the Durham algorithm [37]. The Durham jet reconstruction algorithm is one of successive combination algorithms which are iterative, beginning with a list of jets that are just the observed particles. At each stage of the iteration, one considers two jets i and j as candidates for combination into a single jet according to the value of a dimensionless variable y_{ij} which express "distance" between the jet i and j . The pair i, j with the smallest value of y_{ij} is combined first. When two jets are

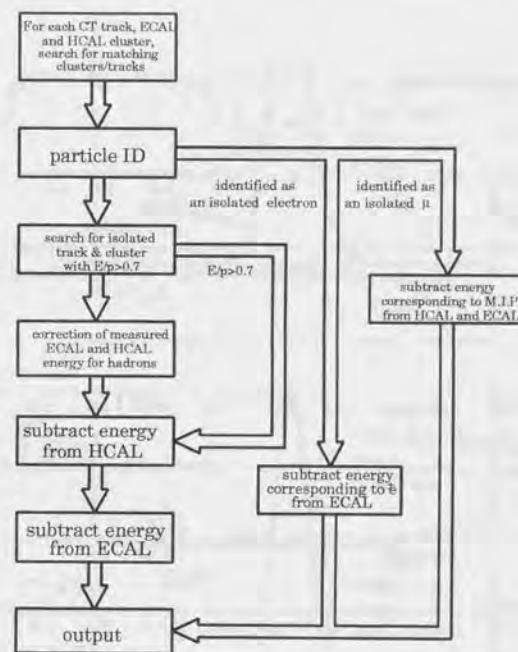


Figure 5.5: The schematic view of the algorithm to calculate energy flow.

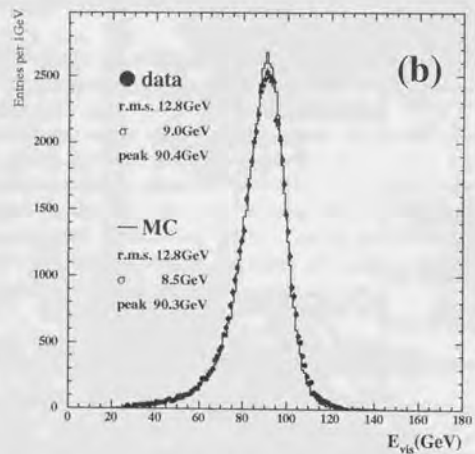
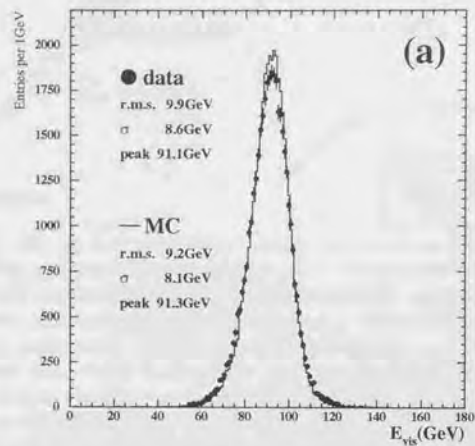


Figure 5.6: Visible energy distribution both for Monte Carlo and data at $\sqrt{s}=91.3$ GeV; (a) in the barrel region ($|\cos\theta_{\text{thrust}}| \leq 0.70$) and (b) in the full region. The tail at lower energies in (b) is due to the missing energy in the forward region.

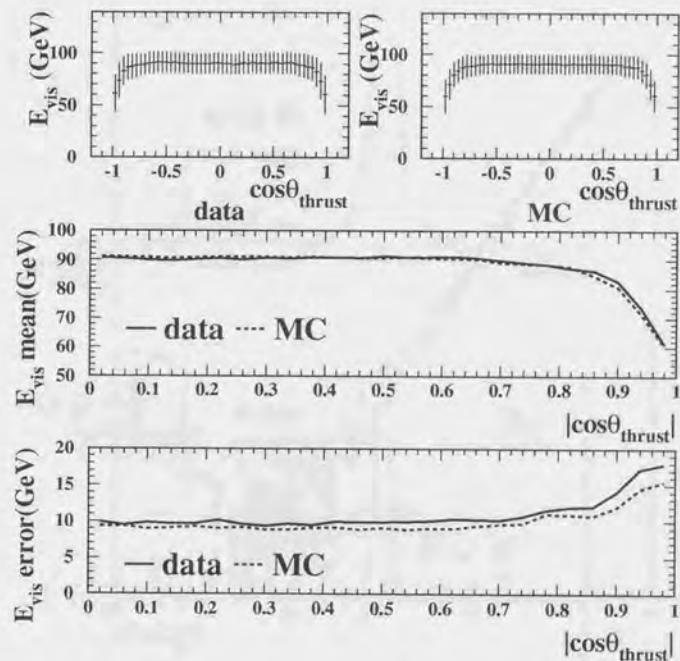


Figure 5.7: Comparison between data and Monte Carlo on the visible energy depending on the direction of the thrust axis.

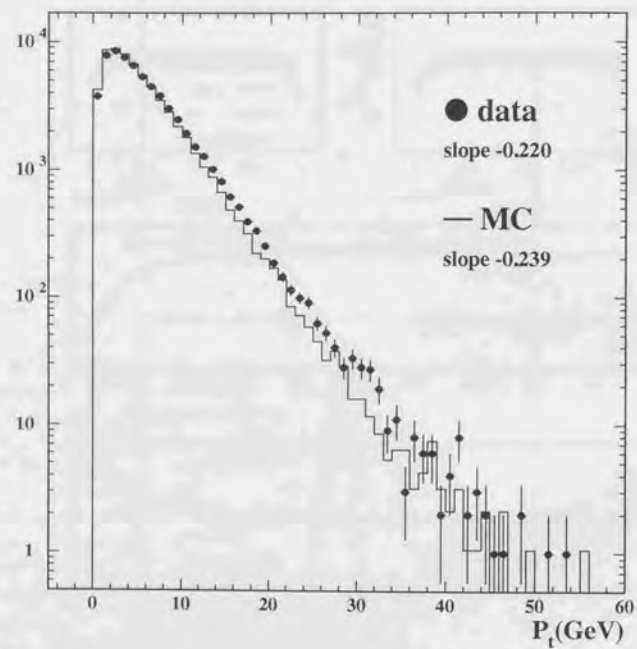


Figure 5.8: Transverse momentum distribution both for Monte Carlo and data at $\sqrt{s}=91.3$ GeV.

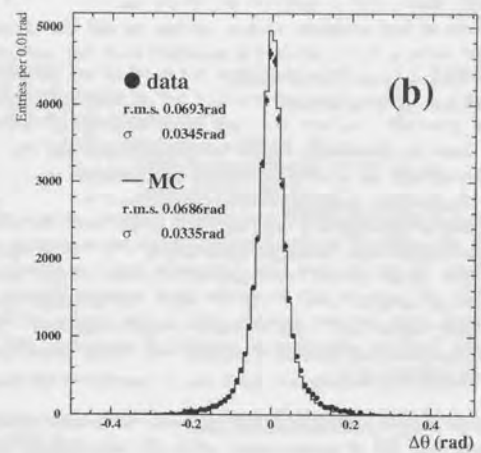
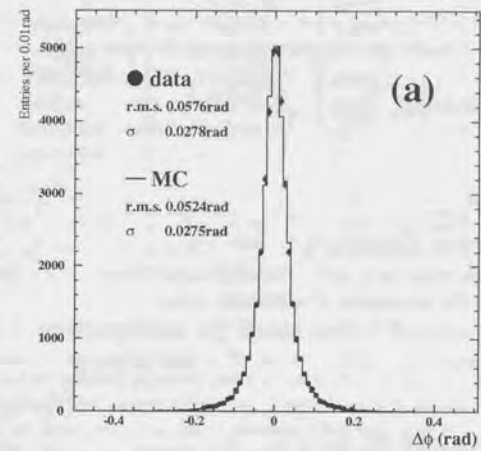


Figure 5.9: The distribution of the supplementary angle of ϕ_s (shown in (a)) and θ_s (shown in (b)) of 2 jets reconstructed using the Durham jet algorithm which is described in section 5.2.

		Monte Carlo	Data
Visible Energy	mean	90.80GeV	90.66GeV
	r.m.s.	9.2GeV	9.9GeV
	σ	8.1GeV	8.6GeV
	peak	91.3GeV	91.1GeV
Transverse Momentum	slope	-0.239	-0.220
Angular Resolution	$\Delta\phi$	0.0275rad	0.0278rad
	$\Delta\theta$	0.0335rad	0.0345rad

Table 5.1: Performance of the algorithm to calculate energy flow. These values are evaluated using data collected in Z^0 run in 1997 and Monte Carlo events generated with the OPAL configuration in 1997. Data and the results of Monte Carlo agree with each other very well. The differences between them are taken into consideration in the estimation of systematic error.

combined the four-momentum of the new jet P^u is determined by a combination formula

$$P^u = P_i^u + P_j^u \quad (5.2)$$

After this joining, there is a new list of jets. The process continues until every remaining y_{ij} is larger than a cutoff parameter, y_{cut} , which is called a jet resolution parameter. In this way, each event is classified as containing two, three, four, etc. jets, where the number of jets depends on y_{cut} . When events are forced to be reconstructed as N -jet events, this procedure is repeated until the number of jets reaches N without setting y_{cut} at a fixed value.

In the Durham algorithm, y_{ij} is defined as

$$y_{ij} = \frac{2\min(E_i^2, E_j^2)(1 - \cos\theta_{ij})}{s} \quad (5.3)$$

$2\min(E_i^2, E_j^2)(1 - \cos\theta_{ij})$ is the same as the transverse momentum squared of the lower-energy particle with respect to the direction of the higher-energy particle in the small-angle limit. It can be seen that a particle with low energy will be combined with another soft particle only when the angle between them is smaller than the angle it makes with another particle with higher energy. This is the superior feature of the Durham algorithm to the JADE algorithm [38]. In the JADE algorithm y_{ij} is defined to be

$$y_{ij} = \frac{2E_i \cdot E_j(1 - \cos\theta_{ij})}{s} \quad (5.4)$$

where two soft particle is easy to be combined even if the angle between them is large. In this analysis jet reconstruction is done with a jet resolution parameter of $y_{cut}=0.005$ if not specified otherwise.

5.3 Acoplanarity Angle

The acoplanarity angle, ϕ_{acop} , is defined as a supplementary angle in a plane perpendicular to the beam direction between two jets which are forced using the Durham jet algorithm,

$$\cos(\pi - \phi_{acop}) \equiv \frac{(\mathbf{p}_1 \times \hat{\mathbf{z}})(\mathbf{p}_2 \times \hat{\mathbf{z}})}{|\mathbf{p}_1 \times \hat{\mathbf{z}}||\mathbf{p}_2 \times \hat{\mathbf{z}}|} \quad (5.5)$$

where $\hat{\mathbf{z}}$ is the unit vector of e^- beam direction. If any missing particle with momentum not along the beam axis exists, the angle between the two jets in the transverse plane is not 180° . As a result large acoplanarity angle is expected for events including any missing particle(s).

5.4 Identification of Isolated Photons

Identification of isolated photons plays an important role in this analysis. It helps to reduce background events efficiently. Several conditions are required for ECAL clusters to be identified as isolated photons with high purity. There are two sets of conditions which are optimised separately for the high multiplicity analysis and the low multiplicity analysis which will be described in Section 5.7.

- There should not be any associated charged track to the ECAL cluster.
- The cluster has to be in the region of $|\cos\theta_{cluster}| \leq 0.90$. This requirement is needed because in the forward region ($|\cos\theta_{cluster}| > 0.90$) number of hit wires in CJ is so small that the tracking efficiency tends to decrease. It causes mis-identification of ECAL clusters originated from electrons as those from photons. In addition photons in the forward region is easy to generate electro-magnetic showers before reaching ECAL due to more material in that region. In this case it is difficult to identify the photons. Also the photons of initial-state radiation are concentrated in the forward region. This requirement is effective to reduce them. Figure 5.10 shows the angular distribution of the ECAL clusters without any associated charged track. The discrepancy between data and Monte Carlo in the forward region comes from lower efficiency of track reconstruction for data and the incomplete modelling of low mass two-photon processes.
- To reduce final-state radiation background, the cluster energy, $E_{cluster}$ should exceed 15 GeV and 5% of the beam energy in the high and low multiplicity analyses respectively. Figure 5.11 shows the energy distribution of isolated photons identified after requesting the other requirements for data and expected background, and signal Monte Carlo of typical mass combinations. The peak which can be seen around 70 GeV in Figure 5.11 (a) corresponds

ΔM_{\pm}	$m_{\tilde{\chi}_1^{\pm}}$	50	55	60	65	70	75	80	85	90
	GeV	GeV	GeV	GeV	GeV	GeV	GeV	GeV	GeV	GeV
3.0 GeV		95.2	96.6	96.4	97.2	97.0	97.3	96.8	97.6	96.9
5.0 GeV		94.4	95.3	95.5	96.8	96.8	97.2	97.1	96.9	97.3
10.0 GeV		93.8	94.6	96.2	97.0	96.6	96.6	96.5	96.7	96.3
20.0 GeV		93.1	94.3	95.3	95.7	96.5	96.4	96.7	96.3	96.1
$m_{\tilde{\chi}_1^{\pm}}/2$ GeV		92.0	93.9	94.1	95.1	95.2	95.1	95.3	95.7	95.6
$m_{\tilde{\chi}_1^{\pm}}-20$ GeV		88.5	90.2	90.7	92.7	91.9	92.2	91.5	90.9	91.1
$m_{\tilde{\chi}_1^{\pm}}-10$ GeV		86.1	87.3	87.3	87.4	87.6	87.0	87.0	85.2	80.7
$m_{\tilde{\chi}_1^{\pm}}$ GeV		81.4	82.0	82.7	82.2	82.0	80.2	74.8	62.9	62.1

Table 5.2: Photon detection efficiencies for each mass combination of $m_{\tilde{\chi}_1^{\pm}}$ and $\Delta M_{\pm} \equiv m_{\tilde{\chi}_1^{\pm}} - m_{\tilde{\chi}_1^0}$ listed in percent. Those are estimated at each mass combination grid using 2000 $\tilde{\chi}_1^0 \tilde{\chi}_1^{\pm}$ pair production simulated events, that is 4000 $\tilde{\chi}_1^0 \rightarrow \gamma \tilde{G}$ decays.

to the radiative-return events. The photon energy of the radiative-return event E_{gamma} is evaluated as

$$E_{\gamma} = \frac{(\sqrt{s})^2 - m_{\tilde{Z}}^2}{2\sqrt{s}}. \quad (5.6)$$

- The isolation conditions are required as energy deposition on cone energies, those are:

- sum of charged track momenta,
- sum of ECAL cluster energies excluding the primary cluster and
- sum of HCAL cluster energies

in 15° half-angle cone for high multiplicity analysis and 20° half cone for low multiplicity analysis. (a), (b) and (c) should be smaller than 1.0 GeV, 5.0 GeV and 5.0 GeV, respectively. In Figure 5.12 energy distributions of ECAL and HCAL clusters in 15° half-angle cone which satisfy the other requirements as an isolated photon are shown for data and expected background, and signal Monte Carlo.

Total efficiencies of identifying photons from $\tilde{\chi}_1^0 \rightarrow \gamma \tilde{G}$ range from 62% to 97% depending on the mass combination of $\tilde{\chi}_1^{\pm}$ and $\tilde{\chi}_1^0$ which decides the whole kinematics. They are summarised in Table 5.2

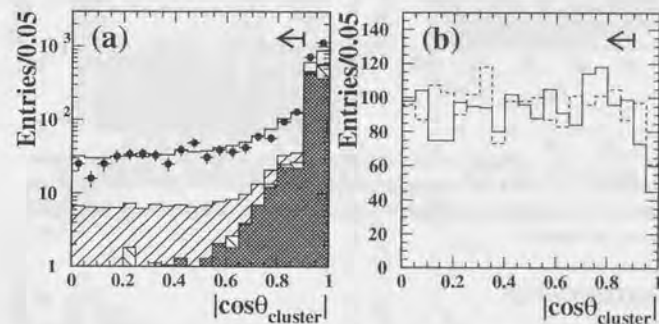


Figure 5.10: The angular distribution of the most energetic ECAL cluster which is not associated with any charged track and has cluster energy greater than 10 GeV. In (a) are shown the data (filled circles with error bars) and expected background: dilepton events (double hatched area), two-photon processes (negative slope hatching), four-fermion processes (positive slope hatching) and multihadronic events (open area). In (b) predictions from simulated chargino events are shown for $M_{\tilde{\chi}_1^{\pm}} = 90$ GeV and with $M_{\tilde{\chi}_1^0} = 87$ GeV (solid line) and with $M_{\tilde{\chi}_1^0} = 45$ GeV (dashed line), assuming 100% branching fractions for $\tilde{\chi}_1^{\pm} \rightarrow \tilde{\chi}_1^0 W^{\pm*}$ and for $\tilde{\chi}_1^0 \rightarrow \gamma \tilde{G}$. The normalisations of the signal distributions are arbitrary.

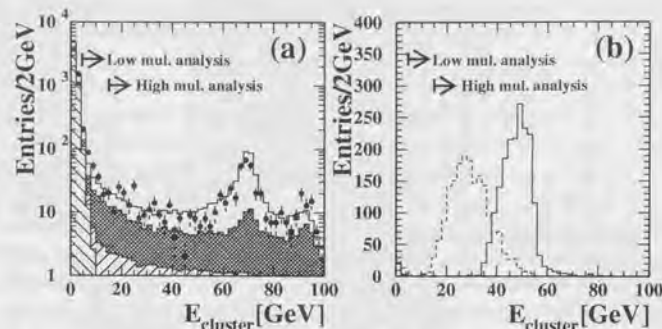


Figure 5.11: The ECAL cluster energy distribution for data and expected background are shown in (a) and for simulated signals are shown in (b). The symbols and shadings are the same as in Figure 5.10. The normalisations of the signal distribution are arbitrary.

5.5 Luminosity

The luminosity is measured using small-angle Bhabha events detected in the SW calorimeters. Bhabha scattering events are selected by requiring a high energy cluster in each end of SW, as described below. The energy in each calorimeter has to be at least half of the beam energy, and the average energy has to be at least three quarters of the beam energy. Figure 5.13 shows the correlation of the energy of the SW calorimeter on one end with that on the other end. The two highest energy clusters are required to be back-to-back in ϕ , $|\phi_R - \phi_L| - \pi| < 200$ mrad, where ϕ_R and ϕ_L are the azimuthal angles of the cluster in the right- and left-hand calorimeter respectively. They are also required to be collinear by placing a cut on the difference between the radial position, $\Delta R \equiv |R_R - R_L| < 25$ mm, where R_R and R_L are the radial coordinates of the clusters on a plane approximately 7 radiation lengths into the calorimeter. This cut corresponds to an acollinearity angle² of about 10.4 mrad. The inner and outer radial cuts on the fiducial region delimit a region between 38 and 52 mrad on one side of the calorimeter, which for the opposite calorimeter a wider zone between 34 and 56 mrad is used. Two luminosity measurements are performed; the narrower fiducial region on one side plus the wider region on the other side and vice versa. The final result is the

²The acollinearity angle is defined as a supplementary angle between the two electrons.

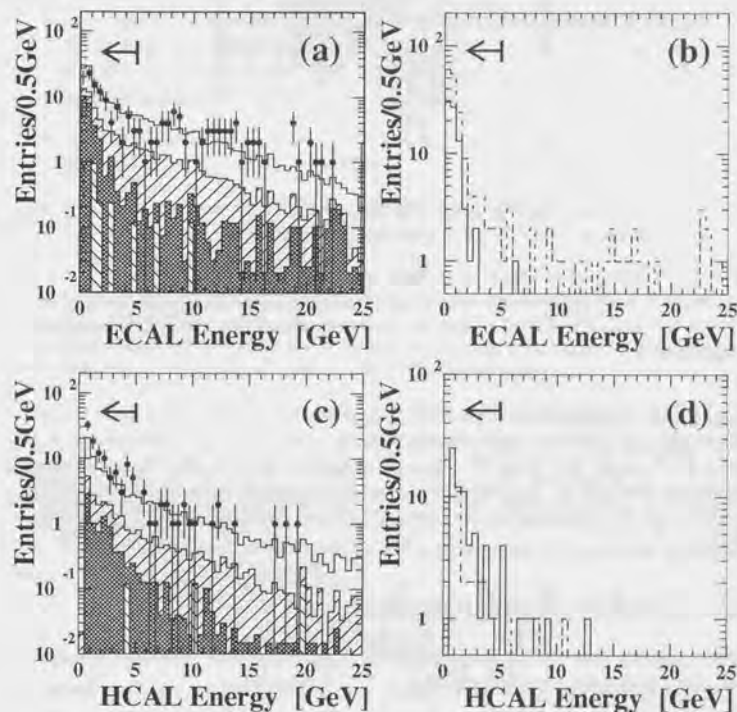


Figure 5.12: The cone energy distributions of ECAL and HCAL in 15° half-angle cone about the photon candidates of ECAL cluster for data and expected background are shown in (a) and (c) and for simulated signals are shown in (b) and (d). In (b) and (d) predictions from simulated signals are shown. The symbols and shadings are the same as in Figure 5.10. The arrows shown indicate the position of the cut used to identify isolated photons.

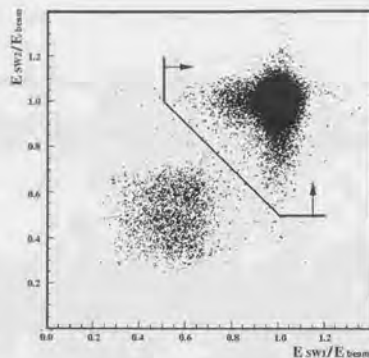


Figure 5.13: The correlation of the energy (shown as the fraction of the beam energy) of the SW calorimeter on one end of OPAL with that of the SW calorimeter on the other end. The Bhabha peak is clearly separated from the off-momentum background.

average of the two and has no first-order dependence on beam offsets or tilts. The cross-section for Bhabha scattering accepted by these cuts is calculated using the Monte Carlo program BHLUMI [39]. The statistical error on the luminosity measurement is 0.26%. The systematic uncertainty which arises from theoretical knowledge of the cross-section and detector effects amounts totally to 0.41% at 183 GeV.

5.6 Quality Requirements

Before applying the cuts, quality selection is done for each measured charged track and calorimeter cluster as follows,

- Good charged track is required to have at least 20 measured space points, more than 50% of the hits geometrically expected, and transverse momentum exceeding 100 MeV.
- ECAL clusters in the barrel region are required to have an energy of at least 100 MeV, and the clusters in the endcaps to have an energy of at least 250 MeV and contain at least two adjacent lead glass blocks.
- Clusters in HCAL are required to have an energy of at least 0.6 GeV in the barrel and endcaps, and at least 2 GeV in the pole tips.

Calculations of experimental variables are performed using the four-momenta evaluated by the algorithm described in section 5.1.

To select well measured events the following preselection criteria are applied:

- The number of charged tracks satisfying the quality criteria is required to be at least two. Furthermore, the ratio of the number of tracks satisfying the quality criteria to the total number of reconstructed tracks is required to be larger than 0.2.
- The transverse momentum of the event relative to the beam direction is required to be larger than 1.8 GeV.
- The total energies deposited in each side of the silicon tungsten calorimeter, forward calorimeter and the gamma-catcher have to be smaller than 2 GeV, 2 GeV and 5 GeV respectively.
- The visible invariant mass of the event has to exceed 3 GeV.
- The maximum EM cluster energy and the maximum charged track momentum have to be smaller than 130% of the beam energy.

After these preselection cuts 24816 data events are selected for further analysis. The number can be compared with 25003.4 which is expected from the background simulation. The difference between observed and expected events can be attributed to the incomplete modelling of low mass two-photon processes by the available generators. As it will be described later, reducing the two-photon contribution in the course of the analysis will give satisfactory agreement between data and the background simulation.

5.7 Detection of Charginos

The event samples are divided into two categories in order to optimise the sensitivity, motivated by the topologies expected to result from chargino events. Separate analyses are applied to each category to obtain optimal performance:

- (A) High multiplicity topologies, with $N_{ch} - N_{conv} > 4$, where N_{ch} is the total number of charged tracks in the event, and N_{conv} is the number of charged tracks originating from identified photon conversions,
- (B) Low multiplicity topologies, with $N_{ch} - N_{conv} \leq 4$.

Photon conversion is identified by the following methods. If a track has its partner such that their vertex geometry is consistent with photon conversion or if

a track has no corresponding hit on the central detectors (SI and CV), the energy of the associated ECAL cluster is greater than 1 GeV and the cluster is isolated from the other tracks under the condition of the sum of track momenta inside 20° half-angle cone smaller than 5 GeV, the track is identified as the one from photon conversion. The difference of efficiencies for photon conversion identification between data and Monte Carlo is estimated to be less than 5% relatively [40], which is evaluated using $\pi^0 \rightarrow \gamma\gamma$ samples in the region of the photon energy greater than 5 GeV. In the OPAL detector the number of radiation lengths traversed by photons emerging at 90 degree to the z axis is approximately 9% up to the end of the CJ sensitive volume. The total e^+e^- pair-production cross section, for photons with energies greater than ~ 1 GeV is given by $\sigma_{e^+e^-} \approx \frac{7}{9}(A/X_0 N_A)$, where A is the atomic weight of the material, N_A is Avogadro's number and X_0 is the number of radiation lengths [42]. Hence, the probability that a photon converts in the material is approximately 7%. Therefore the effect of the difference between efficiencies of conversion identification for data and Monte Carlo is smaller than 0.35%, which is negligible comparing with the other systematic errors that will be considered in Section 5.9.

The fraction of $\tilde{\chi}_1^+ \tilde{\chi}_1^-$ events falling into categories (A) and (B) for various mass combination of $(\Delta M_+ \equiv m_{\tilde{\chi}_1^+} - m_{\tilde{\chi}_1^0}, m_{\tilde{\chi}_1^+})$ are given in Table 5.3.

5.7.1 Analysis A ($N_{\text{ch}} - N_{\text{conv}} > 4$)

For reasonably large values of ΔM_+ , if either $\tilde{\chi}_1^+$ or $\tilde{\chi}_1^-$ decays hadronically, signal events tend to fall into category (A). As listed in Table 5.3, the fraction of $\tilde{\chi}_1^+ \tilde{\chi}_1^-$ events falling into category (A) is 72-90% if ΔM_+ is 10 GeV or greater. The fraction drops to $\leq 22\%$ for $\Delta M_+ = 3$ GeV since the average charged track multiplicity of these events is small. For an event to be considered as a candidate it has to satisfy the following criteria:

- (A1) The cosine of the polar angle of the missing momentum of the full event (including the hadron calorimeter) $\cos \theta_{\text{miss}}$ must satisfy $|\cos \theta_{\text{miss}}| < 0.95$. The $\cos \theta_{\text{miss}}$ distribution is given in Figure 5.15.
- (A2) The momentum of the full event transverse to the beam axis P_t^{HCAL} must satisfy $P_t^{\text{HCAL}} > 6$ GeV. Since the hadron calorimeter has noise and sampling fluctuations which can generate apparent transverse momentum, it is additionally required that the event transverse momentum without the hadron calorimeter satisfy $P_t > 5$ GeV. The distribution of P_t^{HCAL} is plotted in Figure 5.16.
- (A3) The visible energy of the full event must satisfy $E_{\text{vis}} < 0.9\sqrt{s}$.

	$m_{\tilde{\chi}_1^+}$	50	55	60	65	70	75	80	85	90
		GeV	GeV	GeV	GeV	GeV	GeV	GeV	GeV	GeV
ΔM_+	Category									
3.0 GeV	(A)	22	21	20	22	21	20	18	19	20
	(B)	78	79	80	78	79	80	82	81	80
5.0 GeV	(A)	48	48	47	48	47	47	47	46	47
	(B)	52	52	53	52	53	53	53	54	53
10.0 GeV	(A)	73	74	73	72	72	74	74	73	73
	(B)	27	26	27	28	28	26	26	27	27
20.0 GeV	(A)	85	83	85	84	85	85	84	85	84
	(B)	15	17	15	16	15	15	16	15	16
$m_{\tilde{\chi}_1^+}/2$	(A)	85	87	87	87	86	89	89	89	89
	(B)	15	13	13	13	14	11	11	11	11
$m_{\tilde{\chi}_1^+} - 20$ GeV	(A)	86	89	88	88	90	90	89	88	89
	(B)	14	11	12	12	10	10	11	12	11
$m_{\tilde{\chi}_1^+} - 10$ GeV	(A)	88	88	88	89	89	89	90	89	90
	(B)	12	12	12	11	11	11	10	11	10
$m_{\tilde{\chi}_1^+}$	(A)	88	88	88	88	88	90	90	90	88
	(B)	12	12	12	12	12	10	10	10	12

Table 5.3: The percentages of the simulated $\tilde{\chi}_1^+ \tilde{\chi}_1^-$ event samples falling into each of the two categories for $\tilde{\chi}_1^+ \rightarrow \tilde{\chi}_1^0 W^{*+}$ and $\tilde{\chi}_1^0 \rightarrow \gamma \tilde{G}$ decay, where $\Delta M_+ = m_{\tilde{\chi}_1^+} - m_{\tilde{\chi}_1^0}$. These percentages have been evaluated using 2000 events for each mass combination.

- (A4) After forcing the event to be reconstructed into two jets using the Durham algorithm, the acoplanarity angle between those jets must satisfy $\phi_{\text{acop}} > 12^\circ$. The distribution of ϕ_{acop} is plotted in Figure 5.17.
- (A5) The event must contain at least one isolated photon with the cluster energy of electromagnetic calorimeter greater than 15 GeV which did not originate from a conversion. The photon is required to be isolated by requirements on the maximum allowed energy inside a 15° half-angle cone centred on the cluster:
 - < 1 GeV charged track scalar momentum sum,
 - < 5 GeV energy sum in the electromagnetic calorimeter, after excluding the energy associated with the photon,
 - < 5 GeV energy sum in the hadron calorimeter.

The energy of the most energetic photon is plotted in Figure 5.18.

	data	total bkg.	q \bar{q} (γ)	$\ell^+\ell^-(\gamma)$	$\gamma\gamma\gamma$	4-f	$\tilde{\chi}_1^+\tilde{\chi}_1^-$	
$m_{\tilde{\chi}_1^+}$							90	90
$m_{\tilde{\chi}_1^0}$ (GeV)							87	45
cut								
no cuts	-	-	-	-	-	-	2000	2000
Presel+(A)	11275	10904.	3410.9	21.8	6770.1	715.4	368	1604
Cut (A1)	5403	5566.1	1306.6	13.6	3622.8	623.0	322	1455
Cut (A2)	1259	1342.4	799.0	11.8	16.1	515.6	319	1439
Cut (A3)	658	628.5	253.9	10.6	15.9	348.2	319	1434
Cut (A4)	304	295.3	22.1	1.1	6.2	266.0	312	1182
Cut (A5)	8	10.4	6.8	0.5	0.0	3.3	286	1063
Cut (A6)	2	2.6	0.6	0.1	0.0	1.9	264	960
Cut (A7)	2	2.1	0.6	0.1	0.0	1.4	264	892

Table 5.4: The remaining numbers of events after each cut for various background processes normalised to 56.75 pb^{-1} are compared with data for category (A). Numbers for two simulated event samples of $\tilde{\chi}_1^+\tilde{\chi}_1^-$ with $\tilde{\chi}_1^+ \rightarrow \tilde{\chi}_1^0 W^+$ are also given.

- (A6) Excluding the highest energy photon, the remainder of the event is split into two jets using the Durham algorithm. The sum of the opening angles among the two jets and the photon is required to be less than 358° , and the invariant mass of the two jet system is required to be less than 60 GeV. The distribution of the sum of opening angles is plotted in Figure 5.19
- (A7) Finally, if at least one lepton is identified, a veto is applied to remove $W^+W^- \rightarrow q\bar{q}\ell\nu$ events. After removing the most energetic lepton, the rest of the event is split into two jets using the Durham algorithm. The resulting di-jet invariant mass M_{jj} is required to be less than 60 GeV. It is also required that the invariant mass formed with the lepton and event missing momentum vector $M_{\ell\text{-miss}}$ is less than 60 GeV. In Figure 5.20 the distribution of the M_{jj} vs. $M_{\ell\text{-miss}}$ after cut (A6) is shown for background and for simulated chargino events with $m_{\tilde{\chi}_1^+}=90 \text{ GeV}$ and $m_{\tilde{\chi}_1^0}=45 \text{ GeV}$.

The numbers of events remaining after each cut are listed in Table 5.4. Two events survive the complete analysis. It can be compared with 2.1 expected from Standard Model sources. One of the candidates in analysis (A) is shown in Figure 5.14. For events falling into category (A) the efficiencies for $\tilde{\chi}_1^+\tilde{\chi}_1^-$ events are listed in Table 5.5 for the $\tilde{\chi}_1^0 W^{++}$ decay of the $\tilde{\chi}_1^+$ followed by the $\gamma \tilde{G}$ decay of the $\tilde{\chi}_1^0$ with zero lifetime. In large ΔM_+ region, energy of photons from the $\tilde{\chi}_1^0$ decays is liable to be below the cut threshold. In particular, for large $m_{\tilde{\chi}_1^+}$ the event shape is very similar to $W^+W^- \rightarrow q\bar{q}\ell\nu$ with a soft photon from the final

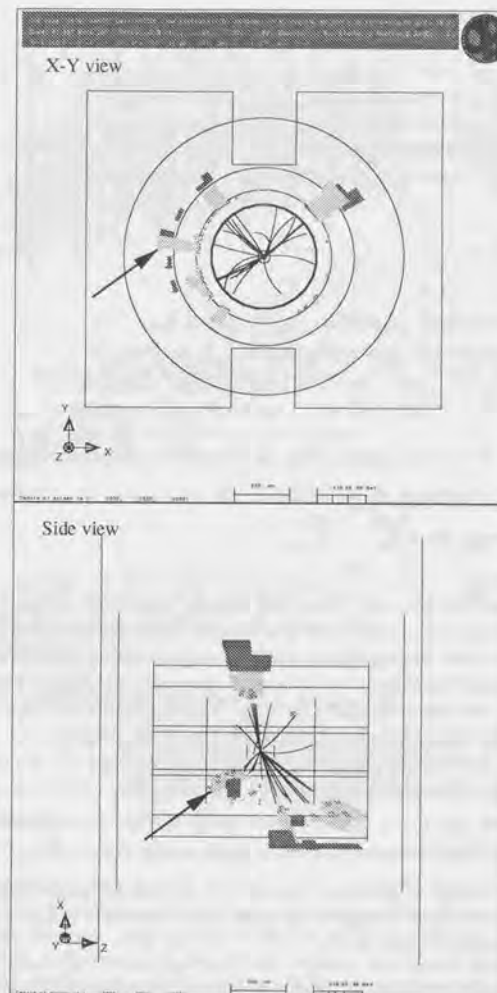


Figure 5.14: One of the candidates in analysis (A) shown in X-Y and side view. The ECAL cluster indicated by an arrow is identified as an isolated photon with the measured energy of 33.3 GeV. The event missing momentum is 50.3 GeV which directs to $\theta=1.84$ ($\cos \theta=-0.297$) and total measured energy is 132.9 GeV.

$m_{\tilde{\chi}_1^+}$ (GeV)	50	55	60	65	70	75	80	85	90
ΔM_+									
3.0 GeV	51	57	55	64	65	63	61	68	67
5.0 GeV	50	55	53	60	64	65	68	69	71
10.0 GeV	44	48	53	57	59	62	64	66	69
20.0 GeV	33	41	48	48	55	57	60	63	64
$m_{\tilde{\chi}_1^+}/2$	28	33	37	40	41	43	46	49	50
$m_{\tilde{\chi}_1^+} - 20$ GeV	21	23	25	26	28	28	27	25	24
$m_{\tilde{\chi}_1^+} - 10$ GeV	16	16	18	19	18	18	17	16	8
$m_{\tilde{\chi}_1^+}$	10	12	14	12	14	10	7	3	1

Table 5.5: The detection efficiencies requesting at least one isolated photon for events falling into category (A), in percent, for $\tilde{\chi}_1^+ \tilde{\chi}_1^-$ with two $\tilde{\chi}_1^+ \rightarrow \tilde{\chi}_1^0 W^{*+}$, $\tilde{\chi}_1^0 \rightarrow \gamma \tilde{G}$ decays normalised to the number of events with $N_{\text{ch}} - N_{\text{conv}} > 4$.

state radiation. This is the reason why the detection efficiencies drops in that region.

5.7.2 Analysis B ($N_{\text{ch}} - N_{\text{conv}} \leq 4$)

The low multiplicity analysis (B) selects the events with at least two charged tracks and at least one photon. There are initially significant number of backgrounds from leptonic two-photon collision events, which are largely removed by requiring that the event has significant visible energy and missing transverse momentum. After requiring at least one photon in the event, the largest background is from radiative tau pair production, $\tau^+ \tau^- \gamma$. This is reduced by requiring that the event be inconsistent with radiative return to the Z^0 with $Z^0 \rightarrow \tau^+ \tau^-$, and that the two tau leptons and the photon do not lie in a plane. To be selected as candidates, events must satisfy the following set of selection criteria:

- (B1) After forcing the event into two jets using the Durham algorithm, the acoplanarity angle between those jets must satisfy $\phi_{\text{acop}} > 5^\circ$.
- (B2) The visible energy of the event computed with charged tracks and electromagnetic calorimeter energy, E_{vis} , must satisfy $0.15\sqrt{s} < E_{\text{vis}} < 0.90\sqrt{s}$. E_{vis} is plotted in Figure 5.21.
- (B3) The cosine of the polar angle of the missing momentum of the event computed with charged tracks and electromagnetic calorimeter energy must satisfy $|\cos \theta_{\text{miss}}| < 0.95$.
- (B4) The event must contain at least one photon with an energy greater than 5% of the beam energy which did not originate from a conversion. The photon

	data	total bkg.	qq(γ)	$\ell^+ \ell^- (\gamma)$	$\tau^+ \tau^- \gamma$	4-f	$\tilde{\chi}_1^+ \tilde{\chi}_1^-$
$m_{\tilde{\chi}_1^\pm}$ (GeV)							90
$m_{\tilde{\chi}_1^0}$ (GeV)							87
cut							45
no cuts	-	-	-	-	-	-	2000
Presel.+(B)	13541	14099.4	13.6	6439.3	7456.3	190.3	1369
Cut (B1)	5771	6455.5	1.5	85.0	6256.5	112.6	1319
Cut (B2)	338	293.8	1.2	52.8	147.0	92.8	1319
Cut (B3)	157	150.2	0.2	41.2	26.2	82.7	1268
Cut (B4)	24	23.7	0.2	21.1	0.8	1.7	1208
Cut (B5)	4	4.9	0.0	3.6	0.3	1.2	1067

Table 5.6: The remaining numbers of events for data and for various background processes normalised to 56.75 pb^{-1} are compared after each cut in category (B). Numbers for two simulated event samples of $\tilde{\chi}_1^+ \tilde{\chi}_1^-$ with $\tilde{\chi}_1^+ \rightarrow \tilde{\chi}_1^0 W^*$ are also given.

is required to be isolated by requirements on the maximum allowed energy inside a 20° half-angle cone centred on the cluster:

- < 1 GeV charged track scalar momentum sum,
- < 5 GeV energy sum in the electromagnetic calorimeter, after excluding the energy associated with the photon,
- < 5 GeV energy sum in the hadron calorimeter.

(B5) Finally, several vetoes against $\tau^+ \tau^- \gamma$ are applied:

- The photon energy must be at least $3\sigma_\gamma$ different from the energy expected from radiative return to the Z^0 , where σ_γ is the estimated error on the photon energy. The energy of the most energetic photon is plotted in Figure 5.22.
- The cosine of the polar angle of the photon must satisfy $|\cos \theta_\gamma| < 0.90$.
- Removing the highest energy photon from the event, the rest of the event is inspected to see if it is consistent with a tau pair (either there are two identified leptons of any flavour, or if there is one identified lepton the remaining tracks are summed and considered as a tau jet if the resulting invariant mass is less than 2 GeV). If there is a possible $\tau^+ \tau^- \gamma$ event, the sum of the opening angles between the two tau jets and the photon must be less than 358° .
- If the event is consistent with $\tau^+ \tau^- \gamma$, the energies of the tau leptons are estimated by assuming that the angles of the tau leptons are the

same as those of the tau jets, using conservation of momentum and energy, allowing for up to one additional photon missing along the beam axis. The inferred di-lepton invariant mass must be at least 10 GeV different from the Z^0 boson mass.

The number of events remaining after each cut are listed in Table 5.6. Four events survive the complete analysis. The number can be compared with 4.9 expected from Standard Model sources. For events falling into category (B) the efficiencies for $\tilde{\chi}_1^+ \tilde{\chi}_1^-$ events are listed in Table 5.7 for $\tilde{\chi}_1^0 W^{*\pm}$ decay of the $\tilde{\chi}_1^\pm$ followed by the $\gamma \tilde{G}$ decay of the $\tilde{\chi}_1^0$ with zero lifetime.

$m_{\tilde{\chi}_1^\pm}$ (GeV)	50	55	60	65	70	75	80	85	90
ΔM_+									
3.0 GeV	46	45	47	49	48	52	56	64	66
5.0 GeV	47	47	47	52	51	55	57	62	68
10.0 GeV	44	49	55	51	53	60	63	67	64
20.0 GeV	48	51	51	57	55	58	63	67	64
$m_{\tilde{\chi}_1^\pm}/2$	50	55	53	53	57	63	63	60	63
$m_{\tilde{\chi}_1^\pm} - 20$ GeV	53	50	53	53	55	63	51	65	57
$m_{\tilde{\chi}_1^\pm} - 10$ GeV	46	49	52	55	51	56	59	62	54
$m_{\tilde{\chi}_1^\pm}$	46	54	46	55	49	52	56	37	53

Table 5.7: The detection efficiencies requesting at least one isolated photon for events falling into category (B), in percent, for $\tilde{\chi}_1^+ \tilde{\chi}_1^-$ with $\tilde{\chi}_1^\pm \rightarrow \tilde{\chi}_1^0 W^{*\pm}$, $\tilde{\chi}_1^0 \rightarrow \gamma \tilde{G}$ decays normalised to the number of events with $N_{\text{ch}} - N_{\text{conv}} \leq 4$.

5.7.3 Combined Efficiencies and Background for $\tilde{\chi}_1^+ \tilde{\chi}_1^-$

The high and low multiplicity analyses (A and B) are combined by adding the numbers of selected events and background expectation for the two analyses, and then linearly summing the selection efficiencies weighted by the fraction of events expected to fall into the two categories. The combined efficiencies of analysis (A) and (B) are given in Table 5.8.

5.7.4 Detection Efficiencies for Arbitrary Leptonic Branching Fraction of $\tilde{\chi}_1^\pm$ Decay

The branching fraction for $\tilde{\chi}_1^\pm \rightarrow \tilde{\chi}_1^0 \ell^\pm \nu$ may vary over a large range up to 100% when slepton(s) ($\tilde{\ell}$ and/or $\tilde{\nu}$) is lighter than chargino as discussed in Section 2.3.1. The selection efficiencies for chargino pair production in the case of a 100% branching fraction for $\tilde{\chi}_1^\pm \rightarrow \tilde{\chi}_1^0 \ell^\pm \nu$ followed by the prompt decays

$m_{\tilde{\chi}_1^\pm}$ (GeV)	50	55	60	65	70	75	80	85	90
ΔM_+									
3.0 GeV	46	48	49	50	52	55	59	63	67
5.0 GeV	48	50	52	54	57	60	63	66	69
10.0 GeV	44	48	52	55	59	61	64	66	68
20.0 GeV	36	41	46	51	55	58	60	63	64
$m_{\tilde{\chi}_1^\pm}/2$	32	39	38	41	44	46	48	50	51
$m_{\tilde{\chi}_1^\pm} - 20$ GeV	25	27	29	30	31	31	30	30	28
$m_{\tilde{\chi}_1^\pm} - 10$ GeV	19	21	22	23	23	22	20	18	14
$m_{\tilde{\chi}_1^\pm}$	15	21	17	17	16	14	12	9	5

Table 5.8: The combined detection efficiencies of the two categories in percent for $\tilde{\chi}_1^+ \tilde{\chi}_1^-$ with $\tilde{\chi}_1^\pm \rightarrow \tilde{\chi}_1^0 W^{*\pm}$ followed by the decay $\tilde{\chi}_1^0 \rightarrow \gamma \tilde{G}$.

$m_{\tilde{\chi}_1^\pm}$ (GeV)	50	55	60	65	70	75	80	85	90
ΔM_+									
3.0 GeV	43	43	44	46	49	53	57	62	68
5.0 GeV	44	43	43	44	46	49	53	59	65
10.0 GeV	48	50	52	54	55	57	59	60	62
20.0 GeV	46	50	53	56	59	61	63	65	67
$m_{\tilde{\chi}_1^\pm}/2$	53	54	55	57	58	60	62	63	65
$m_{\tilde{\chi}_1^\pm} - 20$ GeV	52	54	55	56	57	59	60	60	61
$m_{\tilde{\chi}_1^\pm} - 10$ GeV	46	50	52	54	56	57	57	57	56
$m_{\tilde{\chi}_1^\pm}$	48	50	51	52	52	51	50	48	46

Table 5.9: The combined detection efficiencies of the two categories in percent for $\tilde{\chi}_1^+ \tilde{\chi}_1^-$ with $\tilde{\chi}_1^\pm \rightarrow \tilde{\chi}_1^0 \ell^\pm \nu$ followed by the decay $\tilde{\chi}_1^0 \rightarrow \gamma \tilde{G}$.

$\tilde{\chi}_1^0 \rightarrow \gamma \tilde{G}$ are shown in Table 5.9. These efficiencies are estimated with the 100% $W^{(*)\pm}$ samples, using only $W^\pm \rightarrow \ell^\pm \nu$ decays.

For arbitrary leptonic branching fractions, $b = Br(\tilde{\chi}_1^\pm \rightarrow \ell^\pm \nu)$, detection efficiencies, $E(b)$, is estimated like the following. The events of signal Monte Carlo are divided into three cases utilising the information on $\tilde{\chi}_1^\pm$ decay:

1. Both of $\tilde{\chi}_1^\pm$ decay to leptons
2. One of $\tilde{\chi}_1^\pm$ decays to leptons and the other to hadrons
3. Both of $\tilde{\chi}_1^\pm$ decay to hadrons

Counting the efficiencies of analyses (A) $e_{A,i}$ and those of (B) $e_{B,i}$ separately for these three cases, and summing up those values with appropriate weights

linearly as indicated below, detection efficiencies for arbitrary branching fraction are obtained.

$$E(b) = \sum_{i=1}^3 \{R_i \times e_{A,i} + (1 - R_i) \times e_{B,i}\} \times Br_i(b) \quad (5.7)$$

where $Br_1(b) = b^2$, $Br_2(b) = 2b(1 - b)$, $Br_3(b) = (1 - b)^2$ and R_i is the fraction of events which falls into the category (A) each for three cases.

It was verified using two-body decay Monte Carlo ($\tilde{\chi}_1^\pm \rightarrow \tilde{\ell}^\pm \nu$ with $\tilde{\ell}^\pm \rightarrow \tilde{\chi}_1^0$ followed by $\tilde{\chi}_1^0 \rightarrow \gamma \tilde{G}$) that the efficiency for the two-body decays is higher than the efficiency for three-body decays if $m_{\tilde{\ell}^\pm} - m_{\tilde{\chi}_1^0} > 5$ GeV, so these efficiencies are generally somewhat conservative. The result of this comparison is shown in Table 5.10. The leptonic decay efficiencies are similar to the 100% $W^{(\pm)}$ case, although they are higher in the region with large ΔM_+ .

$\tilde{\chi}_1^\pm \rightarrow W^{(\pm)} \tilde{\chi}_1^0$ with $W^{(\pm)} \rightarrow \ell^\pm \nu$	$\tilde{\chi}_1^\pm \rightarrow \tilde{\ell}^\pm \nu$ with $\tilde{\ell}^\pm \rightarrow \tilde{\chi}_1^0$			
	$m(\tilde{\ell}^\pm) =$ 50 GeV	$m(\tilde{\ell}^\pm) =$ 55 GeV	$m(\tilde{\ell}^\pm) =$ 65 GeV	$m(\tilde{\ell}^\pm) =$ 75 GeV
65.0±1.5%	67.1±1.5%	68.3±1.5%	67.8±1.5%	65.6±1.5%

Table 5.10: Detection efficiencies for $\tilde{\chi}_1^\pm \tilde{\chi}_1^\pm$ with $\tilde{\chi}_1^\pm \rightarrow \ell^\pm \nu$ through $W^{(\pm)}$ and $\tilde{\ell}^\pm$ followed by the decay $\tilde{\chi}_1^0 \rightarrow \gamma \tilde{G}$, where $m(\tilde{\chi}_1^\pm) = 90$ GeV, $m(\tilde{\chi}_1^0) = 45$ GeV. Four cases are shown for decays through $\tilde{\ell}^\pm$; $m(\tilde{\ell}^\pm) = 50, 55, 65$ and 75 GeV.

5.7.5 Detection Efficiencies for Arbitrary $\tilde{\chi}_1^0$ Lifetimes

As shown in Section 2.2, decay length of $\tilde{\chi}_1^0 \rightarrow \gamma \tilde{G}$ ranges from $\sim 1 \mu\text{m}$ to the scale greater than the size of the detector. In this section we consider the detection efficiencies for the case of arbitrary $\tilde{\chi}_1^0$ lifetimes, which is of particular interest since the lifetime is, for all practical purpose, arbitrary, and a long-lived $\tilde{\chi}_1^0$ may have escaped the previous detection.

If one of the $\tilde{\chi}_1^0 \rightarrow \gamma \tilde{G}$ decays occurs outside the detector, its missing energy will effect all event quantities (visible energy, transverse momentum, etc.), and we must rely on our ability to find the single remaining photon. If both $\tilde{\chi}_1^0 \rightarrow \gamma \tilde{G}$ decays occur outside the detector volume, we rely on the gravity-mediated chargino/neutralino search performed by the OPAL collaboration [41].

The signal Monte Carlo simulation with a zero $\tilde{\chi}_1^0$ lifetime is utilised also for the non-zero lifetime case, using the information about the $\tilde{\chi}_1^0 \rightarrow \gamma \tilde{G}$ decays stored with the events. Assuming a given $\tilde{\chi}_1^0$ lifetime, τ , the reconstructed event information is modified according to following algorithm:

- The decay length at the $\tilde{\chi}_1^0$ rest frame (ct) of each $\tilde{\chi}_1^0$ is randomly determined using an exponential distribution with mean $c\tau$.
- The known momentum and mass of the $\tilde{\chi}_1^0$ are used to calculate its decay length, $\beta\gamma c\tau$.
- If the $\tilde{\chi}_1^0 \rightarrow \gamma \tilde{G}$ occurred outside the inner radius of the electromagnetic calorimeter, it is assumed that the γ is not observed, and the relevant event quantities are adjusted accordingly. If this photon was identified, it is removed from the event reconstruction.
- If the $\tilde{\chi}_1^0 \rightarrow \gamma \tilde{G}$ occurred inside the hadron calorimeter, it is conservatively assumed that the high multiplicity analysis has zero efficiency.

It has been verified with full Monte Carlo simulation using a subset of chargino masses ($m_{\tilde{\chi}_1^\pm} = 50, 60, 70, 80$ and 90 GeV) and a range of lifetimes ($c\tau = 1, 10, 100$ and 1000 metres) that the efficiencies estimated with the zero lifetime Monte Carlo are always underestimated ($\sim 5\%$). The conservatism arises principally by underestimating the detection efficiency for photons from $\tilde{\chi}_1^0 \rightarrow \gamma \tilde{G}$ inside the electromagnetic calorimeter. For longer lifetimes, we also consider the gravity-mediated chargino search, by conservatively assuming that it has zero efficiency if either $\tilde{\chi}_1^0$ decays inside the outer radius of the hadron calorimeter.

5.8 Detection of Neutralino

The high and low multiplicity analyses also have reasonable efficiency for the associated pair production process $\tilde{\chi}_2^0 \tilde{\chi}_1^0$, with $\tilde{\chi}_2^0 \rightarrow \tilde{\chi}_1^0 Z^{(*)}$ followed by the decays $\tilde{\chi}_1^0 \rightarrow \gamma \tilde{G}$. Using the same procedure for combining the two analyses as for the chargino limits, the combined efficiencies for $\tilde{\chi}_2^0 \tilde{\chi}_1^0$ production are listed in Table 5.11.

5.9 Systematic Errors and Corrections

Systematic errors on the number of expected signal events arise from the following sources: the measurement of the integrated luminosity (0.5%); Monte Carlo statistics for the signal samples, and interpolation errors when determining the efficiencies at arbitrary $m_{\tilde{\chi}_1^\pm}$ and ΔM_+ (typically 5%); modelling of the cut variables in the Monte Carlo simulations³ (5-10%), which is summarised in Table 5.9; gaugino field content of the $\tilde{\chi}^\pm$ and $\tilde{\chi}^0$ which can lead to different angular distributions for productions and decays ($< 5\%$). Since the analyses require at least

³This is estimated by comparing the efficiencies obtained by shifting each cut variable by its error. The error is determined by studying the differences between the data and the Monte Carlo in the samples with high statistics.

$m_{\tilde{\chi}_2^0} + m_{\tilde{\chi}_1^0}$ (GeV)	100	110	120	130	140	150	160	170	180
ΔM_0									
3.0 GeV	40	40	41	42	43	45	48	51	55
5.0 GeV	49	49	49	50	51	53	56	58	62
10.0 GeV	50	52	54	57	59	62	64	66	68
20.0 GeV	47	50	53	55	58	61	64	67	70
30.0 GeV	47	-	51	-	56	-	61	-	67
50.0 GeV	-	41	-	48	-	54	-	57	-
70.0 GeV	21	-	31	-	39	-	47	-	53
80.0 GeV	16	20	24	28	33	37	41	45	49
90.0 GeV	9	-	15	-	23	-	32	-	43
110.0 GeV		6	-	11	-	17	-	25	-
130.0 GeV				17	-	15	-	16	-
150.0 GeV						12	-	8	-
170.0 GeV								6	3

Table 5.11: The combined detection efficiencies of the two categories in percent for $\tilde{\chi}_2^0 \tilde{\chi}_1^0$ with $\tilde{\chi}_2^0 \rightarrow \tilde{\chi}_1^0 Z^*$ followed by the decay $\tilde{\chi}_1^0 \rightarrow \gamma G$.

one relatively energetic photon in the detector, the trigger inefficiency is expected to be negligible.

The systematic errors on the expected number of background events are determined from: Monte Carlo statistics in the simulated background events (typically 5%); modelling of the cut variables (10-20%), which is summarised in Table 5.9 for analysis (A) and (B). The rate of events in which random energy depositions in the forward detectors exceeds the veto thresholds used in the preselection is estimated from luminosity weighted random beam crossing events to be 4.5%. Since this effect is not included in the Monte Carlo simulations, the luminosity is reduced by this factor when deriving limits with the data.

	Analysis (A)	Analysis (B)
Acoplanarity Angle	3.4%	0.50%
Visible Energy	3.8%	negligible
Photon Energy	6.1%	2.0%
Photon Isolation	8.9%	2.0%
Total	12%	3.0%

Table 5.12: The systematic errors on the number of expected signal events which arise from modelling of the cut variables.

	Analysis (A)	Analysis (B)
Acoplanarity Angle	2.3%	8.0%
Visible Energy	4.6%	0.5%
Photon Energy	8.8%	8.0%
Photon Isolation	21%	4.0%
Total	24%	12%

Table 5.13: The systematic errors on the expected number of background events caused by modelling of the cut variables.

OPAL Preliminary

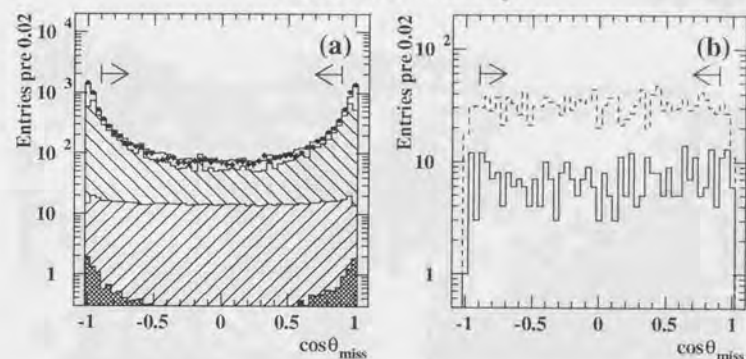


Figure 5.15: The distribution of the event missing direction for events in category (A) after preselection. In (a) are shown the data and the prediction from different background processes. The symbols and shadings are the same as in Figure 5.10.

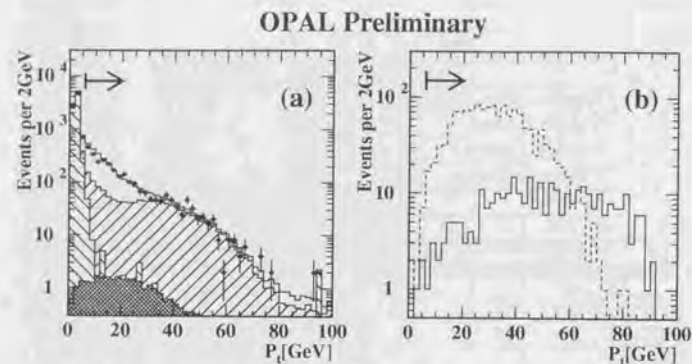


Figure 5.16: The distributions of the event transverse momentum, P_t , for events in category (A) after cut (A1). In (a) are shown the data and the prediction from different background processes. The symbols and shadings are the same as in Figure 5.10.

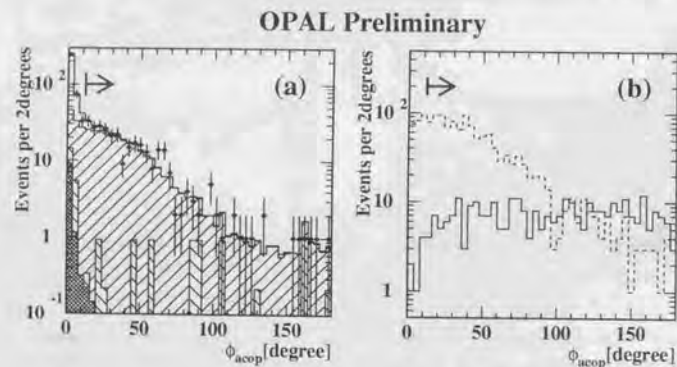


Figure 5.17: The distributions of the event acoplanarity angle, ϕ_{acop} , for events in category (A) after cut (A3). The symbols and shadings are the same as in Figure 5.10.

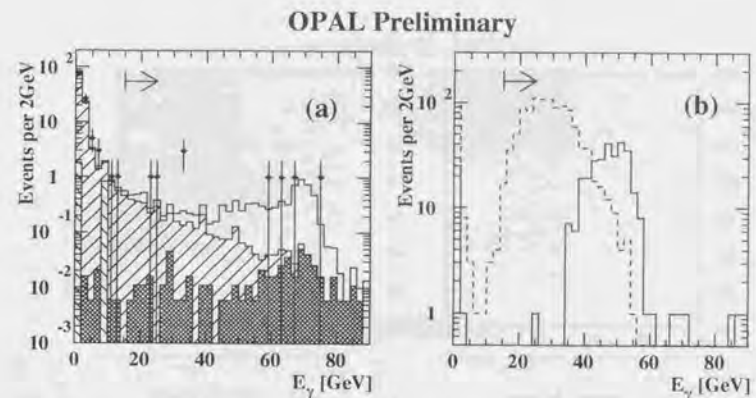


Figure 5.18: The distributions of the energy of the most energetic photon, E_γ , for events in category (A) after cut (A4). The symbols and shadings are the same as in Figure 5.10.

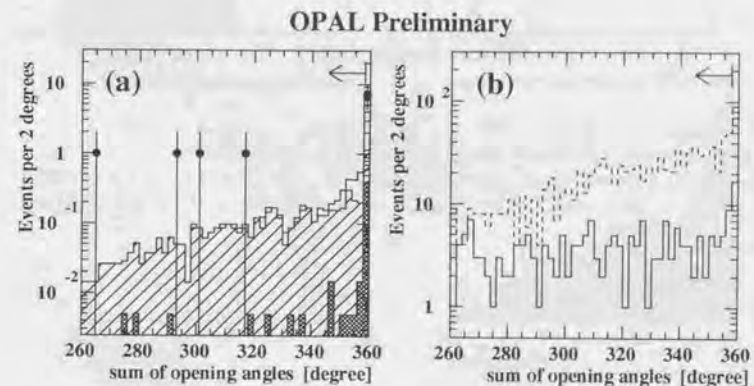


Figure 5.19: The distribution of the sum of the opening angles among the two jets and the photon, for events in category (A) after cut (A5). The symbols and shadings are the same as in Figure 5.10.

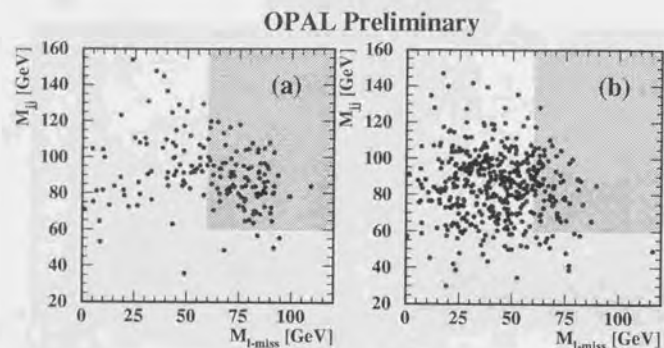


Figure 5.20: The distributions of the M_{jj} vs. M_{l-miss} for events in category (A) after cut (A6), (a) for background and (b) for simulated chargino events with $M_{\tilde{\chi}^{\pm}} = 90$ GeV and $M_{\tilde{\chi}^0} = 45$ GeV. Events in the shaded region are rejected with this cut.

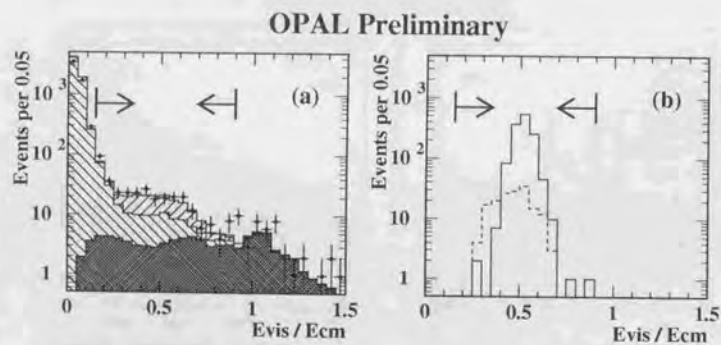


Figure 5.21: The distributions of the visible energy, E_{vis} , divided by the centre-of-mass energy, E_{cm} , in category (B), after cut (B2). The symbols and shadings are the same as in Figure 5.16.

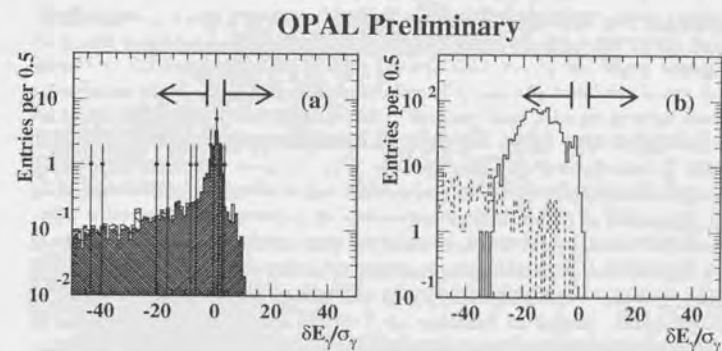


Figure 5.22: The distributions of the photon energy minus that expected from radiative return to the Z^0 , δE_{γ} , divided by its error, σ_{γ} , in category (B), after cut (B5). The symbols and shadings are the same as in Figure 5.16.

Chapter 6

Results

Since no excess over the expectation from Standard Model sources is observed, the limits on the production cross sections of charginos and neutralinos are established.

6.1 Limits on the Production Cross Sections

Interpolating the detection efficiencies in Table 5.8 to obtain the efficiency at arbitrary $(m_{\tilde{\chi}_1^\pm}, \Delta M_4)$ and considering the total of 6 events observed with 7.0 expected from background sources, production cross section limit contours are shown in Figure 6.1. The final limits are computed using the PDG method [42]. Systematic errors are incorporated using the method which is suggested in Reference [43].

Limits on the production cross section for $\tilde{\chi}_2^0 \tilde{\chi}_1^0$ in the case of a 100% branching fraction for $\tilde{\chi}_2^0 \rightarrow \tilde{\chi}_1^0 Z^{(*)}$ followed by the prompt decays $\tilde{\chi}_1^0 \rightarrow \gamma \tilde{G}$ are also shown in Figure 6.2. The region $m_{\tilde{\chi}_2^0} + m_{\tilde{\chi}_1^0} < m_Z$ is not considered in this analysis because the sensitivity was expected to be higher at $\sqrt{s} \simeq m_{Z^0}$ [44].

Based on the obtained efficiencies with the method described in Section 5.7.4, limits on model independent cross sections can also given on the chargino pair production with arbitrary leptonic branching fractions in their decays. Some example limits on the chargino pair production cross section *vs.* the branching fraction for $\tilde{\chi}_1^\pm \rightarrow \tilde{\chi}_1^0 \ell^\pm \nu$ are shown in Figure 6.3 for $m_{\tilde{\chi}_1^\pm} = 90$ GeV. In that figure, the shaded region indicates leptonic branching fractions smaller than 100% $W^{(*)\pm}$ decays, which would not occur in the framework of the GMSB model since the squarks are expected to be heavy.

For arbitrary $\tilde{\chi}_1^0$ lifetimes, the production cross section limit is obtained with the efficiencies estimated using the method shown in Section 5.7.5. In Figure 6.4, limits on the chargino pair production cross section for three example ΔM_4 with $m_{\tilde{\chi}_1^\pm} = 90$ GeV are shown. At large $c\tau$ in this figure the limits from the gravity-mediated chargino search [41] are included, and thus all $0 < c\tau < \infty$ is covered.

Limits at large $c\tau$ are obtained by scaling up the limit in the gravity-mediated chargino search with the fraction of events in which both of neutralinos decay outside the detector volume for given $c\tau$. The fractions are estimated using the signal Monte Carlo of zero lifetime with the method described in Section 5.7.5.

Using the same method, in Figure 6.5 limits on the $\tilde{\chi}_2^0 \tilde{\chi}_1^0$ production cross section for arbitrary $\tilde{\chi}_1^0$ lifetimes are given for the cases of $(m_{\tilde{\chi}_2^0}, m_{\tilde{\chi}_1^0}) = (95 \text{ GeV}, 85 \text{ GeV})$, $(135 \text{ GeV}, 45 \text{ GeV})$ and $(160 \text{ GeV}, 10 \text{ GeV})$.

6.2 Limits in the M_2 *vs.* μ Plane

Results of the limits on the chargino production cross section are transformed back into the M_2 *vs.* μ plane, where M_2 is the $SU(2)$ gaugino mass and μ is the Higgs superpotential mixing parameter. Although from given input parameters at messenger scale GMSB models can compute M_2 at the electroweak scale by using the RG equations, and μ from the relations among the Higgs sector mass parameters obtained by imposing electroweak symmetry breaking, it can be useful to set the limits in the plane which is familiar from existing gravity mediated SUSY interpretations [45]. Excluded region in the M_2 *vs.* μ plane at 95% confidence level concluded from the $\tilde{\chi}_1^\pm \tilde{\chi}_1^\mp$ search results for four selected $\tilde{\chi}_1^0$ lifetimes are shown in Figure 6.6 for $\tan \beta = 2$ and in Figure 6.7 for $\tan \beta = 35$. Since the 100% $W^{(*)\pm}$ decay efficiencies are always less than or equal to those with higher leptonic branching fractions, they are conservatively used for the limit calculation. The $\tilde{\chi}_1^\pm \tilde{\chi}_1^\mp$ production cross section is determined by its field content and by the mass of the $\tilde{\nu}_e$, which contributes to the production via t-channel exchange. In this calculation the mass of the $\tilde{\nu}_e$ is evaluated as follows. From Equations (2.4) and (2.5), M_2 and $m_{\tilde{\nu}_e}$ can be written at the messenger scale as

$$M_2 = N \frac{\alpha_2}{4\pi} \Lambda \quad (6.1)$$

$$m_{\tilde{\nu}_e}^2 = 2\Lambda^2 N \left[\frac{3}{4} \left(\frac{\alpha_2}{4\pi} \right)^2 + \frac{3}{5} \left(\frac{Y}{2} \right)^2 \left(\frac{\alpha_1}{4\pi} \right)^2 \right] \quad (6.2)$$

Neglecting evolution of $m_{\tilde{\nu}_e}^2$ from the messenger scale the electroweak scale and assuming the number of messengers equal to one, $m_{\tilde{\nu}_e}$ can be evaluated from given M_2 .

6.3 Limits in the Minimal GMSB Model Parameter Space

Results of the limits on chargino production cross section are transformed also into the minimal gauge-mediated SUSY breaking parameters described in Section 2.1:

$$(N=1, \tan \beta, \Lambda, \text{sign}(\mu), M)$$

where N is the number of messengers, $\tan \beta$ is the ratio of vacuum expectation values of Higgs bosons, Λ is a parameter to set the overall scale for the superpartner spectrum and M is the scale of the messenger(s). In the minimal model, giving those values sets the boundary conditions at the messenger scale and the masses of sparticles at electroweak scale are calculated according to the RG equations. Although the parameter μ is not determined by the underlying theory, it can be computed from the condition of correct electroweak breaking [5] as shown in Section 2.1. Since the mass of $\tilde{\nu}_e$ can be also computed together with the field content of a chargino from input parameters with RG evolution, the production cross section of chargino pair is obtained at arbitrary point in the parameter space.

In Figure 6.8, the excluded region in the Λ vs. M plane at 95% confidence level is shown for the case of $\tan \beta = 2$ and $c\tau(\tilde{\chi}_1^0 \rightarrow \gamma\tilde{G}) = 0$ with $\text{sign}(\mu) > 0$, $N=1$ and $m_{\text{top}}=175$ GeV. Inside the scanned parameter space $\tilde{\chi}_1^0$ is always the NLSP and all of the final states of $\tilde{\chi}_1^+ \tilde{\chi}_1^-$ production are covered by this analysis even when the $\tilde{\ell}$ is lighter than $\tilde{\chi}_1^\pm$ and the leptonic branching fraction of $\tilde{\chi}_1^\pm$ is equal to 100% due to the conservative estimation of the detection efficiencies using the 100% $W^{(*)\pm}$ decay sample of $\tilde{\chi}_1^\pm$.

Figure 6.9 shows the excluded region in the $\tan \beta$ vs. Λ plane for the case of $M=100$ TeV and $c\tau(\tilde{\chi}_1^0 \rightarrow \gamma\tilde{G}) = 0$, $\text{sign}(\mu) > 0$, $N=1$ and $m_{\text{top}}=175$ GeV. The dashed line indicates the kinematic limit for the chargino pair production. Contours of constant slepton masses are also shown.

The stau mass eigenstates $(\tilde{\tau}_1, \tilde{\tau}_2)$ have a different feature from those of the other sleptons. The stau mass matrix is given by [5]

$$m_{\tilde{\tau}}^2 = \begin{pmatrix} m_{\tilde{\tau}_L}^2 + m_\tau^2 - (\frac{1}{2} - \sin^2 \theta_W) \cos 2\beta M_Z^2 & m_\tau (A_\tau - \mu \tan \beta) \\ m_\tau (A_\tau - \mu \tan \beta) & m_{\tilde{\tau}_R}^2 + m_\tau^2 - (\frac{1}{2} - \sin^2 \theta_W) \cos 2\beta M_Z^2 \end{pmatrix} \quad (6.3)$$

where A_τ is tri-linear A term for the $\tilde{\tau}$.

Due to the large mixing effect between the left and right handed $\tilde{\tau}$ for large $\tan \beta$ caused by the off-diagonal terms proportional to m_τ , the lighter mass eigenstate of $\tilde{\tau}$ ($\tilde{\tau}_1$) can be lighter than the $\tilde{\chi}_1^0$. In particular, for extremely large values of $\tan \beta$, the $\tilde{\tau}$ mass-squared becomes negative which is shown as a hatched region in Figure 6.9. For the region where $\tilde{\tau}$ is the NLSP the final state of $\tilde{\chi}_1^+ \tilde{\chi}_1^-$ production is $\tau\tau + X + (\text{missing energy})$ and that region can not be excluded by this analysis, though some area should have been already excluded by the acoplanar di-lepton search [20].

In the region where the $\tilde{\chi}_1^0$ is the NLSP, slepton mass can be lighter than the lightest chargino and kinematically accessible region for slepton pair production extends to larger M than for chargino pair production. In such region, slepton pair production results in the final state of $\ell\ell\gamma\gamma + X + (\text{missing energy})$ through

$\tilde{\ell} \rightarrow \ell\tilde{\chi}_1^0$ followed by the decay of $\tilde{\chi}_1^0 \rightarrow \gamma\tilde{G}$. Since this final state is similar to the event of chargino production with 100% leptonic decay branching fraction, it is expected that the low multiplicity analysis described in Section 5.7.2 has significant detection efficiencies.

In any case when the signal is established, it is important to study the decay length of the NLSP ($\tilde{\chi}_1^0$) by which the SUSY breaking scale (\sqrt{F}) can be evaluated with Equation (2.14). Although it is impossible to find the decay point inside the detector³, the decay length could be evaluated roughly by counting the fraction of the events which contains two, one and zero isolated photons. Figure 6.10 shows how the fraction changes depending on the decay length of the $\tilde{\chi}_1^0$ for the case of chargino pair production with typical mass combination of $m_{\tilde{\chi}_1^+}=90$ GeV and $m_{\tilde{\chi}_1^0}=45$ GeV. In the shaded region ($c\tau \simeq 2-100$ m), some events contain only one isolated photon and others contain two isolated photons though events without any isolated photons can not be detected by this analysis but could be detected by the gravity-mediated chargino search. This information can be transferred to the allowed region of $\sqrt{F} \simeq 4 \times 10^5 - 10^6$ GeV using Equation (2.14). In shorter decay length region, events with two isolated photons could be always detected by this analysis except ones escaping the detection due to inefficiency and the upper limit of \sqrt{F} could be obtained. However this situation means that the coupling of the \tilde{G} with particles is so strong that the signal such as $e^+e^- \rightarrow \tilde{G}\tilde{G}\gamma$ is expected to be observed [46]. The excess of the cross section of the event than the Standard Model background such as $e^+e^- \rightarrow \nu\nu\gamma$ is able to limit the allowed region of \sqrt{F} . In longer decay length region, the signal can not be detected by this analysis at all but the gravity-mediated chargino search could detect the signal. In this case lower limit of \sqrt{F} would be obtained. Recently it has been proposed as a future project in the CERN LHC to detect a slow decay of the $\tilde{\chi}_1^0$ by constructing a dedicated experiment with a thick iron shield around the collision point followed by a long decay tunnel with detectors which can measure the photon direction at the end [47].

³For the case of slepton NLSP, the decay point can be found at the kink position in the tracking detector. The distribution of the length between that position and the vertex can be translated to the decay length.

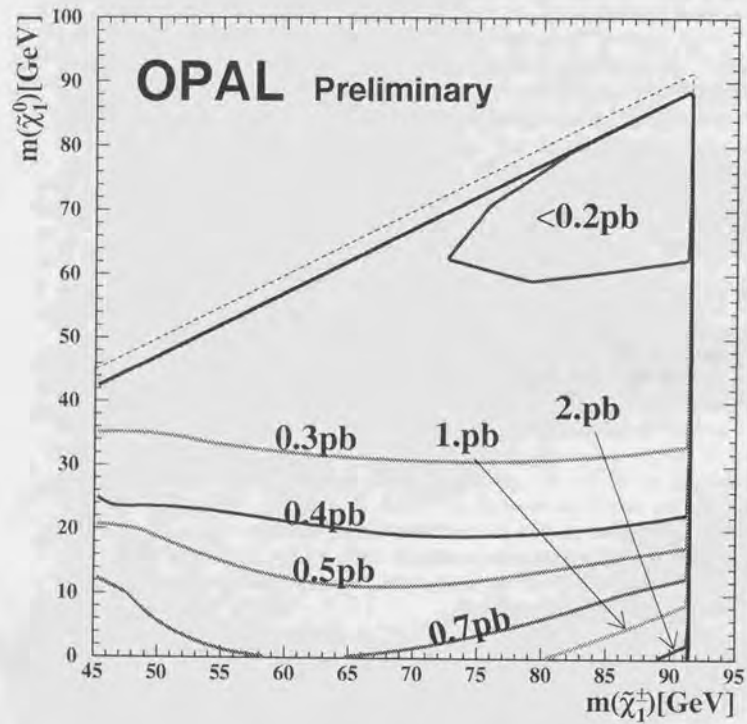


Figure 6.1: Upper limits on the $\tilde{\chi}_1^+ \tilde{\chi}_1^-$ production cross section at 95% C.L., assuming both decay via $\tilde{\chi}_1^\pm \rightarrow \tilde{\chi}_1^0 W^{(\pm)\pm}$, followed by prompt $\tilde{\chi}_1^0 \rightarrow \gamma \tilde{G}$ decays.

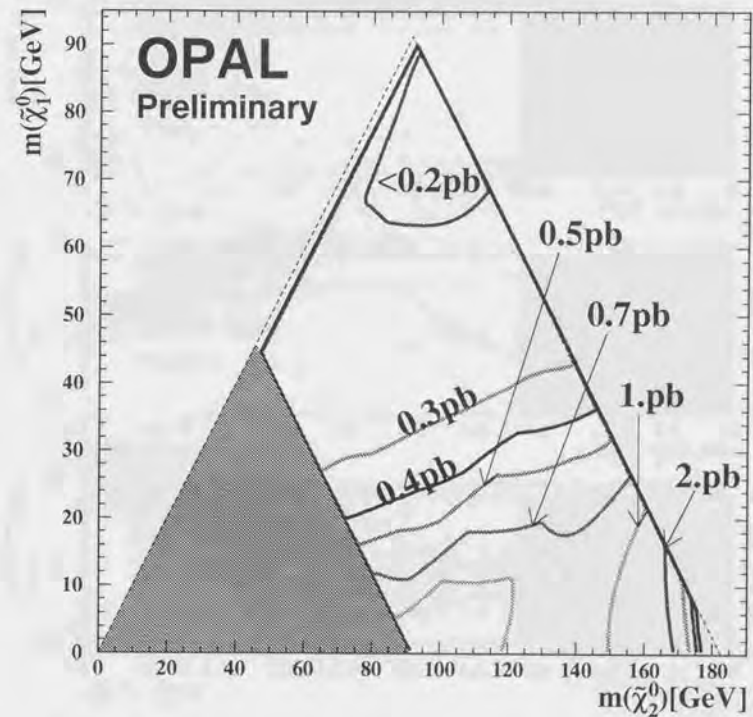


Figure 6.2: Upper limits on the $\tilde{\chi}_2^0 \tilde{\chi}_1^0$ production cross section at 95% C.L., assuming $\tilde{\chi}_2^0 \rightarrow \tilde{\chi}_1^0 Z^{(*)}$, followed by prompt $\tilde{\chi}_1^0 \rightarrow \gamma \tilde{G}$ decays. The shaded region, $m_{\tilde{\chi}_2^0} + m_{\tilde{\chi}_1^0} < m_Z$, is not considered in this analysis because the sensitivity was expected to be higher at $\sqrt{s} \simeq m_{Z^0}$ [44].

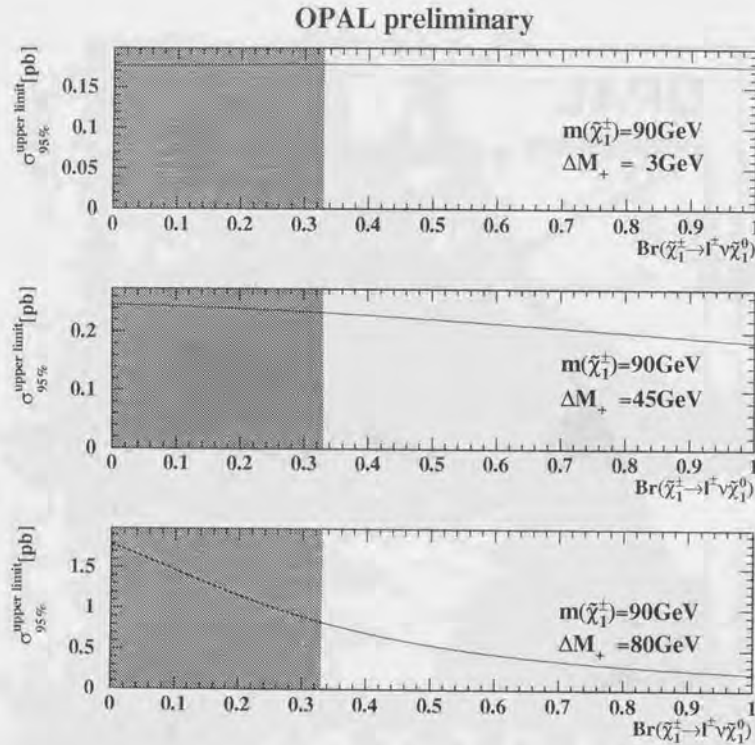


Figure 6.3: Upper limits on the $\tilde{\chi}_1^+ \tilde{\chi}_1^-$ production cross section at 95% C.L. vs. the branching fraction for $\tilde{\chi}_1^+ \rightarrow \tilde{\chi}_1^0 \ell^+ \nu$, assuming prompt $\tilde{\chi}_1^0 \rightarrow \gamma \tilde{G}$ decays, for three example $(m_{\tilde{\chi}_1^+}, \Delta M_+)$ combinations. The shaded region indicates leptonic branching fractions smaller than 100% $W^{(*)\pm}$ decays.

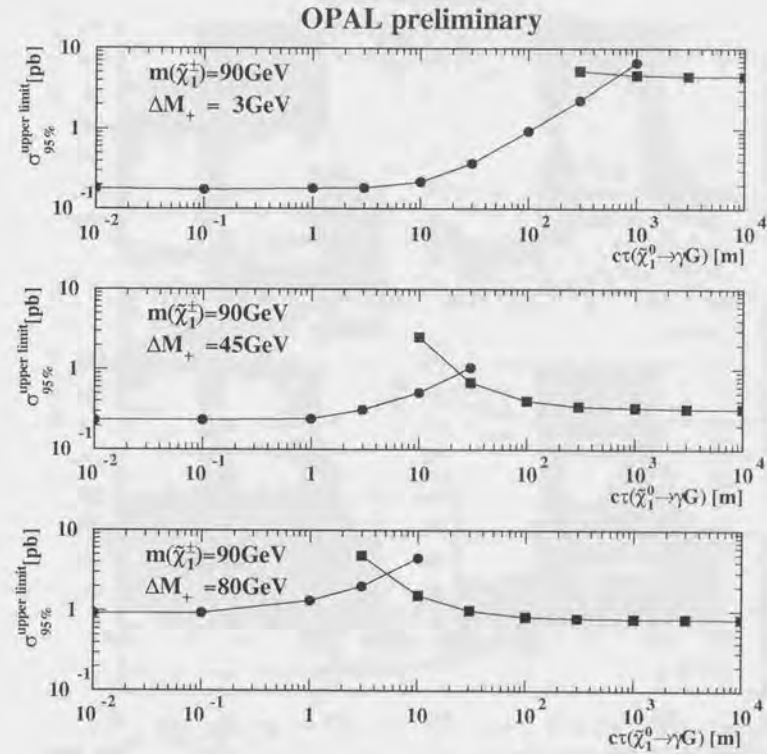


Figure 6.4: Upper limits on the $\tilde{\chi}_1^+ \tilde{\chi}_1^-$ production cross section at 95% C.L., assuming both decay via $\tilde{\chi}_1^+ \rightarrow \tilde{\chi}_1^0 W^{(*)\pm}$, followed by $\tilde{\chi}_1^0 \rightarrow \gamma \tilde{G}$ decays, vs. the $\tilde{\chi}_1^0$ lifetime. The small lifetime limits (connected circles) are from this analysis, while the large lifetime limits (connected squares) come from the gravity-mediated SUSY breaking chargino search.

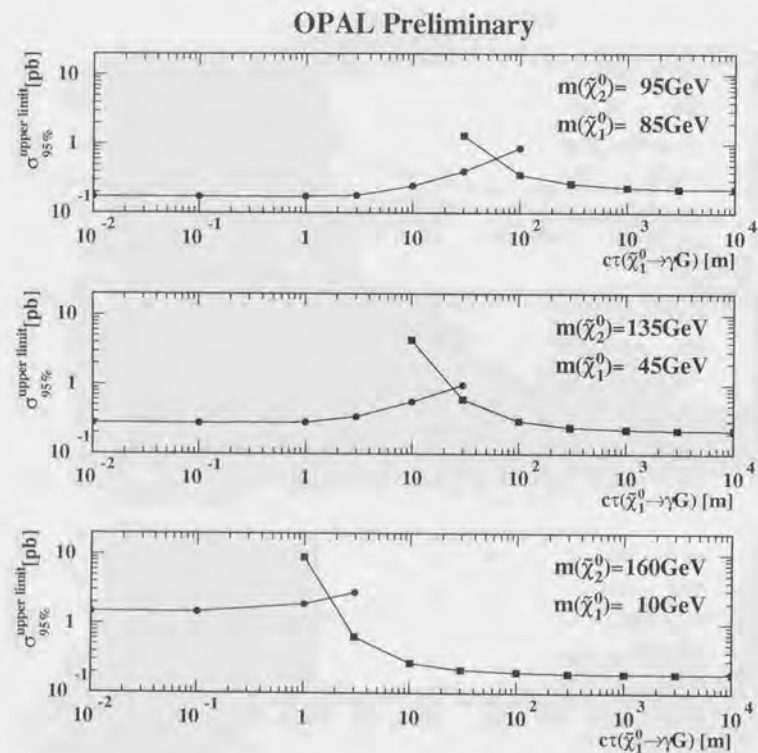


Figure 6.5: Upper limits on the $\tilde{\chi}_2^0 \tilde{\chi}_1^0$ production cross section at 95% C.L., assuming $\tilde{\chi}_2^0$ decay via $\tilde{\chi}_2^0 \rightarrow \tilde{\chi}_1^0 Z^{(*)}$, followed by $\tilde{\chi}_1^0 \rightarrow \gamma G$ decays, vs. the $\tilde{\chi}_1^0$ lifetime. The small lifetime limits (connected circles) are from this analysis, while the large lifetime limits (connected squares) come from the gravity-mediated SUSY breaking neutralino search.

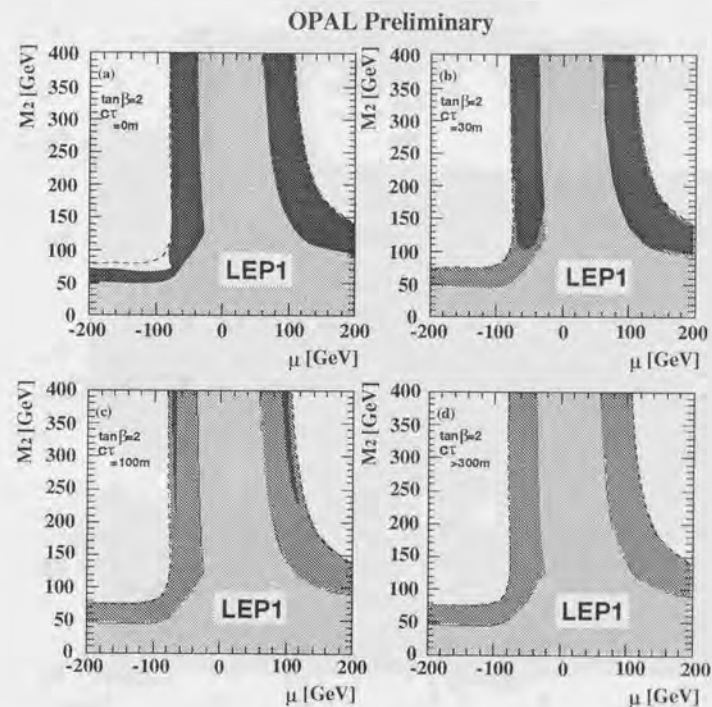


Figure 6.6: Excluded regions in the M_2 vs. μ plane at 95% C.L., for the example case $\tan \beta = 2$, using the $\tilde{\chi}_1^+ \tilde{\chi}_1^-$ results assuming only that each $\tilde{\chi}_1^\pm$ decays into an NLSP $\tilde{\chi}_1^0$. (a) is for $c\tau = 0$, (b) is for $c\tau = 30$ m, (c) is for $c\tau = 100$ m and (d) is for $c\tau = 300$ m. The dark shaded region is excluded by these analyses, while the medium shaded region is additionally excluded by including the gravity mediated $\tilde{\chi}_1^+ \tilde{\chi}_1^-$ search. The light shaded region was kinematically accessible to LEP1, and was not considered in this analysis. The dashed line indicates the kinematic limit.

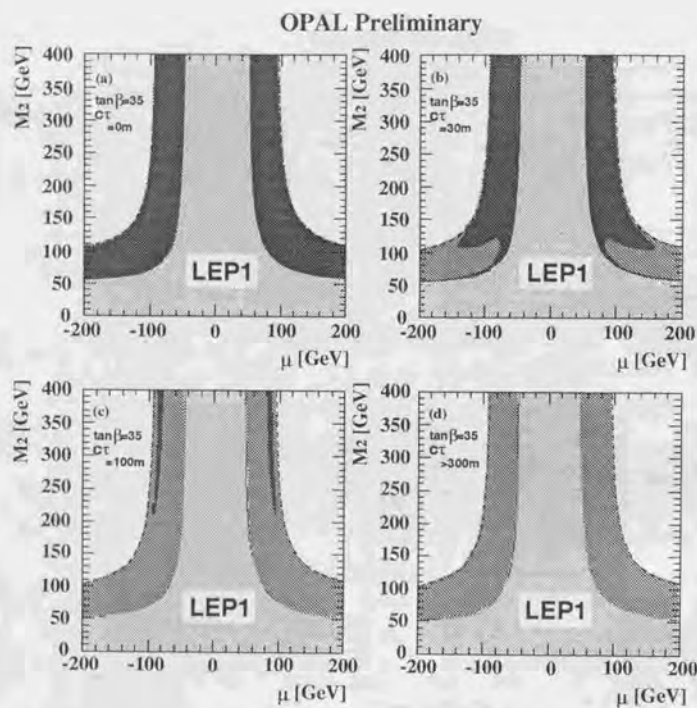


Figure 6.7: Excluded regions in the M_2 vs. μ plane at 95% C.L., for the example case $\tan\beta = 35$, using the $\tilde{\chi}_1^+ \tilde{\chi}_1^-$ results assuming only that each $\tilde{\chi}_1^\pm$ decays into an NLSP $\tilde{\chi}_1^0$. (a) is for $c\tau = 0$, (b) is for $c\tau = 30$ m, (c) is for $c\tau = 100$ m and (d) is for $c\tau = 300$ m. The dark shaded region is excluded by the analyses presented in this note, while the medium shaded region is additionally excluded by including the gravity mediated $\tilde{\chi}_1^+ \tilde{\chi}_1^-$ search. The light shaded region was kinematically accessible to LEP1, and was not considered in this analysis. The dashed line indicates the kinematic limit, and essentially the entire accessible region is excluded for all $\tilde{\chi}_1^0$ lifetimes.

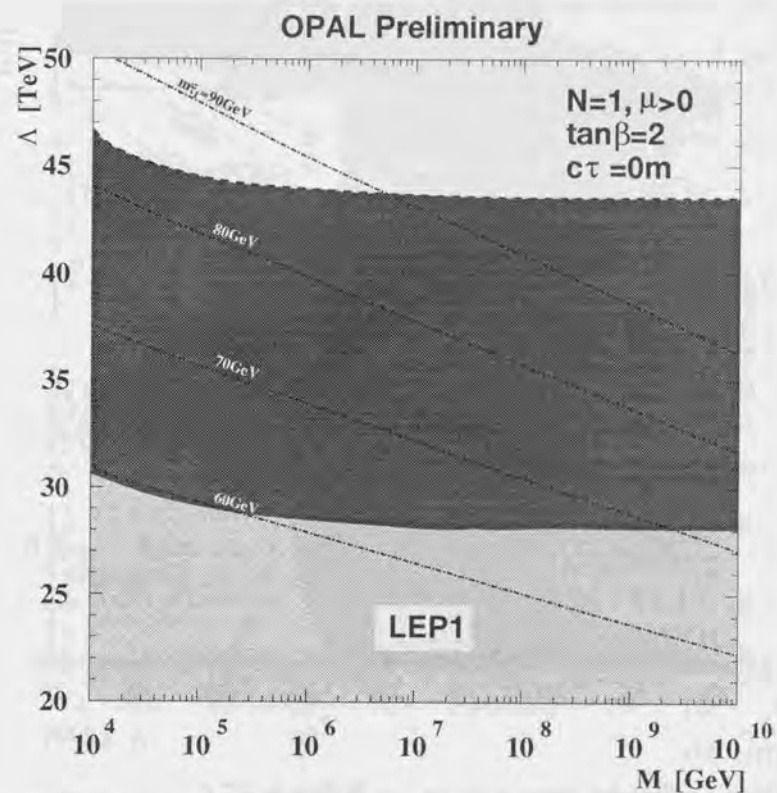


Figure 6.8: Excluded regions in the Λ vs. M plane at 95% C.L., for the case of $N=1$, $\mu > 0$, $\tan\beta = 2$ and $c\tau=0$. The dark shaded region is excluded by this analysis and the light shaded region was kinematically accessible to LEP1. In this parameter space, $\tilde{\chi}_1^0$ is always the NLSP and decays to $\gamma \tilde{G}_2$ while the $\tilde{\tau}_1$ which can be lighter than the $\tilde{\chi}_1^\pm$ decays to $\tilde{\chi}_1^0 \tau$ followed by the $\gamma \tilde{G}$ decay of the $\tilde{\chi}_1^0$. Contours of constant $m_{\tilde{\tau}_1}$ are given by the dash-dotted curves. The dashed line indicates the kinematic limit.

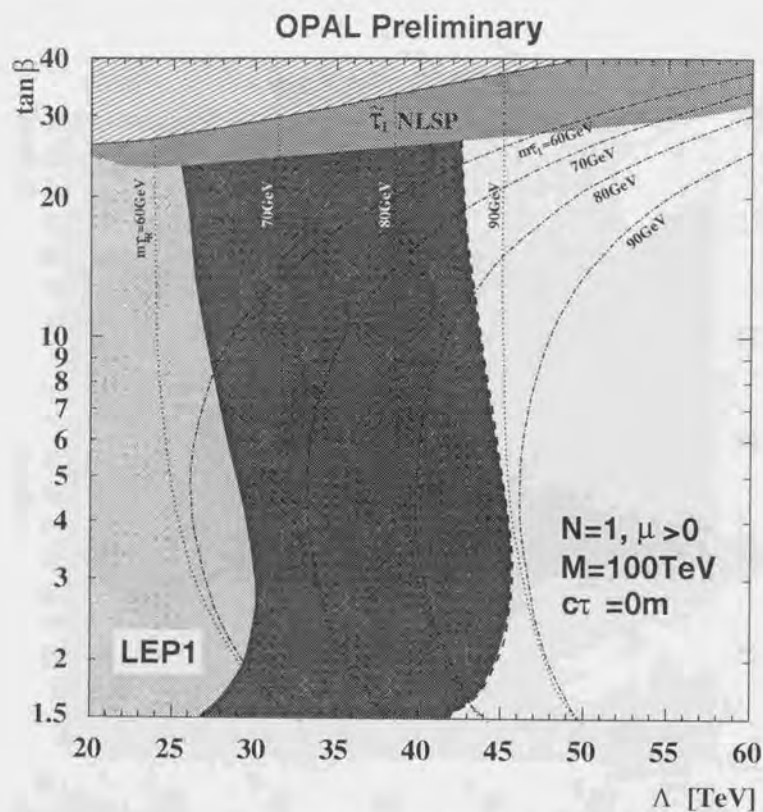


Figure 6.9: Excluded regions in the $\tan \beta$ vs. Λ plane at 95% C.L., for the case of $N=1$, $\mu > 0$, $M=100$ TeV and $c\tau=0$ m. The dark shaded region is excluded by this analysis and the light shaded region was kinematically accessible to LEP1. For large $\tan \beta$, $\tilde{\tau}$ mass eigenstate ($\tilde{\tau}_1$) can be lighter than the $\tilde{\chi}_1^0$ and be the NLSP due to large mixing effect between the left and right handed $\tilde{\tau}$. In addition for more larger $\tan \beta$, the $\tilde{\tau}$ mass-squared becomes negative which is shown as a hatched area in the figure. Contours of constant $m_{\tilde{\tau}_1}$ are given by the dash-dotted curves and contours for right handed sleptons (\tilde{e}_R and $\tilde{\mu}_R$) are shown by the dotted curves. Their mixing between the left and right handed states is small due to the effects proportional to m_ℓ in their mass matrices. The dashed line indicates the kinematic limit.

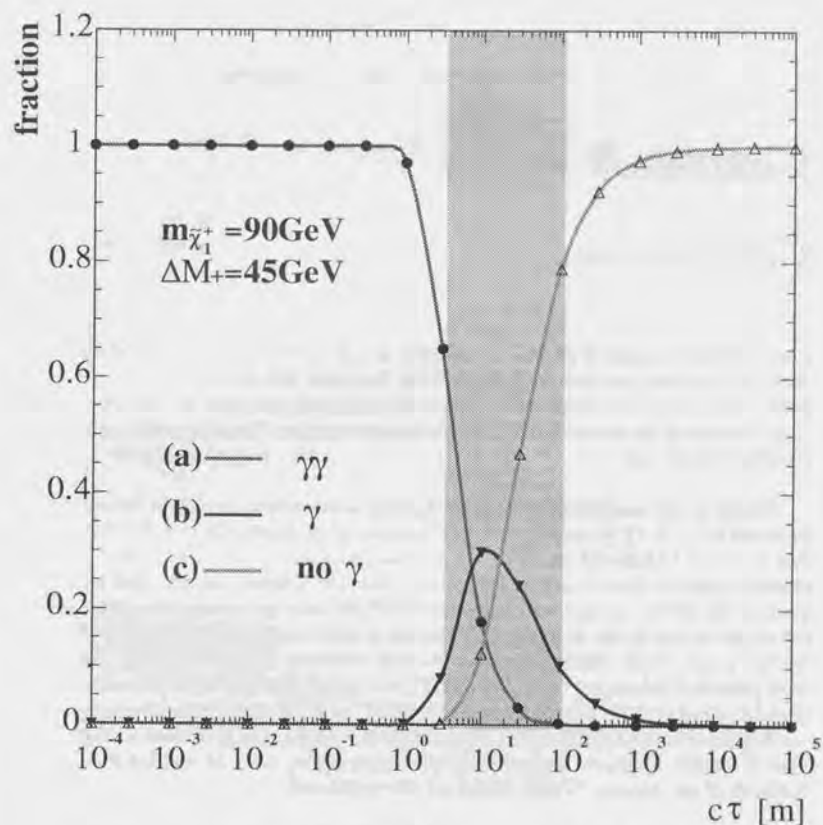


Figure 6.10: The dependence of the fraction of the events with (a):two isolated photons, (b):one isolated photon and (c):no isolated photon on the decay length of $\tilde{\chi}_1^0 \rightarrow \gamma \tilde{G}$ for the chargino pair production with $m_{\tilde{\chi}_1^0} = 90$ GeV and $\Delta M_+ = 45$ GeV. In the shaded region, where the fraction of the events with one isolated photon is greater than 0.1, three types of the events respect to the number of isolated photons would be observed. These are estimated by utilising the signal Monte Carlo for this mass combination and supposing the detection efficiency for the event equal to zero when any $\tilde{\chi}_1^0$ decays inside HCAL. This is the reason why around the shaded region the sum of three fraction is less than one.

Chapter 7

Conclusion

Using the data sample of 56.75pb^{-1} collected at $\sqrt{s} \sim 183\text{ GeV}$ with the OPAL detector, the pair production of the lightest charginos and the associated pair production of the second-lightest and lightest neutralinos have been searched for, in the context of gauge-mediated SUSY breaking scenarios. No evidence for their existence was found.

Limits on the model-independent production cross sections are given for the processes $e^+e^- \rightarrow \tilde{\chi}_1^+\tilde{\chi}_1^-$ and $e^+e^- \rightarrow \tilde{\chi}_2^0\tilde{\chi}_1^0$ supposing the decays of $\tilde{\chi}_1^\pm \rightarrow W^{(\ast)\pm}\tilde{\chi}_1^0$ and $\tilde{\chi}_2^0 \rightarrow Z^{(\ast)}\tilde{\chi}_1^0$ followed by $\tilde{\chi}_1^0 \rightarrow \gamma\tilde{G}$ with zero lifetime. Limits with arbitrary chargino leptonic branching fractions and lifetime are inferred and excluded regions in the M_2 vs. μ plane with different NLSP lifetimes are presented incorporating the results of the chargino search in the gravity-mediated SUSY breaking model by the OPAL collaboration. Limits with arbitrary lifetime of $\tilde{\chi}_1^0$ had not been presented before this work. We would like to stress that this work has established a method to study the gauge-mediated SUSY breaking model experimentally considering non-zero lifetime of NLSP which is one of the striking features in this class of models. Excluded regions in the parameter space, Λ vs. M and $\tan\beta$ vs. Λ planes of the minimal GMSB model are also presented.

In this analysis, it is always supposed that the $\tilde{\chi}_1^0$ is the NLSP. However in more general models where number of messengers can be greater than one (and also in large $\tan\beta$ region), the slepton can be the NLSP. As shown in Section 2.3.2, expected signals for this case are multi-lepton final states with missing energy or greater than minimum ionizing tracks in the tracking detector.

The gauge-mediated SUSY breaking model is very predictive as for the phenomenology at low-energy scale only with a handful of parameters and it has a very attractive feature of the suppression of FCNC's without any fine tuning. If the signal of gauge-mediated SUSY breaking model is established, the SUSY breaking scale can be found by the measurement of lifetime of the NLSP decay.

Still more subjects have to be studied experimentally.

Bibliography

- [1] Y. Gol'fand and E. Likhtam, JETP Lett. 13 (1971) 323;
D. Volkov and V. Akulov, Phys. Lett. B46 (1973) 109;
J. Wess and B. Zumino, Nucl. Phys. B70 (1974) 39.
- [2] H. P. Nilles, Phys. Rep. 110(1984)1;
H. E. Haber and G. L. Kane, Phys. Rep. 117(1985)75.
- [3] Gauge-mediated SUSY breaking has been the subject of intense theoretical activity over the past few years. For example, see several of the excellent review articles ([5] also) and references therein:
S. Ambrosanio, G.D. Kribs, S.P. Martin, "Signals for gauge-mediated supersymmetry breaking models at the CERN LEP2 collider", hep-ph/9703211, Phys. Rev. D56(1997)1761;
G.F. Giudice, R. Rattazzi, "Theories with Gauge-Mediated Supersymmetry Breaking", CERN-TH/97-380, hep-ph/9801271.
- [4] M. Dine, A. E. Nelson, Phys. Rev. D48(1993)1277, hep-ph/9303230;
M. Dine, A. E. Nelson, Y. Shirman, Phys. Rev. D51(1995)1362, hep-ph/9408384;
M. Dine, A. E. Nelson, Y. Nir, Y. Shirman, Phys. Rev. D53(1996)2658, hep-ph/9507378.
- [5] S. Dimopoulos, S. Thomas, J.D. Wells, Nucl. Phys. B488(1997)39, hep-ph/9609434.
- [6] DELPHI Collaboration, P. Abreu *et al.*, Eur. Phys. J. C1(1998)1.
- [7] D0 Collaboration, B. Abbott *et al.*, Phys. Rev. Lett. 80(1998)442.
- [8] S. Deser, B. Zumino, Phys. Rev. Lett. 38(1977)1433;
E. Cremmer *et al.*, Phys. Lett. B 79(1978)231.
- [9] G. G. Ross, *Grand Unified Theories*, (Addison-Wesley, Redwood City CA, 1985).
- [10] P. Fayet, Phys. Lett. B70(1977)461;
P. Fayet, Phys. Lett. B84(1979)416;
P. Fayet, Phys. Lett. B86(1979)272.
- [11] S. Ambrosanio, G. L. Kane, G. D. Kribs, S. P. Martin, S. Mrenna, Phys. Rev. D54, 5395(1996).
- [12] H. E. Haber, G. L. Kane, Phys. Rep. 117(1985)75;
J. F. Gunion, H. E. Haber, Nucl. Phys. B272(1986)1.
- [13] S. Dimiopoulos, M. Dine, S. Raby, S. Thomas, Phys. Rev. Lett. 76(1996)3494.
- [14] K.-I. Izawa, Y. Nomura, K. Tobe, T. Yanagida, Phys. Rev. D56(1997)2886.
- [15] V. Barger, M. S. Berger, P. Ohmann, Phys. Rev. D49(1994)4908
- [16] V. Barger, M. S. Berger, P. Ohmann, Phys. Rev. D47(1993)1093;
V. Barger, M. S. Berger, P. Ohmann, Phys. Rev. D47(1993)2038;
V. Barger, M. S. Berger, P. Ohmann, R. Phillips, Phys. Lett. B314(1993)351;
S. Bertolini, F. Borzumati, A. Masiero, G. Ridolfi, Nucl. Phys. B353(1993)591.
- [17] K. Inoue, A. Kakuto, H. Komatsu, H. Takeshita, Prog. Theor. Phys. 68(1982)927;
K. Inoue, A. Kakuto, H. Komatsu, H. Takeshita, Prog. Theor. Phys. 71(1984)413.
- [18] OPAL Collab., K. Ackerstaff *et al.*, hep-ex/9801024, Subm. to Z. Phys. C.
- [19] OPAL Collab., K. Ackerstaff *et al.*, Euro. Phys. Journal C1 (1998) 45-64.
- [20] OPAL Collab., K. Acherstaff *et al.*, hep-ex/9710010, Subm. to Z. Phys. C.
- [21] OPAL Collab., K. Ahmet *et al.*, Nucl. Instr. Meth. A305(1991)275;
P.P. Allport *et al.*, Nucl. Instr. Meth. A346(1994)476;
B.E. Anderson *et al.*, IEEE Trans. on Nucl. Science 41(1994)845.
- [22] M. Arignon *et al.*, Nucl. Instr. Meth. A313(1992)103.
- [23] A.A. Carter *et al.*, Nucl. Instr. Meth. A250(1986)503.
- [24] SF57 lead glass, Schott Glaswerke, Hattenbergstrasse 10, D-6500 Mainz 1, Germany.
- [25] CEREN-25 lead glass, Corning France, 44 Avenue de Valvins, Avon, Cedex 77210, France.

- [26] J. Allison *et al.*, Nucl. Instr. Meth. **A317**(1992)47.
- [27] GEANT-Detector Description and Simulation Tools, CERN Program Library.
- [28] C. Dionisi *et al.*, in 'Physics at LEP2', eds. G. Altarelli, T. Sjöstrand and F. Zwirner, CERN 96-01, vol.2 (1996)337.
- [29] E. Accomando *et al.*, 'Event Generators for Discovery Physics', hep-ph/9602203, Feb. 1996, and in 'Physics at LEP2', eds. G. Altarelli, T. Sjöstrand and F. Zwirner, CERN 96-01, vol.2 (1996)299.
- [30] E. Boudinov *et al.*, ' $\gamma\gamma$ Event Generators', hep-ph/9512371, Dec. 1995, and in 'Physics at LEP2', eds. G. Altarelli, T. Sjöstrand and F. Zwirner, CERN 96-01, vol.2 (1996)187.
- [31] G. Marchesini *et al.*, Comp. Phys. Comm. **67**(1992)465.
- [32] J. Fujimoto *et al.*, KEK-CP-046 (1996).
- [33] J.A.M. Vermaseren, Nucl. Phys. **B229**(1983)347.
- [34] S. Jadach, B. F. L. Ward, Z. Wąs, Comp. Phys. Comm. **79**(1994)503.
- [35] S. Jadach, W. Placzek, B.F.L. Ward, in 'Physics at LEP2', eds. G. Altarelli, T. Sjöstrand and F. Zwirner, CERN 96-01, vol.2 (1996).
- [36] T. Sjöstrand, Comp. Phys. Comm. **39**(1986)347;
T. Sjöstrand, PYTHIA 5.7 and JETSET 7.4 Manual, CERN-TH 7112/93.
- [37] N. Brown and W.J. Stirling, Phys. Lett. **B252**(1990)657;
S. Bethke, Z. Kunszt, D. Soper and W.J. Stirling, Nucl. Phys. **B370**(1992)310;
S. Catani, Phys. Lett. **B269**(1991)432;
N. Brown and W.J. Stirling, Z. Phys. **C53**(1992)629.
- [38] JADE Collab., S. Bethke *et al.*, Phys. Lett. **B213**(1988)235.
- [39] S. Jadach, E. Richter-Wąs, B.F.L. Ward and Z. Wąs, Comp. Phys. Comm. **70** (1992)305.
- [40] Valerie Gibson, A Measurement of the Conversion Finding Efficiency in OPAL, OPAL Technical Note TN367, unpublished.
- [41] OPAL Collaboration, K. Ackerstaff *et al.*, CERN-PPE/97-083 (14 July 1997), accepted for publication in Eur. J. Phys. C for a more complete description.

- [42] "Review of Particle Physics" R.M. Barnett *et al.*, Phys. Rev. **D54**(1996).
- [43] R.D. Cousins and V.L. Highland, Nucl. Instr. Meth. **A320**(1992)331.
- [44] OPAL Collaboration, G. Alexander *et al.*, Phys. Lett. **B377**(1996)273.
- [45] J. Ellis, J.L. Lopez and D.V. Nanopoulos, Phys. Lett. **B394**(1997)354.
- [46] A. Brignole, F. Feruglio and F. Zwirner, hep-ph/9711516.
- [47] K. Maki, S. Orito, Phys. Rev. **D57**(1998)1.

Appendix A

SUSY particles

Higgs bosons and superpartners in the MSSM and the GMSB models are listed in Table A.1.

Particles	Spin	R -parity	Mass eigenstates	Gauge eigenstates
Higgs bosons	0	+1	h, H^0, A, H^\pm	$\tilde{H}_u, \tilde{H}_d, \tilde{H}_u^\pm, \tilde{H}_d^\pm$
squarks	0	-1	$\tilde{u}_L, \tilde{u}_R, \tilde{d}_L, \tilde{d}_R$ $\tilde{c}_L, \tilde{c}_R, \tilde{s}_L, \tilde{s}_R$ $\tilde{t}_1, \tilde{t}_2, \tilde{b}_1, \tilde{b}_2$	$\tilde{u}_L, \tilde{u}_R, \tilde{d}_L, \tilde{d}_R$ $\tilde{c}_L, \tilde{c}_R, \tilde{s}_L, \tilde{s}_R$ $\tilde{t}_L, \tilde{t}_R, \tilde{b}_L, \tilde{b}_R$
sleptons	0	-1	$\tilde{e}_L, \tilde{e}_R, \tilde{\nu}_e$ $\tilde{\mu}_L, \tilde{\mu}_R, \tilde{\nu}_\mu$ $\tilde{\tau}_1, \tilde{\tau}_2, \tilde{\nu}_\tau$	$\tilde{e}_L, \tilde{e}_R, \tilde{\nu}_e$ $\tilde{\mu}_L, \tilde{\mu}_R, \tilde{\nu}_\mu$ $\tilde{\tau}_L, \tilde{\tau}_R, \tilde{\nu}_\tau$
neutralinos	1/2	-1	$\tilde{\chi}_1^0, \tilde{\chi}_2^0, \tilde{\chi}_3^0, \tilde{\chi}_4^0$	$\tilde{B}, \tilde{W}^0, \tilde{H}_u^0, \tilde{H}_d^0$
charginos	1/2	-1	$\tilde{\chi}_1^\pm, \tilde{\chi}_2^\pm$	$\tilde{W}^\pm, \tilde{H}_u^\pm, \tilde{H}_d^\pm$
gluino	1/2	-1	\tilde{g}	\tilde{g}
gravitino	3/2	-1	\tilde{G}	\tilde{G}

Table A.1: Higgs bosons and superpartners.

Appendix B

Field contents of gauginos

The higgsinos and electroweak gauginos mix with each other due to the effects of electroweak symmetry breaking. The neutral higgsinos (\tilde{H}_u, \tilde{H}_d) and the neutral gauginos (\tilde{B}, \tilde{W}^0) mix to form four neutral mass eigenstates called neutralinos. The charged higgsinos ($\tilde{H}_u^\pm, \tilde{H}_d^\pm$) and winos ($\tilde{W}^\pm, \tilde{W}^\pm$) mix to form two mass eigenstates with charge ± 1 called charginos.

B.1 Neutralinos

The neutralino mass eigenstates are denoted by $\tilde{\chi}_i^0$ ($i=1,2,3,4$) where $m_{\tilde{\chi}_1^0} < m_{\tilde{\chi}_2^0} < m_{\tilde{\chi}_3^0} < m_{\tilde{\chi}_4^0}$. In the gauge eigenstate basis $\psi^0 = (\tilde{B}, \tilde{W}^0, \tilde{H}_u^0, \tilde{H}_d^0)$, the neutralino mass terms in the Lagrangian are

$$-\frac{1}{2}(\psi^0)^T \mathbf{M}_{\tilde{\chi}^0} \psi^0 + c.c. \quad (\text{B.1})$$

where

$$\mathbf{M}_{\tilde{\chi}^0} = \begin{pmatrix} M_1 & 0 & -\cos\beta \sin\theta_W m_Z & \sin\beta \sin\theta_W m_Z \\ 0 & M_2 & \cos\beta \cos\theta_W m_Z & -\sin\beta \cos\theta_W m_Z \\ -\cos\beta \sin\theta_W m_Z & \cos\beta \cos\theta_W m_Z & 0 & -\mu \\ \sin\beta \sin\theta_W m_Z & -\sin\beta \cos\theta_W m_Z & -\mu & 0 \end{pmatrix} \quad (\text{B.2})$$

The field contents of the mass eigenstates are given by $\tilde{\chi}_i^0 = \mathbf{N} \psi^0$ with a unitary matrix \mathbf{N} which diagonalizes $\mathbf{M}_{\tilde{\chi}^0}$. The mixing matrix \mathbf{N} is parametrised by M_1, M_2, μ and $\tan\beta$ but the results are rather complicated to be written in a simple form. However in the limit $m_Z \ll |\mu|$, which is favoured in the GMSB models, the masses of $\tilde{\chi}^0$'s can be written with a good approximation.

For $\tilde{\chi}_1^0$ and $\tilde{\chi}_2^0$, they are given by

$$m_{\tilde{\chi}_i^0} \simeq M_i - \frac{m_Z^2 \sin^2\theta_W (M_i + \mu \sin 2\beta)}{\mu^2 - M_i^2} \quad (\text{B.3})$$

$$m_{\tilde{\chi}_2^0} \simeq M_2 - \frac{m_W^2(M_2 + \mu \sin 2\beta)}{\mu^2 - M_2^2}. \quad (\text{B.4})$$

B.2 Charginos

The chargino mass eigenstates are denoted by $\tilde{\chi}_i^\pm$ ($i=1,2$) where $m_{\tilde{\chi}_1^\pm} < m_{\tilde{\chi}_2^\pm}$. In the gauge eigenstate basis $\psi^\pm = (\tilde{W}^+, \tilde{H}_u^+, \tilde{W}^-, \tilde{H}_d^-)$, the chargino mass terms in the Lagrangian are

$$-\frac{1}{2}(\psi^\pm)^T \mathbf{M}_{\tilde{\chi}^\pm} \psi^\pm + c.c. \quad (\text{B.5})$$

where, in 2×2 block form,

$$\mathbf{M}_{\tilde{\chi}^\pm} = \begin{pmatrix} 0 & X^T \\ X & 0 \end{pmatrix}; \quad \mathbf{X} = \begin{pmatrix} M_2 & \sqrt{2} \sin \beta m_W \\ \sqrt{2} \cos \beta m_W & \mu \end{pmatrix}. \quad (\text{B.6})$$

The mass eigenstates are written as follows,

$$\begin{pmatrix} \tilde{\chi}_1^+ \\ \tilde{\chi}_2^+ \end{pmatrix} = \mathbf{V} \begin{pmatrix} \tilde{W}^+ \\ \tilde{H}_u^+ \end{pmatrix}; \quad \begin{pmatrix} \tilde{\chi}_1^- \\ \tilde{\chi}_2^- \end{pmatrix} = \mathbf{U} \begin{pmatrix} \tilde{W}^- \\ \tilde{H}_d^- \end{pmatrix} \quad (\text{B.7})$$

with two unitary 2×2 matrices \mathbf{U} and \mathbf{V} which diagonalize \mathbf{X} as

$$\mathbf{U}^T \mathbf{X} \mathbf{V}^{-1} = \begin{pmatrix} m_{\tilde{\chi}_1^\pm} & 0 \\ 0 & m_{\tilde{\chi}_2^\pm} \end{pmatrix}. \quad (\text{B.8})$$

Because there are only 2×2 matrices, the masses of charginos are written explicitly as

$$m_{\tilde{\chi}_1^\pm}^2 = \frac{1}{2} \left[(M_2^2 + \mu^2 + 2m_W^2) - \sqrt{(M_2^2 + \mu^2 + 2m_W^2)^2 - 4(\mu M_2 - m_W^2 \sin 2\beta)^2} \right] \quad (\text{B.9})$$

$$m_{\tilde{\chi}_2^\pm}^2 = \frac{1}{2} \left[(M_2^2 + \mu^2 + 2m_W^2) + \sqrt{(M_2^2 + \mu^2 + 2m_W^2)^2 - 4(\mu M_2 - m_W^2 \sin 2\beta)^2} \right] \quad (\text{B.10})$$

In the limit $m_Z \ll |\mu|$, $\tilde{\chi}_1^\pm$ is wino like and $\tilde{\chi}_2^\pm$ is higgsino like with masses

$$m_{\tilde{\chi}_1^\pm} \simeq M_2 - \frac{m_W^2(M_2 + \mu \sin 2\beta)}{\mu^2 - M_2^2} \quad (\text{B.11})$$

$$m_{\tilde{\chi}_2^\pm} \simeq |\mu| + \frac{m_W^2(|\mu| + M_2 \sin 2\beta)}{\mu^2 - M_2^2} \quad (\text{B.12})$$

Appendix C

Particle ID

C.1 Electron ID

In the algorithm to calculate the energy flow electron identification tool based on the neural net technique is employed. There are 12 input variables to the neural net listed below.

- **P** the momentum of the track
- **CT** $\cos \theta$ of the track
- **DEDX** dE/dX in CJ
- **DDED** the error on dE/dX
- **ECLOP** the energy of the ECAL cluster associated to the track divided by the momentum P.
- **NBLO** the total number of blocks in the ECAL cluster.
- **EOVP** E_{cone} over P where E_{cone} is the energy in the ECAL blocks whose center is contained within a 30 mrad half cone around the track.
- **NBECO** number of possible blocks for E_{cone} . Ranges from 0 to 4 (0 when there is no cluster associated to the track).
- **EOVE2** E_{cone} over E_{cone2} where $E_{cone2} = E_{cone} +$ all adjacent blocks.
- **EDPH** absolute ϕ difference between track and ECAL cluster.
- **EDTH** θ difference between track and ECAL cluster.
- **PBPE** presampler multiplicity.

The neural net is trained on the Monte Carlo samples in order to discriminate electrons from hadrons with the momentum greater than 2 GeV. Efficiency in electrons and probability of mistagging a hadron as an electron are 77.4% and 0.151% respectively.

C.2 Muon ID

As for muon identification there exist three types of muon identification criteria and if any of the criteria is satisfied, the track and the associated cluster is identified as a muon. Those criteria are listed below.

- Using ECAL/TOF information,
 - The track should match with the clusters in the muon detector,
 - should fulfil the kaon rejection requirement by dE/dx measurement,
 - should have matching TOF or ECAL cluster and
 - measured energy by ECAL cluster should be smaller than 3.0 GeV.
- Using HCAL information,
 - The track should match with the clusters in the muon detector,
 - should fulfil the kaon rejection requirement by dE/dx measurement and
 - should be identified as a muon track with HCAL by requiring conditions on the number of hit layers and the last hit layer.
- For the track which goes through the holes in the muon detector,
 - The track should be identified as a muon track with hadron calorimeter selection same as B2,
 - should fulfil the kaon rejection requirement by $dEdx$ measurement and
 - should have matching TOF or ECAL cluster.

Appendix D

The OPAL Collaboration

K. Ackerstaff⁸, G. Alexander²³, J. Allison¹⁶, N. Altekamp⁵, K.J. Anderson⁹, S. Anderson¹², S. Arcelli², S. Asai²⁴, S.F. Ashby¹, D. Axen²⁹, G. Azuelos^{18,a}, A.H. Ball¹⁷, E. Barberio⁸, R.J. Barlow¹⁶, R. Bartoldus³, J.R. Batley⁵, S. Baumann³, J. Bechtluft¹⁴, T. Behnke⁸, K.W. Bell²⁰, G. Bella²³, S. Bentvelsen⁸, S. Bethke¹⁴, S. Betts¹⁵, O. Biebel¹⁴, A. Biguzzi⁵, S.D. Bird¹⁶, V. Blobel²⁷, I.J. Bloodworth¹, M. Bobinski¹⁰, P. Bock¹¹, D. Bonacorsi², M. Boutemeur³⁴, S. Braibant⁸, L. Brigliadori², R.M. Brown²⁰, H.J. Burckhart⁸, C. Burgard⁸, R. Bürgin¹⁰, P. Capiluppi², R.K. Carnegie⁶, A.A. Carter¹³, J.R. Carter⁵, C.Y. Chang¹⁷, D.G. Charlton^{1,b}, D. Chrisman⁴, P.E.L. Clarke¹⁵, I. Cohen²³, J.E. Conboy¹⁵, O.C. Cooke⁸, C. Couyoumtzelis¹³, R.L. Coxe⁹, M. Cuffiani², S. Dado²², C. Dallapiccola¹⁷, G.M. Dallavalle², R. Davis³⁰, S. De Jong¹², L.A. del Pozo¹, A. de Roeck⁸, K. Desch⁸, B. Dienes^{33,d}, M.S. Dixit⁷, M. Doucet¹⁸, E. Duchovni²⁶, G. Duckeck³⁴, I.P. Duerdoth¹⁶, D. Eatough¹⁶, P.G. Estabrooks⁶, E. Etzion²³, H.G. Evans⁹, M. Evans¹³, F. Fabbri², A. Fanfani², M. Fanti², A.A. Faust³⁰, L. Feld⁸, F. Fiedler²⁷, M. Fierro², H.M. Fischer³, I. Fleck⁸, R. Folman²⁶, D.G. Fong¹⁷, M. Foucher¹⁷, A. Fürtjes⁸, D.I. Futyan¹⁶, P. Gagnon⁷, J.W. Gary¹, J. Gascon¹⁸, S.M. Gascon-Shotkin¹⁷, N.I. Geddes²⁰, C. Geich-Gimbel³, T. Gerasis²⁰, G. Giacomelli², P. Giacomelli⁴, R. Giacomelli², V. Gibson⁵, W.R. Gibson¹³, D.M. Gingrich^{30,a}, D. Glenzinski⁹, J. Goldberg²², M.J. Goodrick⁶, W. Gorn¹, C. Grandi², E. Gross²⁶, J. Grunhaus²³, M. Grunewald²⁷, C. Hajdu³², G.G. Hanson¹², M. Hansroul⁸, M. Hapke¹³, C.K. Hargrove⁷, P.A. Hart⁹, C. Hartmann³, M. Hauschild⁸, C.M. Hawkes³, R. Hawkins²⁷, R.J. Hemingway⁶, M. Herndon¹⁷, G. Herten¹⁰, R.D. Heuer⁸, M.D. Hildreth⁸, J.C. Hill⁹, S.J. Hillier¹, P.R. Hobbins²⁵, A. Hocker⁹, R.J. Homer¹, A.K. Honma^{28,a}, D. Horváth^{32,c}, K.R. Hossain³⁰, R. Howard²⁹, P. Hüntemeyer²⁷, D.E. Hutchcroft⁵, P. Igo-Kemenes¹¹, D.C. Imrie²⁵, K. Ishii²⁴, A. Jawahery¹⁷, P.W. Jeffreys²⁰, H. Jeremie¹⁸, M. Jimack¹, A. Joly¹⁸, C.R. Jones⁵, M. Jones⁶, U. Jost¹¹, P. Jovanovic¹, T.R. Junk⁸, J. Kanizaki²⁴, D. Karlen⁶, V. Kartvelishvili¹⁶, K. Kawagoe²⁴, T. Kawamoto²⁴, P.I. Kayal³⁰, R.K. Keeler²⁸, R.G. Kellogg¹⁷, B.W. Kennedy²⁰, J. Kirk²⁹, A. Klier²⁶, S. Kluth⁸, T. Kobayashi²⁴, M. Kobel¹⁰, D.S. Koetke⁶, T.P. Kokott³, M. Kolrep¹⁰, S. Komamiya²³, R.V. Kowalewski²⁸, T. Kress¹¹, P. Krieger⁶, J. von Krogh¹¹, P. Kyberd¹³,

G.D. Lafferty¹⁶, R. Lahmann¹⁷, W.P. Lai¹⁰, D. Lanske¹⁴, J. Lauber¹⁵,
 S.R. Lautenschlager³¹, I. Lawson²⁸, J.G. Layter⁴, D. Lazic²², A.M. Lee³¹, E. Lefebvre¹⁸,
 D. Lellouch²⁶, J. Lettis¹², L. Levinson²⁶, B. List⁸, S.L. Lloyd¹³, F.K. Loebinger¹⁶,
 G.D. Long²⁸, M.J. Losty⁷, J. Ludwig¹⁰, D. Lui¹², A. Macchiolo², A. Macpherson³⁰,
 M. Mannelli⁸, S. Marcellini², C. Markopoulos¹³, C. Markus⁴, A.J. Martin¹³,
 J.P. Martin¹⁸, G. Martinez¹⁷, T. Mashimo²⁴, P. Mättig²⁶, W.J. McDonald³⁰,
 J. McKeena²⁹, E.A. Mckigney¹⁵, T.J. McMahon¹, R.A. McPherson²⁸, F. Meijers⁸,
 S. Menke³, F.S. Merritt⁹, H. Mes⁷, J. Meyer²⁷, A. Michelini², S. Mihara²⁴,
 G. Mikenberg²⁶, D.J. Miller¹⁵, A. Mincer^{22,e}, R. Mir²⁶, W. Mohr¹⁰, A. Montanari²,
 T. Mori²⁴, K. Nagai²⁶, I. Nakamura²⁴, H.A. Neal¹², B. Nellen³, R. Nisius⁸,
 S.W. O'Neale¹, F.G. Oakham⁷, F. Odorici², H.O. Ogren¹², A. Oh²⁷, N.J. Oldershaw¹⁶,
 M.J. Oreglia⁹, S. Orito²⁴, J. Pálincás^{33,d}, G. Pásztor³², J.R. Pater¹⁶, G.N. Patrick²⁰,
 J. Patt¹⁰, R. Perez-Ochoa⁸, S. Petzold²⁷, P. Pfeifschneider¹⁴, J.E. Pilcher⁹,
 J. Pinfold³⁰, D.E. Plane⁸, P. Poffenberger²⁸, B. Poli², A. Posthaus³, C. Rembs⁸,
 S. Robertson²⁸, S.A. Robins²², N. Rodning³⁰, J.M. Roney²⁸, A. Rooke¹⁵, A.M. Rossi²,
 P. Rountenburg³⁰, Y. Rozen²², K. Runge¹⁰, O. Runolfsson⁸, U. Ruppel¹⁴, D.R. Rust¹²,
 K. Sachs¹⁰, T. Saeki²⁴, O. Sahr³⁴, W.M. Sang²⁵, E.K.G. Sarkisyan²³, C. Sbarra²⁹,
 A.D. Schaile³⁴, O. Schaile³⁴, F. Scharf⁵, P. Scharff-Hansen⁸, J. Schieck¹¹, P. Schleper¹¹,
 B. Schmitt⁸, S. Schmitt¹¹, A. Schöning⁸, M. Schröder⁸, M. Schumacher³, C. Schwick⁸,
 W.G. Scott²⁰, T.G. Shears⁸, B.C. Shen⁴, C.H. Shepherd-Themistocleous⁸,
 P. Sherwood¹⁵, G.P. Siroli², A. Sittler²⁷, A. Skillman¹⁵, A. Skuja¹⁷, A.M. Smith⁸,
 G.A. Snow¹⁷, R. Sobie²⁸, S. Söldner-Rembold¹⁰, R.W. Springer³⁰, M. Sproston³⁰,
 K. Stephens¹⁶, J. Steuerer²⁷, B. Stockhausen³, K. Stoll¹⁰, D. Strom¹⁹, R. Ströhmer³⁴,
 P. Szymanski²⁰, R. Tafirout¹⁸, S.D. Talbot¹, P. Taras¹⁸, S. Tarem²², R. Teuscher⁸,
 M. Thiergen¹⁰, M.A. Thomson⁸, E. von Törne³, E. Torrence⁸, S. Towers⁶, I. Trigger¹⁸,
 Z. Trócsányi³³, E. Tsir²³, A.S. Turcot⁹, M.F. Turner-Watson⁸, I. Ueda²⁴, P. Utzat¹¹,
 R. Van Kooten¹², P. Vannerem¹⁰, M. Verzocchi¹⁰, P. Vikas¹⁸, E.H. Vokurka¹⁶, H. Voss³,
 F. Wäckerle¹⁰, A. Wagner²⁷, C.P. Ward⁶, D.R. Ward⁶, P.M. Watkins¹, A.T. Watson¹,
 N.K. Watson¹, P.S. Wells⁸, N. Wermes³, J.S. White²⁸, G.W. Wilson²⁷, J.A. Wilson¹,
 T.R. Wyatt¹⁶, S. Yamashita²⁴, G. Yekutieli²⁶, V. Zacc¹⁸, D. Zer-Zion⁸

¹School of Physics and Astronomy, University of Birmingham, Birmingham B15 2TT, UK

²Dipartimento di Fisica dell'Università di Bologna and INFN, I-40126 Bologna, Italy

³Physikalisches Institut, Universität Bonn, D-53115 Bonn, Germany

⁴Department of Physics, University of California, Riverside CA 92521, USA

⁵Cavendish Laboratory, Cambridge CB3 0HE, UK

⁶Ottawa-Carleton Institute for Physics, Department of Physics, Carleton University, Ottawa, Ontario K1S 5B6, Canada

⁷Centre for Research in Particle Physics, Carleton University, Ottawa, Ontario K1S 5B6, Canada

⁸CERN, European Organisation for Particle Physics, CH-1211 Geneva 23, Switzerland

⁹Enrico Fermi Institute and Department of Physics, University of Chicago, Chicago IL 60637, USA

¹⁰Fakultät für Physik, Albert Ludwigs Universität, D-79104 Freiburg, Germany

¹¹Physikalisches Institut, Universität Heidelberg, D-69120 Heidelberg, Germany

¹²Indiana University, Department of Physics, Swain Hall West 117, Bloomington IN 47405, USA

¹³Queen Mary and Westfield College, University of London, London E1 4NS, UK

¹⁴Technische Hochschule Aachen, III Physikalisches Institut, Sommerfeldstrasse 26-28, D-52056 Aachen, Germany

¹⁵University College London, London WC1E 6BT, UK

¹⁶Department of Physics, Schuster Laboratory, The University, Manchester M13 9PL, UK

¹⁷Department of Physics, University of Maryland, College Park, MD 20742, USA

¹⁸Laboratoire de Physique Nucléaire, Université de Montréal, Montréal, Québec H3C 3J7, Canada

¹⁹University of Oregon, Department of Physics, Eugene OR 97403, USA

²⁰Rutherford Appleton Laboratory, Chilton, Didcot, Oxfordshire OX11 0QX, UK

²¹Department of Physics, Technion-Israel Institute of Technology, Haifa 32000, Israel

²²Department of Physics and Astronomy, Tel Aviv University, Tel Aviv 69978, Israel

²³International Centre for Elementary Particle Physics and Department of Physics, University of Tokyo, Tokyo 113, and Kobe University, Kobe 657, Japan

²⁴Institute of Physical and Environmental Sciences, Brunel University, Uxbridge, Middlesex UB8 3PH, UK

²⁵Particle Physics Department, Weizmann Institute of Science, Rehovot 76100, Israel

²⁶Universität Hamburg/DESY, II Institut für Experimentale Physik, Notkestrasse 85, D-22607 Hamburg, Germany

²⁷University of Victoria, Department of Physics, P O Box 3055, Victoria BC V8W 3P6, Canada

²⁸University of British Columbia, Department of Physics, Vancouver BC V6T 1Z1, Canada

²⁹University of Alberta, Department of Physics, Edmonton AB T6G 2J1, Canada

³⁰Duke University, Dept of Physics, Durham, NC 27708-0305, USA

³¹Research Institute for Particle and Nuclear Physics, H-1525 Budapest, P O Box 49, Hungary

³²Institute of Nuclear Research, H-4001 Debrecen, P O Box 51, Hungary

³³Ludwigs-Maximilians-Universität München, Sektion Physik, Am Coulombwall 1, D-85748 Garching, Germany

⁹ and at TRIUMF, Vancouver, Canada V6T 2A3

⁶ and Royal Society University Research Fellow

^c and Institute of Nuclear Research, Debrecen, Hungary

^d and Department of Experimental Physics, Lajos Kossuth University, Debrecen, Hungary

^e and Department of Physics, New York University, NY 1003, USA



THE UNIVERSITY OF CHICAGO PRESS
1995
ISBN 0-226-08312-5
HARVARD-YENCHING INSTITUTE OF CHINESE STUDIES
HONG KONG

